Investigation into the effects of optogenetic stimulation on the structure and function of stem cell derived cardiomyocytes

Craig Hamilton

BSc(Hons), MRes

Submitted in fulfilment of the requirements for the degree of Doctor of Philosophy to the Institute of Cardiovascular and Medical Sciences, University of Glasgow

Research conducted at the Institute of Cardiovascular and Medical Science, College of Medical, Veterinary and Life Sciences, University of Glasgow, U.K.

July 2018

Abstract

INTRODUCTION: The first beats of the developing heart resemble peristaltic contractions with electrical activity arising in the precursor to the sino-atrial node and propagating through the heart tube. The purpose of this thesis was to investigate channelrhodopsin-2 (ChR-2) based optogenetic stimulation of induced pluripotent stem cell derived cardiomyocytes (iPSC-CMs) with the intention of using the technique to investigate the functional effects of directional activation on immature cardiomyocytes.

METHODS: Commercially supplied iPSC-CMs (Axiogenesis) were made to express ChR-2 (H134R) via an adeno-associated viral vector (AAV1.CAG.hChR2(H134R)-mCherry.WPRE.SV40). Cell function was assessed before and after pacing using in house software to measure contraction kinetics and strength-duration curves to determine cell excitability. α-actinin staining allowed for analysis of sarcomere length, inhomogeneity and alignment.

RESULTS: Commercially supplied iPSC-CMs had significantly shorter sarcomeres than their adult counterparts (1.766 ± 0.017 μm vs 2.028 ± 0.079 μm respectively, P=0.0125 unpaired t-test). A viral load of 2500GC/cell produced ChR-2 expression sufficient for optical control of these cells 5 days post transfection. The chronaxie of photostimulated cells (1.53 ± 0.32 ms) did not differ significantly from that of electrically stimulated cells (2.17 ± 0.44 ms, P=0.2434 unpaired t-test). Prolonged photostimulation of a single site led to a loss of stimulation:contraction coupling after 2.22 ± 1.26 hours and almost complete loss of contractile function after 24 hours. Alternating stimulation between multiple sites allowed cells to be paced for 96 hours and allowed directional electrical activation to be imposed on immature heart cells. 96 hours of directional pacing produced no changes in cell structure or cell excitability but produced a significant reduction in contraction upstroke time (72.03 ms vs 48.85 ms P=0.023 one-way ANOVA) 24 hours after the termination of stimulation.

CONCLUSIONS: This project has demonstrated that replicating the directional electrical activity of the developing heart can induce a modest change in contractile function that may represent a step towards functional maturation of commercially available iPSC-CMs.

Table of Contents

List of Tables

List of Figures

Acknowledgements

I would first like to thank my supervisors and mentors, Godfrey and Niall. Their contribution has been invaluable, and their patience (and sarcasm) has been limitless.

I'd like to thank technicians Aileen (Queen of the lab) and Mike, without whom nothing would get done. They deserve all the praise possible.

I'd also like to thank my lab buddy Ana. She helped me keep my sanity, I am greatly indebted to her.

I feel I should also thank my parents for instilling in me a great sense of curiosity and encouraging me to go into science.

Finally, I'd like to dedicate this work to my wife Melissa. She has been an unending font of support and motivation. She is the reason I do everything I do.

Author's Declaration

"I declare that, except where explicit reference is made to the contribution of others, that this dissertation is the result of my own work and has not been submitted for any other degree at the University of Glasgow or any other institution."

Printed Name: CRAIG HAMILTON

Signature: _____

Definitions/Abbreviations

Abbreviation	Explanation
(h)ESC	(human) embryonic stem cell
(h)ESC-CM	(human) embryonic stem cell derived cardiomyocyte
(h)iPSC	(human) induced pluripotent stem cell
(h)iPSC-CM	(human) induced pluripotent stem cell derived cardiomyocyte
APD	Action potential duration
AVV	Atrioventricular valve
BCECF	2',7'-bis-(2-carboxyethyl)-5-(and-6)-carboxyfluorescein
BMP	Bone morphogenetic protein
CD10	Contraction duration at 10% contraction
CD50	Contraction duration at 50% contraction
CD90	Contraction duration at 90% contraction
ChR-2	Channelrhodopsin-2
C_m	Membrane capacitance
Cx43	Connexin 43
Dn90	Relaxation duration
EHT	Engineered heart tissues

Abbreviation	Explanation
EMCCD	Electron multiplying charge-coupled device
FFT	Fast Fourier transform
FWHM	Full width at half maximum
GC	Genome copies
Hand2	heart and neural crest derivatives expressed 2
I_f	Funny/pacemaker current
IGF-1	Insulin-like growth factor
I_{k1}	Inward rectifier potassium current
I_{Na}	Voltage gated sodium current
IP_3	**Inositol 1,4,5-trisphosphate**
I_{to}	Transient outward current
LED	Light emitting diode
MEA	Microelectrode array
MI	Myocardial infarction
MOI	Multiplicity of infection
NCX	Sodium calcium exchanger
ND	Neutral density filter

Abbreviation	Explanation
NRVM	Neonatal rat ventricular myocyte
PBS	Phosphate buffered saline
PFA	Paraformaldehyde
PMT	Photomultiplier tube
R_m	Membrane resistance
ROS	Reactive oxygen species
RyR2	Cardiac ryanodine receptor
SAN	Sino-atrial node
SERCA	Sarco/endoplasmic reticulum calcium ATPase
SOCE	Store operated Ca^{2+} Entry
SR	sarcoplasmic reticulum
T3	Triiodothyronine
Up90	Upstroke duration
V_m	Membrane potential
V_o	Unloaded shortening velocity
Wnt	Wingless-related integration site protein
α-MHC	α-myosin heavy chain

Abbreviation	Explanation
β-MHC	β-myosin heavy chain
ΔV	Change in transmembrane potential

Chapter 1: Introduction

1.1 Introduction

During a myocardial infarction regions of ischaemia of variable size are formed which can result in the loss of many millions of cardiomyocytes[1] making up a significant percentage of the total myocardium. Loss of these cells causes increased strain on the remaining myocardium as it attempts to maintain cardiac output. The increased strain causes pathological remodelling which can lead to decreased cardiac output and heart failure. To progress to heart failure, an infarct in the left ventricle must kill approximately 25% of the 4 billion cells contained within[1], indicating that both the site and the size of the infarct are important in determining patient outcome. In 2010 heart failure was attributed to 279,000 deaths in the US[2] with 33% of heart failure patients having had a previous MI[3], indicating that current strategies for preventing MI progression to HF are ineffective. More recently many groups have begun developing methods of generating cardiomyocytes from pluripotent cells to replace those lost during MI. These cells can then be combined with a collagen matrix or grown in a monolayer to produce cardiac tissue grafts suitable for transplantation into the damaged heart to improve cardiac function.

The ability to produce cardiomyocytes from pluripotent stem cells is of great interest to another aspect of cardiac medicine: Toxicity screening. Approximately 33% of all drugs are withdrawn during human clinical trials due to cardiotoxic effects not seen during animal studies[4]. The primary reason that cardiotoxic effects are not observed in animal models is electrophysiological variation between species. Cardiomyocytes derived from human pluripotent stem cells therefore allows drugs to be screened on human cardiac tissue and is thought to yield clinically relevant toxicity data, with the caveat that current products yield cardiac cells at an embryonic stage of development

1.2 Embryonic development

At Day 15 of human uterine development, progenitor cells from the primitive streak migrate superiorly to form a bilateral plate known as the heart field (Figure 1.1). At this point the progenitor cells are divided into distinct populations of endodermal cells and mesodermal cells. The mesodermal cells are further separated into the haematopoietic and cardiac lineage. Unbalanced

increases in any of these populations can lead to heart defects[5,6]. Segregation of these cell lineages is determined by wingless-related integration site protein (Wnt) and bone morphogenetic protein (BMP) signalling which is modulated by a gradient of Activin/Nodal signalling present throughout the developing heart.

The heart field is split spatiotemporally into the first and second heart fields. At 20 days of development, cells from the first heart field migrate medially where they differentiate in response to endodermal BMP signalling to form the primitive heart tube[7] (Figure 1.1). At this stage, cells of the secondary heart field are held in a progenitor state via canonical Wnt signalling. At day 21 cells from the secondary heart field migrate to the heart tube which acts as a scaffold allowing the secondary cells to differentiate and lead to the generation of structures such as the left and right atria as well as the outflow tracts comprising the conotruncus. The sinus venosus is also formed at this stage from a pool of progenitors originating in the inferolateral border of the secondary heart field[8]. This process is complete at day 22 when the heart tube first begins the beat in a peristaltic manner[9] (Figure 1.1). While the first few beats of the heart may be due to spontaneous activity of the cardiomyocytes[10] it has been shown that, at this stage, the heart is likely under the control of a primordial sinoatrial node (SAN) present in the sinus venosus[11]. At this stage action potential conduction is homogenous throughout the heart tube resulting in a sinusoidal ECG[12].

Around day 28 rightward looping of the heart tube occurs (Figure 1.1). At this stage cells migrate to the outflow tract from the cardiac neural crest to form the aortic arch and the aortic arch arteries. Septation of the ventricles and atria then begins due to the influence of GATA-4, TBX-5 and NKX2.5[13-15]. Formation of the Atrioventricular valve (AVV) also begins at this stage due to BMP2 and TBX2 interactions[16,17]. Around the same time, the true SAN first develops[18] from the cells of the sinus venosus. The formation of the AVV, which has a slower conduction velocity than atrial and ventricular cells, means that the previously peristaltic contraction of the heart is separated into serial contractions of the atria and ventricles. This is reflected in a more matured ECG phenotype[12]. At this stage, well developed sodium, calcium and potassium currents have been detected and L-type calcium current appears to be the dominant excitatory current[19].

Septation continues until the four distinct chambers of the heart are formed around day 50 (Figure 1.1). Throughout this time the phenotypes of atrial and ventricular cells diverge due to modulation of heart and neural crest derivatives expressed 2 (Hand2) and Delta-like protein 1 signalling by microRNAs mir1-1 and mir1-2 in the ventricles and atria respectively[20]. At this stage, sodium current has increased in density to become the dominant excitatory current with rapidly activating potassium currents, such as I_{to}, being the dominant repolarising currents. It is important to note that there are no chamber specific differences in expression of excitatory currents, however there are significant chamber differences in repolarising currents[19].

1.2.1 EC coupling during cardiac development

In the mature heart calcium entry via the L-Type Ca^{2+} channels causes Ca^{2+} release from the sarcoplasmic reticulum via the ryanodine receptor(RyR2)[21]. In the foetal cardiomyocyte the SR is known to exist, due to the presence of caffeine-induced SR Ca^{2+} release[22], however it is reported to be underdeveloped based on results from electron microscopy[23] and isolation of SR vesicles[24,25]. These results are consistent with evidence that ryanodine has little effect on cellular contraction[23].

These results imply that the Ca^{2+} transient in the foetal heart is comprised mainly of Ca^{2+} entering the cell via sarcolemmal Ca^{2+} channels. This is reinforced by evidence that foetal calcium transients are blocked by the L-type Ca^{2+} channel blocker nifedipine[22]. The density of the L-type Ca^{2+} current has been shown to increase throughout foetal development[19,26] and continues to increase after birth. This is in contrast to the outward Na^{+}/Ca^{2+} exchange (NCX) current density which increases throughout foetal development peaking around birth before decreasing during postnatal dvelopment[27-29]. This postnatal decrease accompanies an increase in maturation of the SR[24,25] indicating that NCX may compensate for the immature SR during foetal development but plays a lesser role in the mature heart. There is evidence to suggest that this change in dominance may be due to hormonal signalling from the thyroid[30].

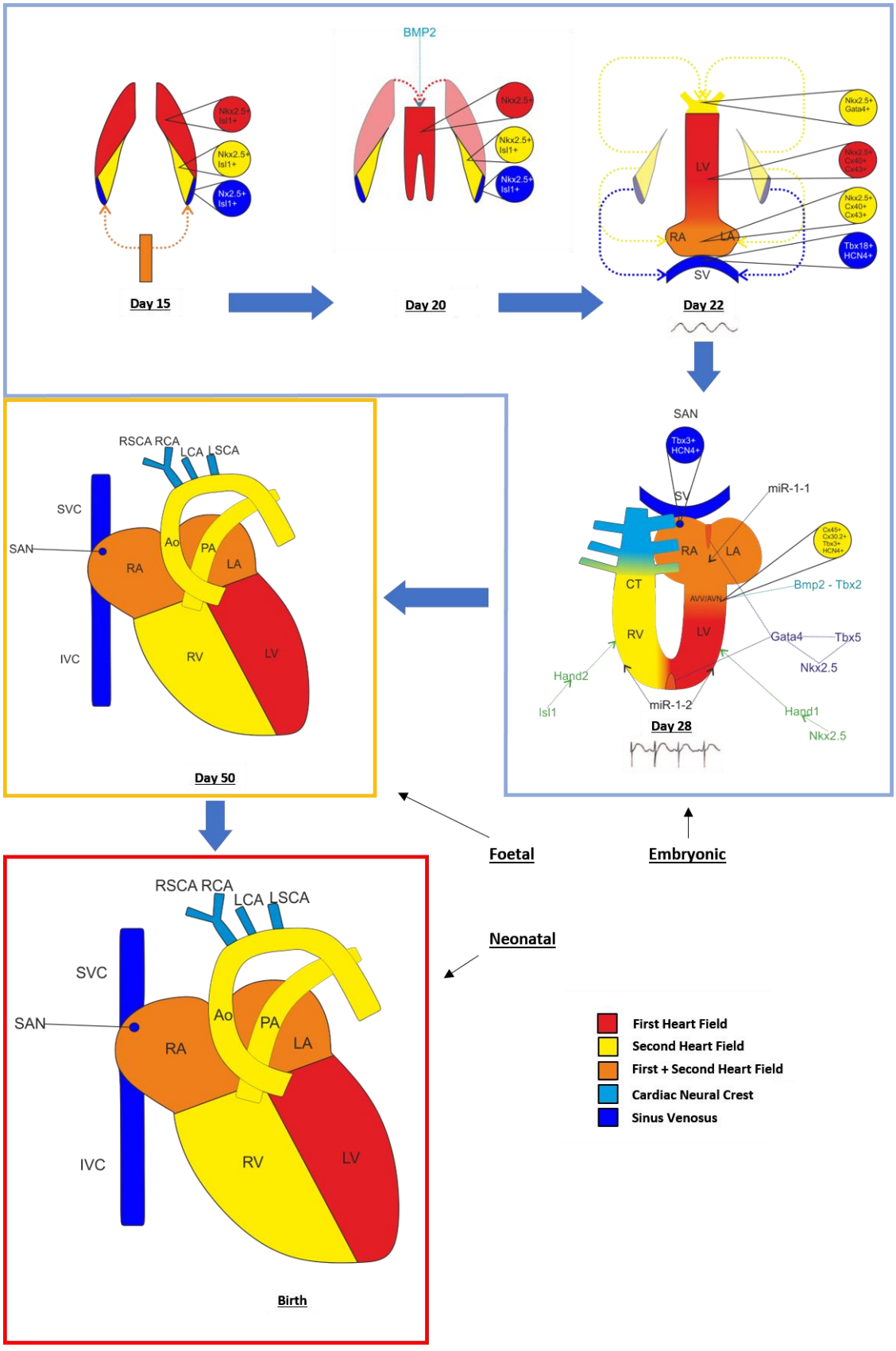

Figure 1.1 Embryonic cardiac development
Diagrammatic representation of human foetal cardiac development. LV: left ventricle. RA: Right Atria. LA: Left Atria. SV: Sinus venosus. CT: Conotruncus. RV: Right Ventricle. SAN: Sinoatrial Node. AVV/AVN: Atrioventricular valve/node. Ao: Aorta. PA: Pulmonary artery. RSCA: Right subclavian artery. RCA: right carotid artery. LCA: Left carotid artery. LSCA: Left subclavian artery. SVC: Superior Vena cava. IVC: Inferior vena cava.

Ca^{2+} sparks, discrete Ca^{2+} release events caused by activation of a single cluster of RyR2 channels, are virtually absent in the foetal heart[22]. Sparks can be categorised as spontaneous (independent of L-type Ca^{2+}) or evoked (triggered by calcium entry via L-type Ca^{2+} channel[31]). It has been shown that sparks begin to develop in the neonatal heart arising initially in close proximity to the surface membrane and appearing throughout the whole cell over time[22]. This is likely due to the increase in colocalisation of RyR2 and L-type Ca^{2+} channels that accompanies development of the t-tubules[22]. Given that spontaneous Ca^{2+} sparks arise largely as a result of high SR Ca^{2+}, and neonatal cardiomyocytes have a significantly reduced SR capacity[32], it is unsurprising that evoked sparks are prevalent in neonatal cardiomyocytes.

1.3 Post-natal development

It is important to note that throughout foetal development, the Carnegie stages allow for a simple interspecies comparison of developmental landmarks, i.e. studies on rat or mouse development can be easily translated into human development[33]. The absence of such a system for post-natal development makes interspecies comparisons much more difficult.

In the days following birth, growth of the heart changes from hyperplasic growth to hypertrophic growth. Increases in cell volume and binucleation shows that this change in dominance occurs around day 4 in the rat with approximately 90% of cardiomyocytes becoming binucleated by day 12[34]. By day 18 in rat the T-tubular system is almost completely developed[22] and by day 20, L-type Ca^{2+} current is not significantly different from adult cells. However at this point the Ca^{2+} content of the sarcoplasmic reticulum is still significantly lower than that of an adult cell[32]. In new born humans (< 2 weeks of age) cells display a characteristic flat or slightly negative force-frequency relationship. In infants (3-14 months), this has changed to a positive force frequency relationship akin to the adult heart[29]. In the adult heart, additional calcium release from intracellular stores is thought to arise due to activation of the inositol 1,4,5-triphosphate (IP_3) receptor by IP_3 generated by G protein-coupled receptors in the surface membrane[35]. This IP_3 signalling pathway has been detected in neonatal rat cardiomyocytes as young as 1 day old[36,37].

It is difficult to determine at which time point cardiomyocytes become adult. There is no adequate marker of maturity in these cells, several different characteristics of the cells are similar to adult at different time points and there is no clear consensus as to what characteristics must be present before a cell may be classed as adult. For example, although T-tubules are almost fully developed at day 18 their presence is not suitable as a marker of maturity as they develop as a response to increased cell size (Figure 1.2).

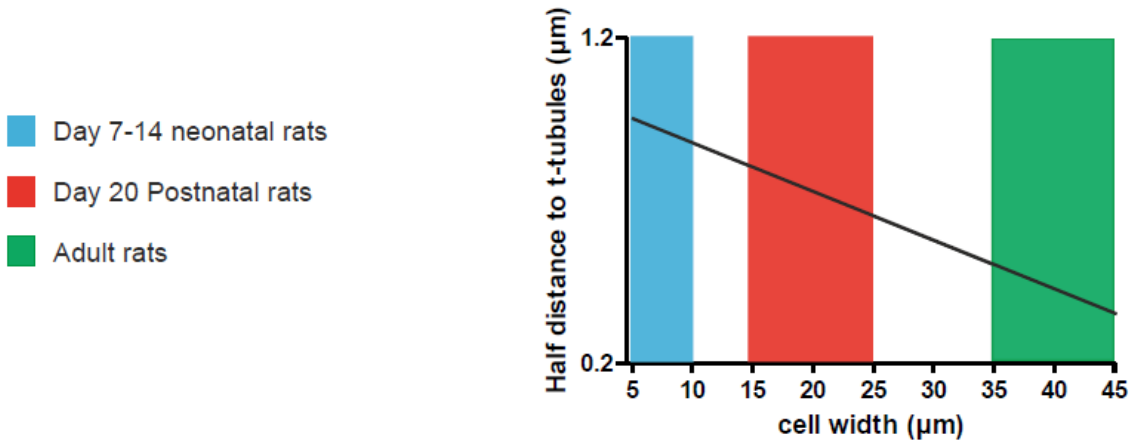

Figure 1.2 Relation of t-tubule density to cell size
T-tubule density increases with increasing cell size. Coloured bands show the cell width of neonatal (blue), post-natal (red) and adult (green) rat ventricular cardiomyocytes. Figure adapted from Richards et al[38]

1.4 Pluripotent stem cell derived cardiomyocytes

Traditionally the main source of pluripotent cells were embryonic stem cells. Use of these cells has large ethical concerns due to the destruction of human embryos. More recently retroviral transfection of fibroblasts with transcription factors (Oct3/4, Sox2, Klf4, and c-Myc) [39,40] generated pluripotent cells which were similar to embryonic stem cells in terms of surface morphology, gene expression, and surface proteins.

Both embryonic (ESC) and induced (iPSC) pluripotent stem cells have been used to generate cardiomyocytes using various means.

1.5 Current strategies for cardiomyocyte development

A number of groups have attempted to produce cardiac differentiation of stem cells by replicating conditions found during uterine development. In addition to work on pluripotent cells, a great deal of work has been carried out on neonatal rat ventricular myocytes (NRVM) as they have a similar level of maturity as derived cardiomyocytes.

1.5.1 Biochemical

A logical step in deriving cardiomyocytes from stem cells is to mimic the signalling pathways that arise during physiological development. Treatment of

embryonic stem cells with BMP4 and Activin A can cause cardiogenesis in both ESCs and iPSCs which can be enhanced by the addition of inhibitors of Activin/nodal signalling[41]. Inhibition of canonical Wnt signalling (responsible for maintaining a progenitor state during development) has been shown be a potent inducer of cardiomyocytes[42]. These methods produce cardiomyocytes at a prenatal or neonatal maturity level. In order to produce more adult like cells, the next logical step is to mimic peri- and post-natal factors.

One such factor is the thyroid hormone triiodothyronine (T3) which has been shown to cause cardiomyocyte maturation. Foetal sheep cardiomyocytes demonstrated increased cell width, binucleation and increased expression of SERCA in response to increased levels of T3 during in vivo development[43]. T3 has also been shown to increase expression of Nkx2.5, SERCA and RyR2 in murine ESC-CM's. In addition to an increased amplitude of caffeine induced Ca^{2+} transients (representing a more mature SR) these cells also had a more negative resting membrane potential again indicating increased maturity[44]. Improved Ca^{2+} handling and increased SERCA expression with a concomitant increase in contractile force were also shown in human iPSC-CMs following 1 week exposure to T3[45].

A common factor throughout the foetal, post-natal and adult heart is the presence of micro RNA's specifically miR-1[46]. This microRNA was shown to decrease the resting potential and APD of ESC-CMs via an increase in repolarising potassium currents and a decrease in the pacemaker current. Given the regional differences in expression of miR-1 isoforms during development[20], It is possible that stem cell derived cardiomyocytes with chamber specific phenotypes may be produced.

1.5.2 Electrical stimulation

From day 22 onwards the foetal heart is electrically active. It has been shown that electrical stimulation can cause cardiogenesis in ESCs through the generation of intracellular ROS[47]. Further to this it has been shown that pacing of NRVM at physiological rates produced increases in fractional shortening, cell alignment and cell coupling[48] as well as increased: NCX expression; action potential duration; and conduction velocity[49].

Pacing of human ESC-CMs has demonstrated similar increases in action potential duration as well as increased SERCA expression and increased caffeine induced Ca^{2+} release[50]. A recent study has shown that chronic pacing (10 days) of human iPSC engineered heart tissue increases fractional shortening and contractile force as well as producing a more mature structural phenotype in terms of cell shape and size[51].

1.5.3 Mechanical

During physiological development, the 3D structure of the heart and the rhythmic contractions mean that developing cardiomyocytes experience significant mechanical loading. Significant amounts of work have gone into investigating the effects these conditions on cardiomyocyte maturation.

One method that has been successful in maturing both NRVM and ESC-CMs is cyclic stretching. Sustained cyclic stretching has been shown to cause characteristic morphological and electrophysiological changes associated with maturation in NRVM[52,53]. 10% strain at 2 Hz for 2 weeks increased expression of cardiac specific markers such as α-MHC, GATA-4 and Nkx2.5 in ePSCs[54]. Cycle stretching of ESC-CMs has also been shown to cause significant increases in cell size, sarcomere organisation[55] as well as increased electrical coupling, increased Ca^{2+} re-uptake, and increased expression of the inward rectifying potassium channel and voltage gated sodium channel[56].

Other attempts at replicating developmental conditions have been carried out through the use of cell patterning and 3D culture. This has led to a great amount of research into hydrogels of different compositions that have differing electrical and mechanical properties, many of which have been shown to increase cardiomyocyte differentiation. Micropatterning of cells onto various substrates can be used to control cell orientation and cause increases in myofilament alignment, electrical coupling[57], and force of contraction[58]. 3D culture methods utilising hydrogel embedded with rigid support columns have been shown to cause cardiac progenitor cells from mouse ESCs and human iPSCs to differentiate into cardiomyocytes in a highly functional engineered heart tissue[59,60].

1.5.4 Combined strategies

Recently, focus has shifted to the development of maturation methods that encompass several aspects of physiological maturation.

One research group developed a novel bioreactor using both mechanical and electrical stimulation within the same system to mimic isovolumic contraction. NRVMs were cultured in a fibrin construct wrapped around inflatable latex tubing such that, when air was injected and removed from the tubing, the construct was stretched circumferentially. Cyclic stretching to 5% strain at 1Hz followed by a delayed electrical stimulus (mimicking isovolumic contraction during adult cardiac cycle) produced a distinct increase in SERCA expression that was not produced by isolated mechanical or electrical stimulation[61].

Another study investigated the effects of electrical stimulation (ES) in the presence of IGF-1 on the maturation of NRVM within a polyglycerol scaffold. They showed visually that there was greater expression of connexin 43 (Cx43) under dual stimulation when compared to ES or IGF-1 alone. They also showed a marked increase in contractility of the engineered tissue following dual stimulation compared to little or no increase with individual stimuli[62].

1.6 Cardiomyocyte maturity

Currently available stem cell derived cardiomyocytes have a broad range of maturation levels ranging from the equivalent of day 22 embryonic cardiomyocytes to neonatal cardiomyocytes. Compared to their adult counterparts derived cardiomyocytes differ in a number of ways.

1.6.1 Structure

Stem cell derived cardiomyocytes tend to be circular in appearance[63,64] and have a much smaller surface area than fully mature cells[65,66]. In addition to the small size there is a significantly lower, but variable level of organisational alignment of sarcomeric proteins α-actinin and β-MHC[50,63,67]. Concomitant with the smaller surface area is infrequent or absent transverse tubules (T-Tubules) [68,69]. Absence of a mature T-tubule network may contribute to the immature nature of calcium handling within these cells.

1.6.2 Contractile function and ECC

In the mature cell, calcium induced calcium release from the sarcoplasmic reticulum is the major source of intracellular calcium during EC coupling[21]. Stem cell derived cardiomyocytes have lower expression of many calcium handling proteins such as RyR2 and phospholamban[70] and have mixed responsiveness to calcium releasing drugs such as caffeine and thapsigargin[71-74]. As a result, the calcium transients of these cells are smaller as well as being poorly coupled to electrical activation due to the absence of T-tubules[68]. This, combined with the poor sarcomeric organisation means that the contractile force of derived cardiomyocytes is significantly lower (nN/mm^2)[75] than adult cells ($\mu N/mm^2$)[76]. An important alternative Ca^{2+} handling pathway in adult cardiomyocytes, IP_3 mediated Ca^{2+} release and store operated calcium entry (SOCE), have both been shown to be present in derived cardiomyocytes[77-79].

1.6.3 Electrophysiological properties

A major distinguishing feature of derived cardiomyocytes is the spontaneous activity they demonstrate[45,50,64]. The presence of the pacemaker current (I_f) and lack of inward rectifier current (I_{k1})[80] causes the resting membrane potential to increase gradually towards the threshold for voltage gated sodium channels (I_{Na}) resulting in spontaneous activation. It has been suggested that stem cell derived cardiomyocytes exhibit differential atrial or nodal phenotypes at different stages of development with appropriate levels of both I_f and I_{k1}[80]. The reduced spontaneous activity of the cells exhibiting the atrial phenotype correlates well with studies showing reduced numbers of spontaneously active cells when cells are plated at lower densities[81] indicating that spontaneous activity in monolayers may be due to the presence of nodal cells.

The reduced I_{k1} expression in derived cardiomyocytes leads to a more positive membrane potential than mature cells[64,82]. This more positive membrane potential, coupled with decreased expression of sodium channels[83], can cause a decreased upstroke velocity[82,84]. Expression of connexin 43 has been shown to be dispersed throughout the membrane of derived cardiomyocytes contrasting the highly polarised distribution found in adult myocytes. This combined with the

decreased upstroke velocity results in a conduction velocity that is significantly lower than adult heart tissue[85,86].

1.7 Applications

1.7.1 Transplantation

An obvious use of stem cell derived cardiomyocytes is to replace the cells lost during MI to prevent progression to heart failure. Indeed, studies have shown minor improvements in cardiac function following successful transplantation of cardiomyocytes in animal models of heart failure[87-89]. These cells are an ideal candidate for transplantation as they can be patient specific, thereby removing any complications due to rejection. Despite this, the clinical use of stem cell derived cardiomyocytes for this purpose is currently infeasible for several reasons.

Firstly, the poor electrical coupling, calcium handling and spontaneous activity of the derived cells means that the transplanted cells are pro-arrhythmic in nature[89] although this is contested by research showing suppression of post-MI arrhythmias[90].

Secondly, the low survival rates[88] means that a large number of cells are needed to replace those lost during MI[91]. In addition to this rejection free grafting is only possible via iPSC-CMs derived from somatic cells of the individual patients. The high cost and low efficacy of the techniques[42] used in the generation of these cells means that currently, generation of sufficient patient specific cells would be prohibitively time consuming and expensive.

1.7.2 Cardiotoxicity assays and drug discovery

Around 33% of all drugs are withdrawn during clinical trials due to unforeseen cardiotoxic effects[4]. This is due to electrophysiological differences between the animal models used and the clinical target (humans). A more clinically relevant substrate for pharmacological testing would allow for increased drug safety as well as increases in drug discovery. Stem cell derived cardiomyocytes have been shown to have similar current densities to isolated human cells[92-96] indicating that they may have a greater clinical relevance than animal models.

The validity of these cells as a drug screening candidate is supported by studies showing arrhythmia generation in response to drugs that are known to be pro-arrhythmic[97]. Another advantage of the cell-based drug assay is the use of the 96 well format, allowing for high throughput screening of multiple drugs.

Once a reliably mature cell line is available independent assays may be used to investigate the effects of drugs in both healthy and diseased hearts. One caveat to the use of cell-based assay systems is that many drugs have cardiotoxic effects due to long term exposure or have toxic products produced by drug metabolism. Given the limited lifetime of these cells in culture and the lack of a complex drug metabolism, these toxic effects would not be observable in a cell-based system.

An alternative to a purely cell-based system is the “Organ on a chip” design. Advances in microfluidics has allowed for the creation of new *in vitro* models that more accurately replicate the complex, multicellular 3D structure of several organs including lung[98], liver[99], kidneys[100], and heart[101]. The eventual goal of these artificial organs is to create a “Human on a chip” where the separate organs are connected. This system would allow drug metabolism to be mimicked more accurately and be could be used to replace animal models.

1.8 Optogenetics

Under resting conditions, electrically excitable cells demonstrate a transmembrane potential difference caused by a build-up of positive and negative charges along the cell membrane. (Figure 1.3A) The resting membrane potential is negative relative to the outside due to the ionic composition of the intracellular and extracellular fluids. An action potential is triggered when the membrane potential becomes increasingly positive and reaches a threshold value for the opening of voltage sensitive ion channels. In cardiac physiology, the increase in membrane potential arises from the pacemaker current found in cells within the sino-atrial node. The membrane potential can be artificially made more positive using electric field stimulation. Negative charge from the cathode displaces positive charge from the external membrane causing an increased external negative charge. This in turn repels negative charge from the internal

side of the membrane causing the membrane potential to become more positive and activating voltage-gated ion channels (Figure 1.3B).

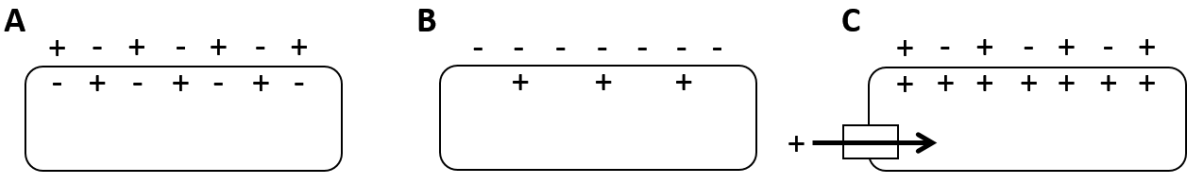

Figure 1.3 Optogenetic stimulation vs field stimulation
A) Representative diagram of charge distribution in an excitable cell at rest (resting membrane potential). B) Field stimulation displaces positive charge from the outside of the outside of the cell membrane leading to a more positive membrane potential. C) Current injection through a cation channel (optically activated or otherwise) causes positive charge to accumulate on the inner membrane around the channel leading to a more positive membrane potential.

The effectiveness of field stimulation is heavily dependent on the material the electrode is comprised of; the distance between the cell and the electrode; and the composition of any surrounding tissue[102]. Alongside these variables there are several disadvantages associated with field stimulation. Long periods of stimulation, and even short repetitive bursts of stimulation can cause electrolysis of the extracellular solution leading to changes in pH and the production of free radicals, both of which can cause cell damage. Field stimulation is also confounded by a lack of selectivity. All cells within the electric field undergo stimulation meaning it is impossible to achieve patterned stimulation.

These limitations can be avoided through the use optogenetic stimulation. Optogenetics is the use of light activated proteins to control or monitor the behaviour of excitable cells[103]. In the majority of studies, this translates to the addition of light-sensitive ion channels, however optogenetics also covers the use of fluorescent sensor proteins that respond to changes in cell membrane potential or calcium concentration[104-106]. There are a large variety of light activated ion channels, most of which are depolarising whilst a few others are hyperpolarising[107].

One of the most widely used ion channels is chanelrhodopsin-2 (ChR-2)[108-110]. Channelrhodopsin-2 is a 7 transmembrane α helix protein[108] which when illuminated with 400-500 nm[111] light produces a photocurrent characterised by an initial peak followed by a reduced but sustained steady state current until cessation of illumination[108]. The photocurrent is caused by isomerisation of the

all-trans-retinal complex to C13-cis-retinal[111] causing a conformational change within the pore region of the protein. This in turn allows cations to enter the cell causing depolarisation[108,109](Figure 1.3C).

As only cells that express the protein are stimulated, optogenetics has proven useful for neuroscience as specific cell types can be targeted meaning that the exact anatomical structure does not need to be known[103,112]. In addition to this, the multitude of different optogenetic channels means that cells can be both stimulated or inhibited which can allow for behavioural modulation[113-115].

The field of cardiac electrophysiology has also seen an increase in the use of optogenetic proteins because of the number of advantages it has over traditional field electrodes. The increased spatiotemporal resolution of optogenetic stimulation allows specific sub-regions of the myocardium to be selectively stimulated, creating stimulation patterns that can disrupt re-entrant arrhythmias with minimal risk of secondary pro-arrhythmic effects[116,117]. As there is no need for an electric shock, pain and damage caused by implantable automatic defibrillators[118-120] could potentially be avoided using optogenetic defibrillators.

An important consideration when comparing field stimulation to optogenetic stimulation is how the magnitude of the change in transmembrane potential (ΔV) relates to increasing stimulus strength and how this relationship is altered by changes in resting membrane potential. Field stimulation causes a surface potential gradient which, as the cell interior is isopotential, causes a spatially varying transmembrane potential difference throughout the cell, leading to ion channel activation and depolarisation[121]. ΔV increases with increasing field strength, and is largely unaffected by membrane potential[122]. Optogenetic stimulation, by comparison, causes a ΔV by injection of a photocurrent. ChR-2 photocurrent, and therefore ΔV, increases non-linearly with light intensity[123], with saturation reflecting activation of all available channels[124]. ChR-2 also shows strong inward rectification[109] meaning that, unlike field stimulation, ChR-2 ΔV is heavily dependent on membrane potential.

1.8.1 Optogenetic maturation of iPSC-CMs

It was hypothesised that, through careful patterning of optogenetic stimulation, the directional electrical activity observed at day 22 within the developing heart (Figure 1.1) could be replicated within a monolayer of iPSC-CMs. By mimicking embryonic electrophysiological conditions, the maturity of commercially available iPSC-CMs could be improved.

1.9 Aims of project

The aim of this project was to investigate the use of optogenetic stimulation, via ChR-2, as a means of altering cardiomyocyte phenotype. More specifically the project aimed to:

1) Determine optimal virus load for effective ChR-2 transfection in iPSC-CMs

2) Assess equivalence of optogenetic and field stimulation in iPSC-CMs.

3) Trial long term photostimulation protocols on iPSC-CMs and test the effect on structural and functional phenotype.

4) Determine the effect of directional electrical activation on structural and functional phenotype.

Chapter 2: General Methods

2.1 Solutions

For plating and maintenance of iPSC-CM's, Cor4U media was used. For fixing and imaging cells phosphate buffered saline was used.

2.1.1 Cor4U media

Cor4U cell plating and maintenance media was provided by Axiogenesis. For plating, media was supplemented with 3 μM puromycin to prevent fibroblast growth. For chronic pacing experiments, media was supplemented with 1% penicillin and streptomycin.

2.1.2 Phosphate Buffered Saline (PBS)

2.67 KCl, 1.47 KH2PO4, 138 NaCl and 8 Na2HPO4-7H2O (concentrations in mM). 1% bovine serum albumin (BSA) (by mass) was added for use in immunohistochemistry.

2.2 Methods

2.2.1 Cell plating and viral transfection

Glass bottomed culture dishes were coated with 1:100 fibronectin (Sigma Aldrich):PBS (with Ca^{2+} and Mg^{2+}). The plates were then left at 37°C for 3 hours before the fibronectin was removed. A cryovial containing 1 million Cor4U cardiomyocytes (Axiogenesis, Germany) was removed from liquid nitrogen storage and 500 μl of prewarmed Cor4u media was then added before the cryovial was warmed in a water bath at 37°C until the pellet of cells detached. The cells and media were then removed from the cryovial and added slowly to a 50ml falcon tube containing 3ml prewarmed media. The cryovial was then washed with a further 1ml of media which was then added to the falcon tube resulting in a final volume of 5ml. 10 μl of the cell suspension was added to 10 μl trypan blue before being added to a haemocytometer for counting. After counting the media volume was altered such that the cell concentration was 250,000 cells/ml for seeding in inserts or 125,000 cells/ml for seeding in 96 well plates. Cells were then seeded at a density of 25,000 cells per well and then

kept in an incubator overnight. The media was replaced as early as possible the following day to remove any remaining cryopreservatives.

It was at this point that channelrhodopsin-2 was introduced into the cells via an adeno associated virus (AAV1.CAG.hChR2(H134R)-mCherry.WPRE.SV40). The 1.17×10^{13}GC/ml stock was split into 2 µl aliquots to prevent repeat freeze-thaw cycles. For transfection, a 2 µl aliquot was added to 1ml cell media resulting in a solution of 2.34×10^{10} GC/ml. The appropriate volume for the selected multiplicity of infection (MOI) was then added to each well to be transfected. For example, an MOI of 2,500 at a cell density of 25,000 would require 6.25×10^{7} genome copies (GC) meaning 2.67 µl of the diluted viral solution was added to each well. The cells were left in the presence of virus for 24 hours, at which time the viral solution was removed, and fresh media added. Media was subsequently replaced every 48 hours. The media containing viral particles and any plastic or glassware used in transfection was treated with bleach overnight before disposal as a safety precaution.

2.2.2 Optical stimulation

A 470 nm LED (Cairn research) was used to optically stimulate cells via an Olympus IX71 Microscope with a 40x objective. The minimum optical power of the LED was reduced using a 10% neutral density (ND) filter (Comar). Pulsed illumination was possible by controlling the power level of the LED using an external Digitimer DS2A stimulator coupled to a Digitimer DG2A train generator (Figure 2.1). Using this setup, the minimum optical power required to pace cells with 1:1 coupling was recorded.

2.2.3 Strength duration curves

Starting with a 20 ms pulse width, photostimulation intensity was increased until 1:1 coupling occurred. The pulse width was then reduced and the photostimulation intensity increased to the new threshold. This was repeated until the threshold intensity exceeded the maximum output of the LED. Rheobasic current (the threshold power at an “infinite” pulse width) and the chronaxie (the pulse width at which the threshold is twice the rheobasic power) were taken from the resulting plot of power vs pulse-width.

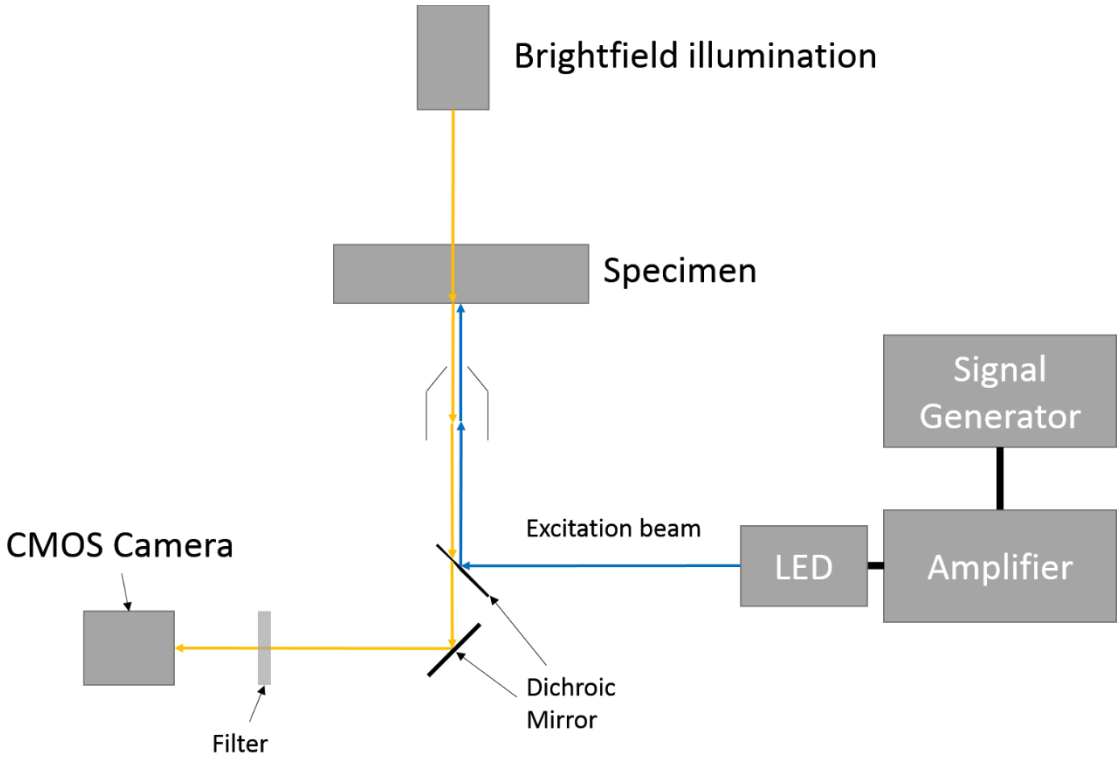

Figure 2.1 Photostimulation optical pathway
Optical pathway diagram of microscope setup used for photostimulation. A 470 nm LED was powered by a Cairn research opto-LED power supply. A Digitimer DS2A stimulator coupled to a Digitimer DG2A train generator was used to control the optical power level.

2.2.4 Contractility recordings

Contracting cells were recorded at 100 frames per second for 8-10 seconds using a Hamamatsu orca flash 4.0 camera in conjunction with HCI imaging software. Brightfield illumination was used throughout recording and the level was unchanged between recordings to prevent changing levels of background ChR-2 activation. To conserve disk space and reduce memory usage a 600x600 pixel sub-array was used instead of the full sensor area. The resulting image sequence was then analysed using an algorithm developed by Dr Francis Burton which has since been further developed into an automated, open source software tool (MUSCLEMOTION)[125]. Absolute changes in pixel intensity between a reference frame and the frame of interest allow for contraction to be assessed. For every pixel within the frame of interest, the equivalent pixel in the reference frame is subtracted and the difference is presented in absolute numbers. Unchanged pixels result in low values, while changed pixels result in higher values. The mean pixel intensity of the resulting image gives a quantifiable measure of pixel displacement.

When all frames within an image sequence are compared to a common reference frame (img_i -img_{ref} = img_{result}) the output describes the total displacement over time. If the reference frame is dependent upon the frame of interest (img_{ref} = img_{i-1}) the output describes the relative interframe displacement defined as contraction velocity. An exert from Sala et al describes several improvements made to the algorithm:[125]

> "MUSCLEMOTION has been modified to handle typical experimental recordings by (i) improving the signal-to-noise ratio (SNR), (ii) automating reference frame selection and (iii) programming built-in checks to validate the generated output data. The SNR was increased by isolating the pixels of interest in a three-step process: i) maximum projection of pixel intensity in the complete contraction stack, ii) creation of a binary image of this maximum projection with a threshold level equal to the mean grey value plus standard deviation and iii) multiplication of the pixel values in this image by the original contraction and speed of the contraction image stack. This process allowed the algorithm to work on a region of interest with movement above the noise level only" (Figure 2.2 Schematic overview of MUSCLEMOTION).

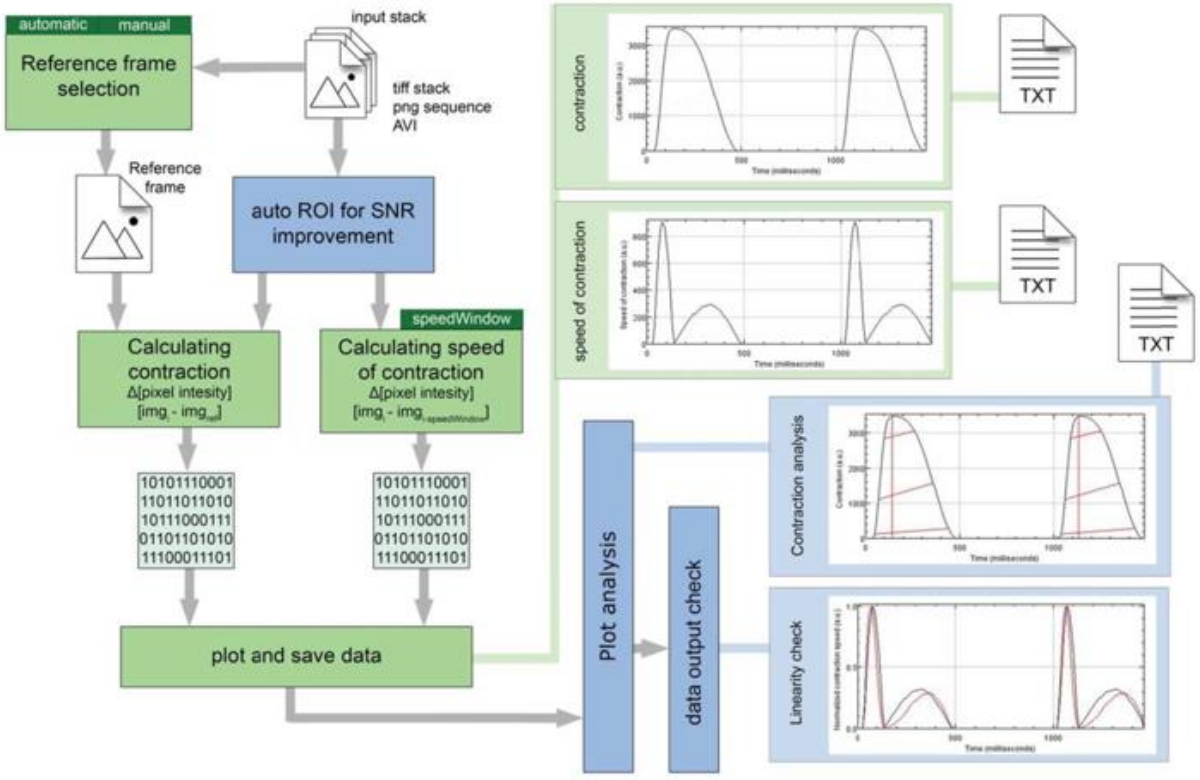

Figure 2.2 Schematic overview of MUSCLEMOTION
Green blocks indicate basic steps of the algorithm. Dark green blocks indicate important user input choices. Plots within light green blocks indicate results. Optional steps are shown in blue blocks, with graphical representation of the analysed parameters indicated by red lines. Three result files are generated containing the raw data: "contraction.txt", "speed-of-contraction.txt" and "overview-results.txt". Furthermore, three images showing relevant traces and a log file are generated and saved (not shown in schematic). Figure adapted from Sala et al[125]

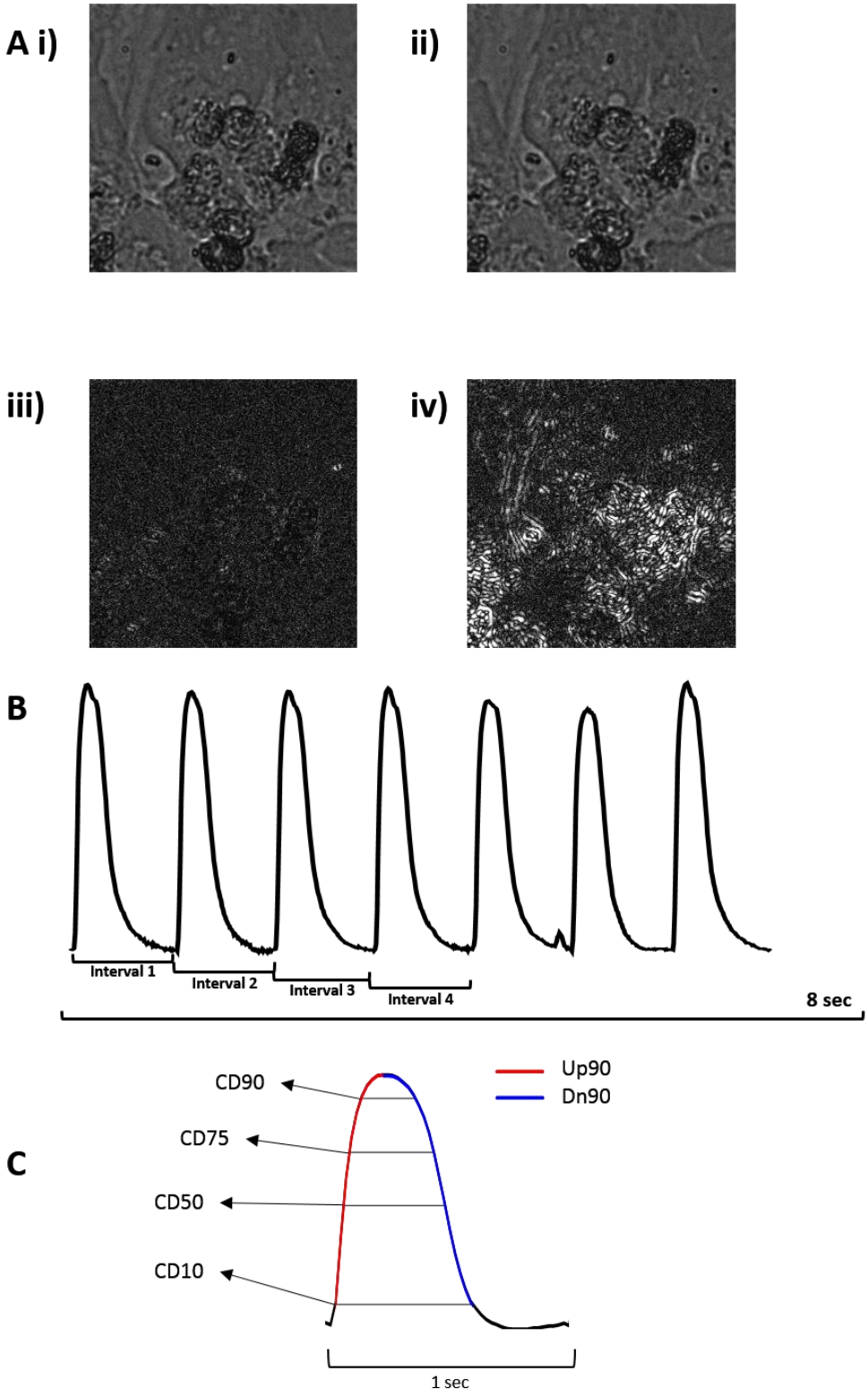

Figure 2.3 Example of contractility analysis
A) i) Brightfield reference image. ii) Brightfield image at peak contraction. iii) Result image of reference frame subtracted from non-displaced frame. iv) Result image from reference image subtracted from frame at maximum displacement. B) Example output showing train of contractions. E) Visual breakdown of the parameters obtained from contraction analysis. The upstroke time (Up90 red) and downstroke time (Dn90 blue) are output alongside the contraction duration (CD) at 10,50,75 and 90% peak contraction.

Using the exposure time of the frames of interest, several contraction parameters can be determined. The beat-to-beat cycle length along with the duration of the upstroke (Up90 – time from 10% contraction to peak contraction) and downstroke (Dn90 – time from peak contraction to 10% contraction) phases of contraction can be determined. The cycle durations at various levels of contraction are also output by the algorithm (e.g. CD50 – time for 50% contraction after peak minus time for 50% contraction before peak) (Figure 2.3). As contraction amplitude is relative, and therefore heavily influenced by changes in light intensity and cell position, it was not used for the majority of experiments.

MUSCLEMOTION has been validated against gold standards in several cell systems (optical flow measurements in hiPSC-CMs, post deflection in engineered heart tissues, and sarcomere length fractional shortening in adult cardiomyocytes). MUSCLEMOTION correlated well with optical flow in isolated hiPSC-CMs (R^2 = 0.916) (Figure 2.4a v), hiPSC-CM monolayers (R^2 = 0.803)(Figure 2.4b v) and hiPSC-derived cardiac organoids (R^2 = 0.747) (Figure 2.4c v). MUSCLEMOTION also correlated well with post deflection in engineered heart tissues (R^2 = 0.879) (Figure 2.4d v) and sarcomere length fractional shortening for adult rabbit ventricular cardiomyocytes (R^2 = 0.871) (Figure 2.4e v)[125].

Throughout this project, for consistency and accuracy, only areas of iPSC-CM monolayers that showed heterogeneous contraction upon manual observation were recorded and analysed using the MUSCLEMOTION algorithm. The typical distribution of contractility parameters obtained throughout this project are shown in Figure 2.5. Spontaneous cycle length was not normally distributed with greater than 90% of cells having spontaneous frequency between 0.5 and 3Hz. As Up90, Dn90 and contraction durations are heavily influenced by the beating rate of cells, they also displayed non-normal distributions.

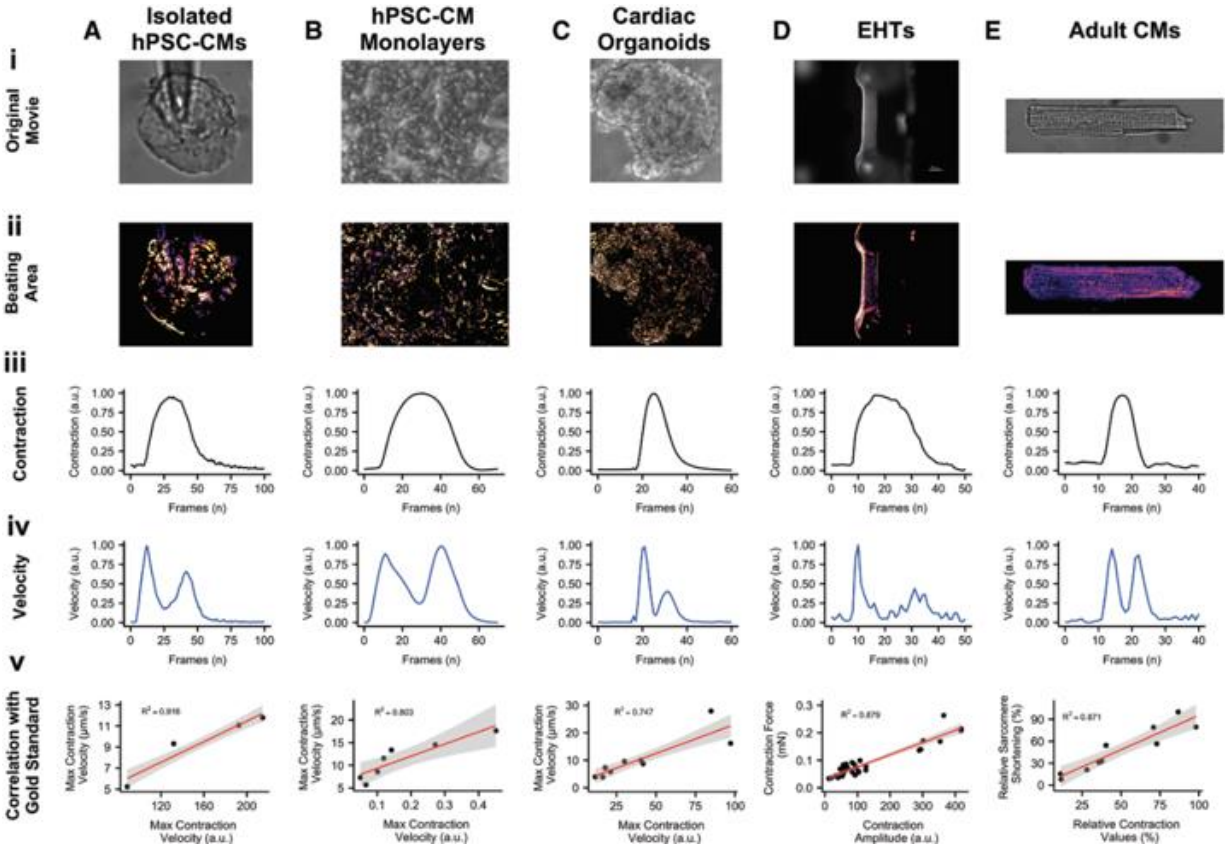

Figure 2.4 Correlation of results with gold standards

Figure and caption obtained from Sala et al[125]. a) Brightfield image of isolated hiPSC-CMs (i), with maximum projection step visually enhanced with a fire Look Up Table (ii), contraction (iii) and velocity (iv) profiles of each individual beat have been generated by MUSCLEMOTION and temporally aligned; linear regression analysis between MUSCLEMOTION results (x-axis) and optical flow results (y-axis) (v). b) Phase contrast image of hiPSC-CM monolayers (i), with maximum projection step visually enhanced with a fire Look Up Table (ii), contraction (iii) and velocity (iv) profiles of each individual beat have been generated by MUSCLEMOTION and temporally aligned; linear regression analysis between MUSCLEMOTION results (x-axis) and those obtained with optical flow results (y-axis) (v). c) Phase contrast image of cardiac organoids (i), with maximum projection step visually enhanced with a fire Look Up Table (ii), contraction (iii) and velocity (iv) profiles of each individual beat have been generated by MUSCLEMOTION and temporally aligned; linear regression analysis between MUSCLEMOTION results (x-axis) and those obtained with optical flow results (y-axis) (v). d) Live view of an EHT during contraction analysis. Scale bar = 1 mm. (i), with maximum projection step visually enhanced with a fire Look Up Table (ii), contraction (iii) and velocity (iv) profiles of each individual beat have been generated by MUSCLEMOTION and temporally aligned; linear regression analysis between MUSCLEMOTION results (x-axis) and those obtained with post deflection (y-axis) (v). e) Brightfield image of adult rabbit CMs (i), with maximum projection step visually enhanced with a fire Look Up Table (ii); contraction (iii) and velocity (iv) profiles of each individual beat have been generated by MUSCLEMOTION and temporally aligned; linear regression analysis between MUSCLEMOTION results (x-axis) and those obtained from sarcomere fractional shortening calculation with Fast Fourier Transform (y-axis) (v).

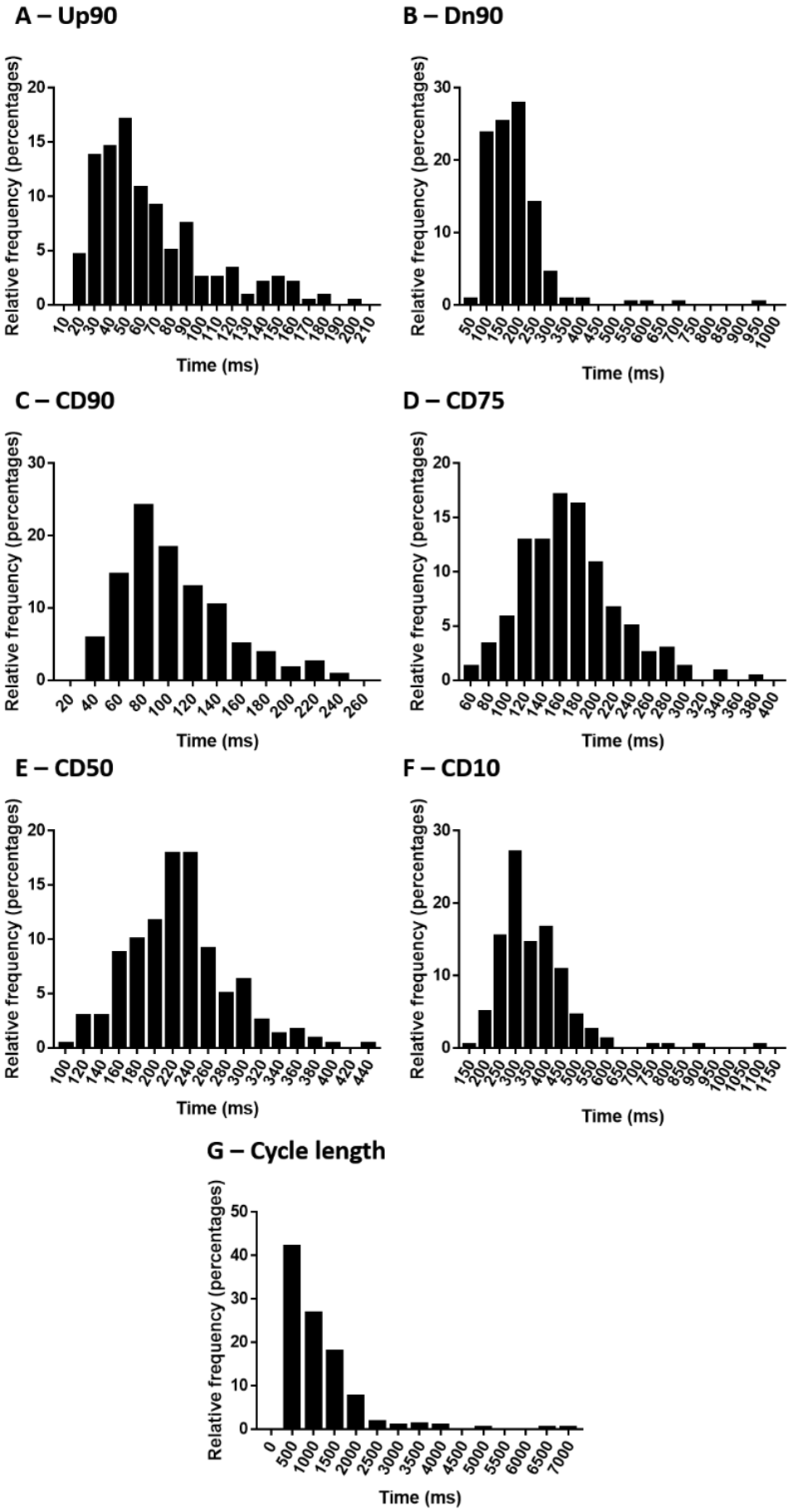

Figure 2.5 Typical variation in spontaneous contractility parameters
Histograms showing distribution of spontaneous measurements of A) Up90, B) Dn90, C) CD90, D) CD75, E) CD50, F) CD10 and G) Cycle length. N = 240 cell areas.

2.2.5 Optical dyes

2.2.5.1 Di-4-anepps

Di-4-anepps is a voltage sensitive dye with a peak excitation of 482 nm (Figure 2.6) and peak emission of 686 nm. Using photomultiplier tubes (PMTs) to detect emissions from either side of the peak, ratiometric voltage measurements can be performed. Membrane depolarisation causes a reversible change in peak emission towards a shorter wavelength. When this occurs, the signal from the short wavelength PMT increases while the signal from the long wavelength PMT decreases. The ratio of these two signals can be used to monitor changes in membrane potential and give several useful metrics such as various action potential durations. Ratiometric dyes such avoid several of the artefacts (movement, photobleaching) that plague non-ratiometric dyes such as fluovolt, however the imaging equipment required is more complex. The photostimulation apparatus (Figure 2.1) was adapted from the system used for voltage measurements. As channelrhodopsin-2 and di-4-anneps share similar excitation spectra (Figure 2.6), di-4-anneps could not be used in conjunction with photostimulation.

2.2.5.2 Fura-2

Fura-2 is a ratiometric calcium indicator that can be calibrated to give optical measurements of absolute calcium levels. Unlike voltage measurement with di-4-anepps, which excites at 1 wavelength and monitors 2 emission wavelengths, calcium measurements with fura-2 excites with 2 wavelengths, typically 340 nm and 380 nm, and records emission at 1 wavelength, typically 510 nm (Figure 2.6). When excited at 340 nm an increase in free calcium concentration causes an increase in fluorescence but causes a decrease in fluorescence when excited at 380 nm. The fluorescence ratio of 340/380 increases linearly with increasing calcium concentration (0-3000 nm) and independently of fura concentration[126]. While measurement of cytoplasmic calcium levels would be useful for this project it was unclear how 340 or 380 nm illumination will interact with channelrhodopsin-2 as action spectra for the ion channel have not been recorded at wavelengths shorter than 390 nm[127]

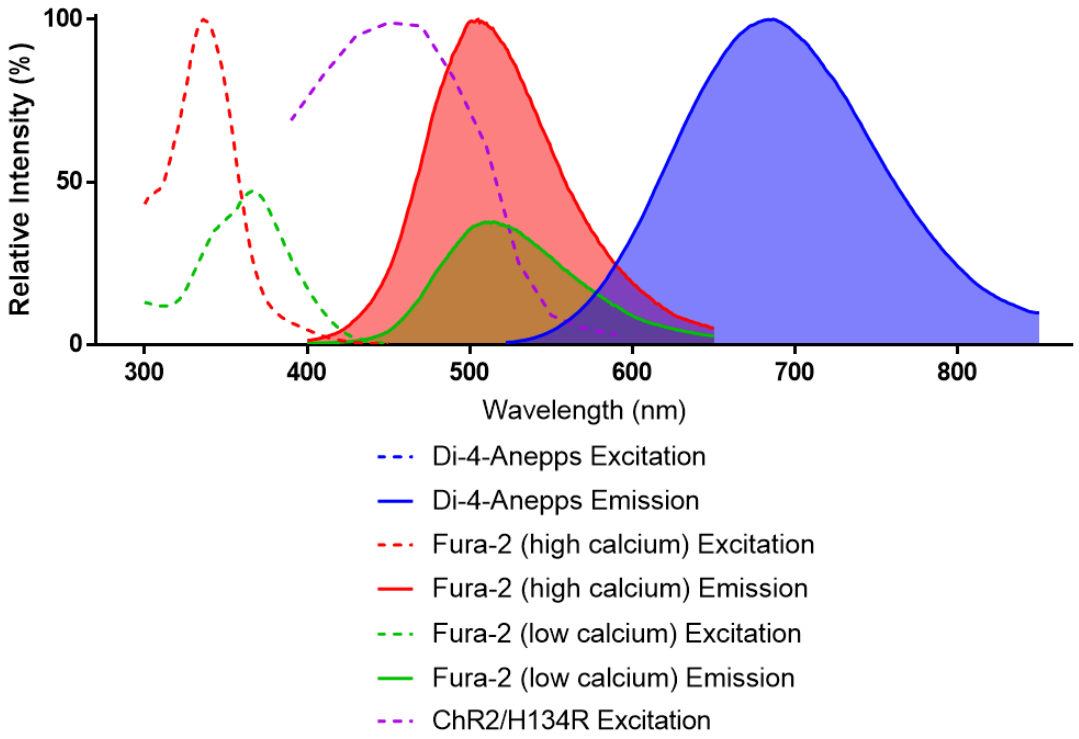

Figure 2.6 Excitation spectra for Di-4-anepps, Fura-2 and ChR2
Excitation and emission spectra for Di-4-Anepps, Fura-2 (calcium bound) and Fura-2 (calcium free) were obtained from thermofisher spectraviewer. Spectra for Channelrhodopsin-2(H134R mutant) recreated from Lin et al[127] supplemental material.

2.2.6 Cell fixing

Cell media was removed and replaced with 2% paraformaldehyde (PFA) in PBS. The PFA was removed after ten minutes and the cells were washed 3 times in PBS. Fixed cells were then stored at 4°C for a maximum of 3 weeks before being used for immunohistochemistry.

2.2.7 Immunohistochemistry

Fixed cells were placed in a 0.2% triton 1% BSA PBS solution for 10 minutes in order to permeabilise the cells. They were then washed for 10 minutes in 1% BSA PBS 3 times before being blocked for an hour with a 10% goat serum, 1% BSA PBS solution. After blocking, cells were washed once for 10 minutes using 1% BSA PBS. The cells were then covered with a PBS solution containing 3% goat serum, 1% BSA and 0.2% mouse anti-α-actinin primary antibody (Invitrogen) and stored at 4°C overnight. After primary staining was completed the cells were washed 3 times in 1% BSA PBS before being covered with a secondary antibody PBS solution containing 1% BSA and 0.5% goat anti-mouse alexafluor 647 secondary antibody for 1.5 hours. Cells were then washed with standard PBS 3 times before imaging.

2.2.8 Cell imaging

Stained cells were placed on an Olympus IX83 confocal microscope under 40x magnification. 40x magnification was used to allow sarcomeres to be resolved while avoiding the application of lens oil required at higher magnification. The focal point was found using brightfield illumination before illumination was switched to 637 nm laser light (Obis continuous wave laser, Coherent, USA) with a 700/75 nm emission filter for visualisation of α-actinin. 561 nm laser light (Obis continuous wave laser, Coherent, USA) with a 595/50 nm emission filter was used for visualisation of mCherry (Figure 2.7). A Cairn research opto-spin filter controller was used to change emission filters. Minimal laser power was used in order to prevent significant photobleaching and a standard exposure time of 200 ms and an EM gain of 300 was used for the majority of images but was adjusted if required. Due to the nature of the cellular monolayer, it was often the case that the full sarcomere could not be imaged in a single focal plane. As long as the distance between the top and the bottom of the sarcomere was small (<10 μm) a z-stack of the sarcomere area was taken. Using Metamorph imaging software, the IX83s focus motor (to allow fine automated control of the height of the objective lens) and an Evolve 512 Delta EMCCD camera (Photometrics, USA), a series of images at varying points on the z axis but fixed points on the x and y axis was acquired. Focal depth was controlled using an X-light confocal imager with a 70 μm pinhole disc spinning at 1500rpm (Crest, Italy) The resulting “z-stack” was then used in a maximum intensity projection to increase the usable area of α-actinin. Only those cells with clearly defined sarcomeres, that had no overlapping cells were selected for analysis.

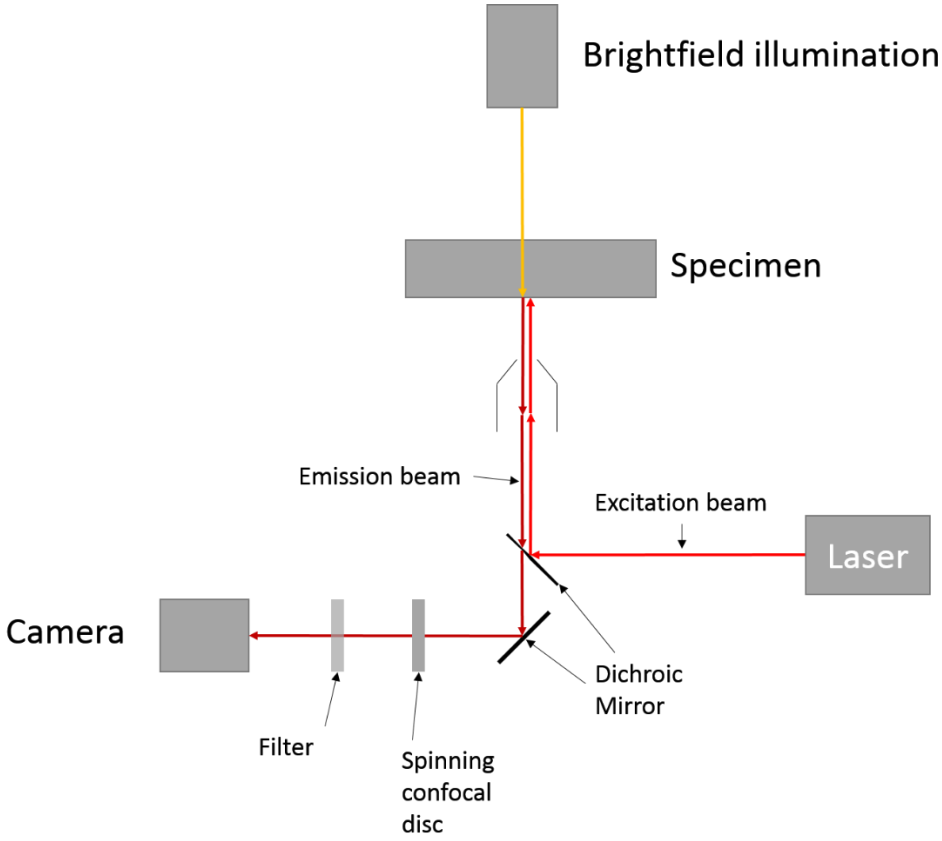

Figure 2.7 Optical pathway for confocal microscope
Optical pathway diagram showing microscope set-up used for visualisation of α-actinin and mCherry. 637 nm laser light was used in conjunction with a 700/70 nm emission filter for visualisation of α-actinin while 561 nm illumination and a 595/50 nm emission filter was used to visualise mCherry.

2.2.9 Image analysis

FIJI[128] (an open-source image analysis software) was used to determine sarcomere length, inhomogeneity and alignment. Sarcomere images first had their background subtracted using a rolling ball radius of 2.0. Areas of usable sarcomere were selected, and the image was manually thresholded to produce a binary image. The FIJI plugin “Skeletonise 2d/3d” was used to produce a skeletonised image. Another FIJI plugin, “Directionality”, was used to determine the sarcomere alignment from the skeletonised image (Figure 2.1 E). This method was adapted from a t-tubule analysis method[129]. Sarcomere length and inhomogeneity were determined by applying a fast Fourier transform (FFT) to the skeletonised sarcomere image. The resulting spatial frequency was then plotted (Figure 2.8 D) and the sarcomere length was determined by taking the reciprocal of the fundamental frequency, whereas the sarcomere inhomogeneity was taken as the full width at half maximum of the first order peak (FWHM)[130]. A 1 mm stage micrometer with 0.1 and 0.01 mm divisions was used as a to confirm results.

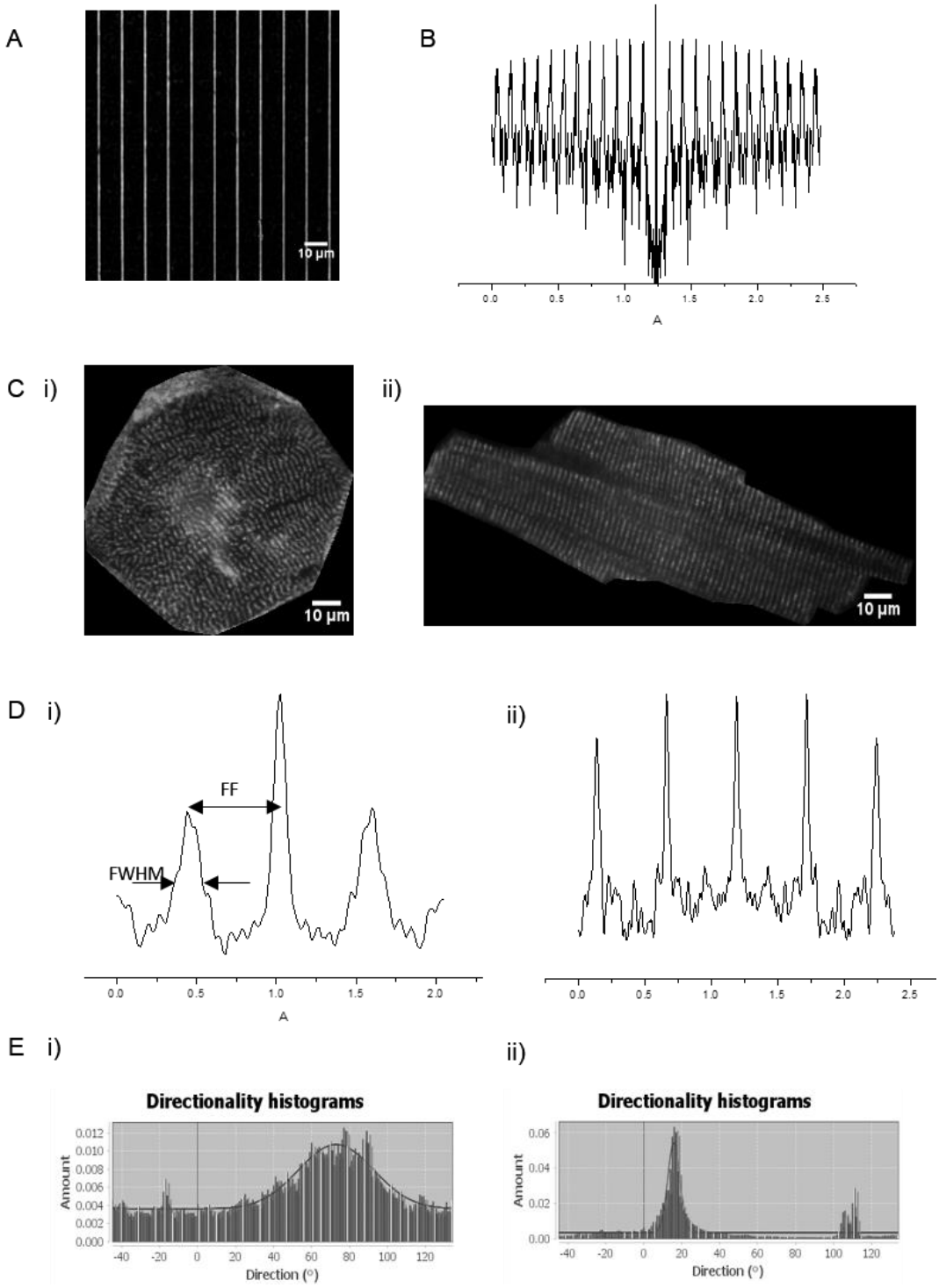

Figure 2.8 Sarcomere analysis
Example images of sarcomeric analysis. A) 0.01 mm stage micrometer divisions, B) Fourier transform of stage micrometer image. C) α-actinin staining in i) an iPSC-CM and ii) an adult rat ventricle cell. D) show the resulting Fourier transform which was then used to calculate sarcomere length (FF= fundamental frequency) and inhomogeneity (FWHM= full-width half maximum) in i) iPSC-CMs and ii) adult rat ventricle cells. E) Output of the ImageJ Directionality plugin that was used to quantify sarcomere alignment in i) iPSC-CMs and ii) adult rat ventricle cells.

2.2.10 Commercially available iPSC-CMs have a markedly different sarcomeric structure from isolated adult cardiomyocytes

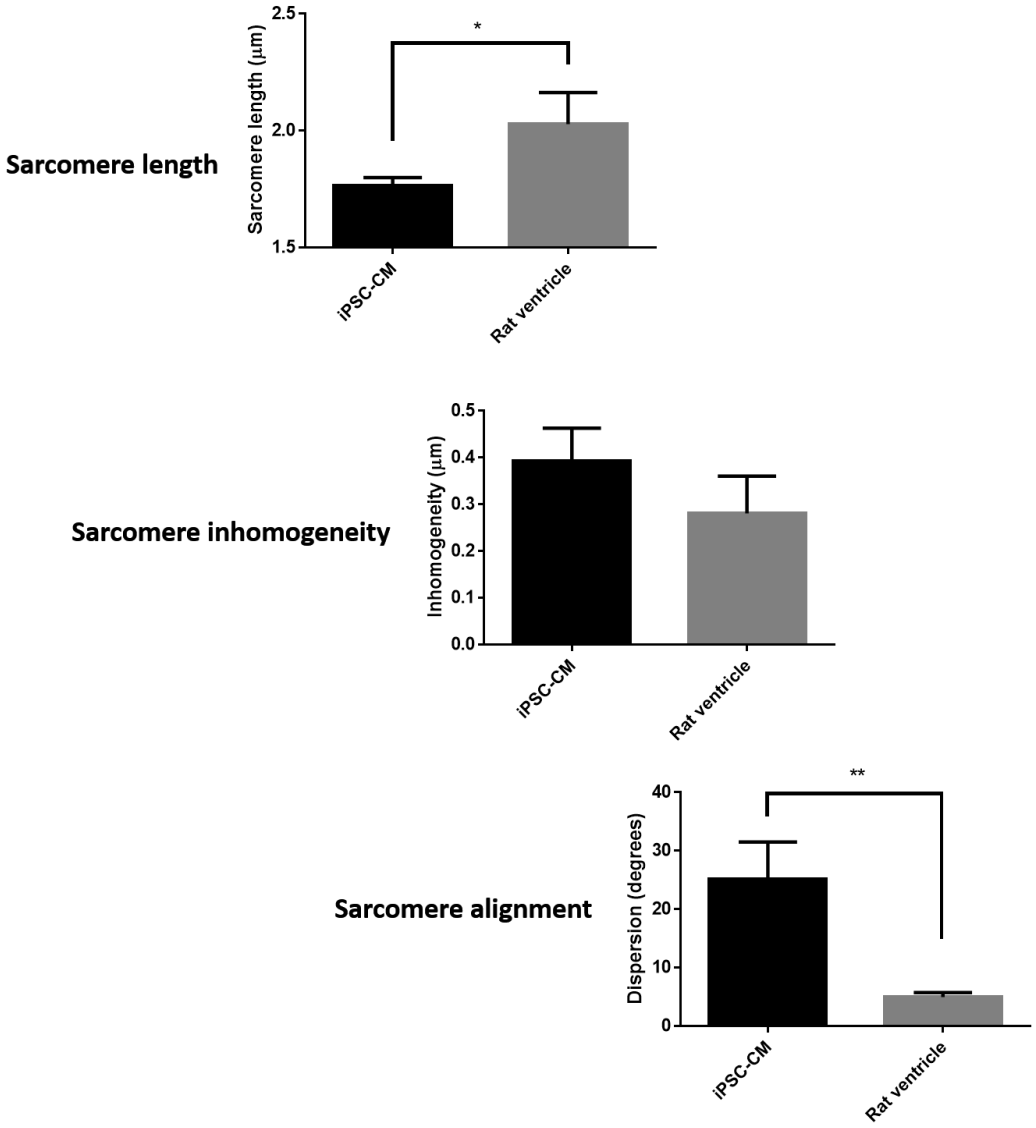

Figure 2.9 Baseline comparison of cell structure
Sarcomere length was significantly longer in adult cardiomyocytes (N= 3 animals, 10 cells/animal) when compared to iPSC-CMs (N=4 wells, 10 cells/well) (1.766 ± 0.017 µm vs 2.028 ± 0.079 µm respectively, P=0.0125 unpaired t-test). Middle) Sarcomere inhomogeneity in iPSC-CMs was comparable to adult cells (0.39 ± 0.035 µm vs 0.28 ± 0.046 µm respectively, P=0.1024). Right) adult cardiomyocytes are vastly more polarised than iPSC-CMs (4.98 ± 0.44° vs 25.22 ± 3.15° respectively, P=0.0029 unpaired t-test).

Fourier analysis of the 0.1 mm stage micrometer divisions gave a length of 100 µm while the 0.01 gave a length of 10 µm. iPSC-CMs had a significantly shorter sarcomere length, when compared to isolated adult rat ventricular cells (1.766 ± 0.017 µm vs 2.028 ± 0.079 µm respectively, P=0.0125 unpaired t-test. Figure 2.9). The sarcomere inhomogeneity however, was not significantly different between the iPSC-CMs and the adult ventricle cells (0.39 ± 0.035 µm vs 0.28 ±

0.046 µm respectively, P=0.1024. Figure 2.9). By far the starkest contrast between the iPSC-CMs and adult cells was the sarcomere alignment. The spatial frequency spectra of the mainly circular iPSC-CMs covers a much larger range of angles (25.22 ± 3.15°) than the polarised adult cardiomyocytes (4.98 ± 0.44°, P=0.0029, unpaired t-test. Figure 2.9). These results are the baseline measurements that were used throughout this project and are discussed in detail in chapter 4.

Chapter 3: Optimisation and validation of channelrhodopsin based photostimulation

3.1 Introduction

3.1.1 Axiogenesis Cor4U

Cor4U cells are an iPSC-CM cell line generated by Axiogenesis using the Yamanaka method of generating iPSC from dermal fibroblasts[40]. Human Fibroblasts (from a 28-year-old Caucasian female donor) were used to generate iPSC cells via virus-free plasmid transfection. Two vectors were used for transfection, each containing two of the pluripotency-associated genes Klf4, c-Myc, Oct3/4 and Sox2. Vectors I and II were approximately 8kb and 7kb in size, with a beta-actin promoter. Cardiomyocyte differentiation was driven by a 9.5kb plasmid vector which was used to insert the cardiomyocyte specific alpha MHC promotor and the puromycin resistance cassette. The antibiotic resistance this conferred was used to increase the purity of the cardiomyocyte culture to 100%. Due to their human background they are an ideal substrate for cardiotoxic drug testing[131]. These cells however do demonstrate many of the disadvantages associated with their immature phenotype[132].

3.1.2 Channelrhodopsin-2

ChR-2 is a light-gated cation channel derived from the green algae *Chlamydomonas reinhardtii*[108]. The H134R gain of function variant used in this project arises from a single point mutation from histidine to arginine at histidine residue 134 which results in an increased photocurrent[109].

Peak photocurrent occurs at 450 nm illumination however approximately 60% peak current can be induced by 390 nm light[127].The blue shifted activation spectra allows channelrhodopsin expressing cells to be optically paced using a 470 nm led normally used for voltage sensitive dyes. This also means that illumination with 470 nm light with sufficient intensity to fluoresce such optical dyes would also activate channelrhodopsin meaning photostimulation and optical voltage sensing may be incompatible. Data regarding activation at shorter wavelengths could not be found, however it is possible that illumination with 380, or 340 nm, the illuminations used by ratiometric calcium dyes such as fura, could cause a photocurrent to be injected and alter cell electrophysiology.

3.1.3 Strength duration curve

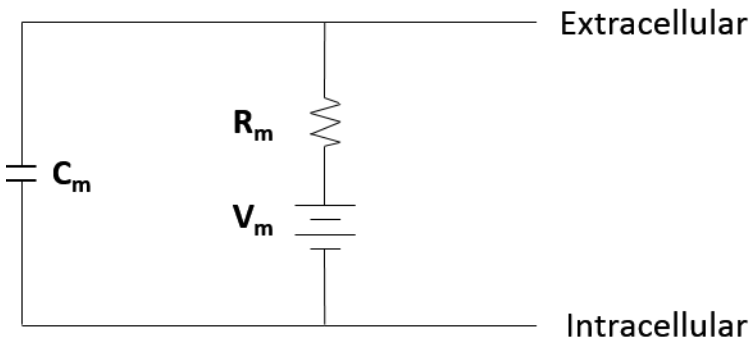

Figure 3.1 Plasma membrane equivalent circuit diagram
Equivalent circuit diagram representing a patch of plasma membrane. C_m represents the membrane capacitance, R_m represents the membrane resistance to ion flux, and V_m represents the potential difference across the membrane.

The membrane of an excitable cell can be represented, somewhat simplistically, by an electric circuit diagram. The impermeant nature of the plasma membrane causes it to act like a capacitor (C_m), while the restricted flow of ions through ion channels acts like a resistor (R_m). Differences in ion concentrations between the intracellular and extracellular solutions cause opposing charges to build up either side generating a potential difference across the membrane (V_m). At rest, this potential difference is maintained by and can be calculated using the Goldman-Hodgkins-Katz equation (Equation 3.1) and is approximately -90mV in ventricular cells.

Equation 3.1 Goldman-Hodgkin-Katz equation
Where E_M is the resting membrane potential, R is the universal gas constant, T is the absolute temperature in kelvin, F is the Faraday constant, P is the relative membrane permeability to ion x $[x]_o$ is the extracellular concentration of ion x and $[x]_i$ is the intracellular concentration of ion x.

$$E_M = \frac{RT}{F} \ln\left(\frac{P_{Na^+}[Na^+]_o + P_{K^+}[K^+]_o + P_{Cl^-}[Cl^-]_i}{P_{Na^+}[Na^+]_i + P_{K^+}[K^+]_i + P_{Cl^-}[Cl^-]_o}\right)$$

When an inward current is injected into the cell, the membrane potential becomes depolarised. When the membrane potential reaches a certain value, voltage-sensitive Na^+ ion channels open causing an inward current further depolarising the membrane and initiating an action potential. The membrane potential this occurs at is referred to as the threshold potential. To reach threshold potential the current stimulus (I) must supply sufficient charge (Q) within the duration (t) of the stimulus $\left(I = {}^{Q}/_{t}\right)$. The charge required is

determined by the threshold potential (V_t) and the capacitance (C) of the cell membrane ($Q = V_t C$). The threshold current (I_t) is therefore directly related to the cell capacitance and threshold potential ($I_t = {}^{V_t C}/_{t}$). Assuming capacitance and threshold potential are fixed, the threshold current is inversely related to the duration of the stimulus ($I_t = {}^{1}/_{t}$) giving rise to the strength-duration curve (Figure 3.2(A)) from which, 2 useful cell characteristics can be determined. Rheobase, the minimum current required to reach threshold with a stimulus pulse of infinite duration, and chronaxie, the duration of a pulse with twice the rheobasic strength.

The strength-duration curve, although it has limitations[7], is a useful tool for comparing the excitability of different tissues and has been used to show excitability changes in response different drugs. Both chronaxie and rheobase have been shown decrease upon the addition of caffeine (likely due to sensitisation of RyR2 as well as indirect effects on calcium channels due to phosphodiesterase inhibition)[133], and increase upon exposure to quinidine[134,135], bunapthine[136] and propafenone[137]. Strength duration curves have also been used to show the effect of denervation on the excitability of skeletal muscle. Denervation of rabbit limb muscle caused a transient increase in rheobase that normalised overtime, this was accompanied by a permanent increase in chronaxie demonstrating the reduction in excitability caused by degeneration of the motor endplates[138].

In the context of this project, the strength-duration curve is useful as it allows for iPSC-CM excitability to be compared between ChR-2 and field stimulation, as well as revealing any changes in excitability caused by chronic photostimulation.

3.1.4 Aims

The aims of this chapter were to:

1) Determine optimal virus load for effective ChR-2 transfection in iPSC-CMs

2) Assess equivalence of optogenetic and field stimulation in iPSC-CMs

3) Assess feasibility of using optical dyes in conjunction with optogenetics.

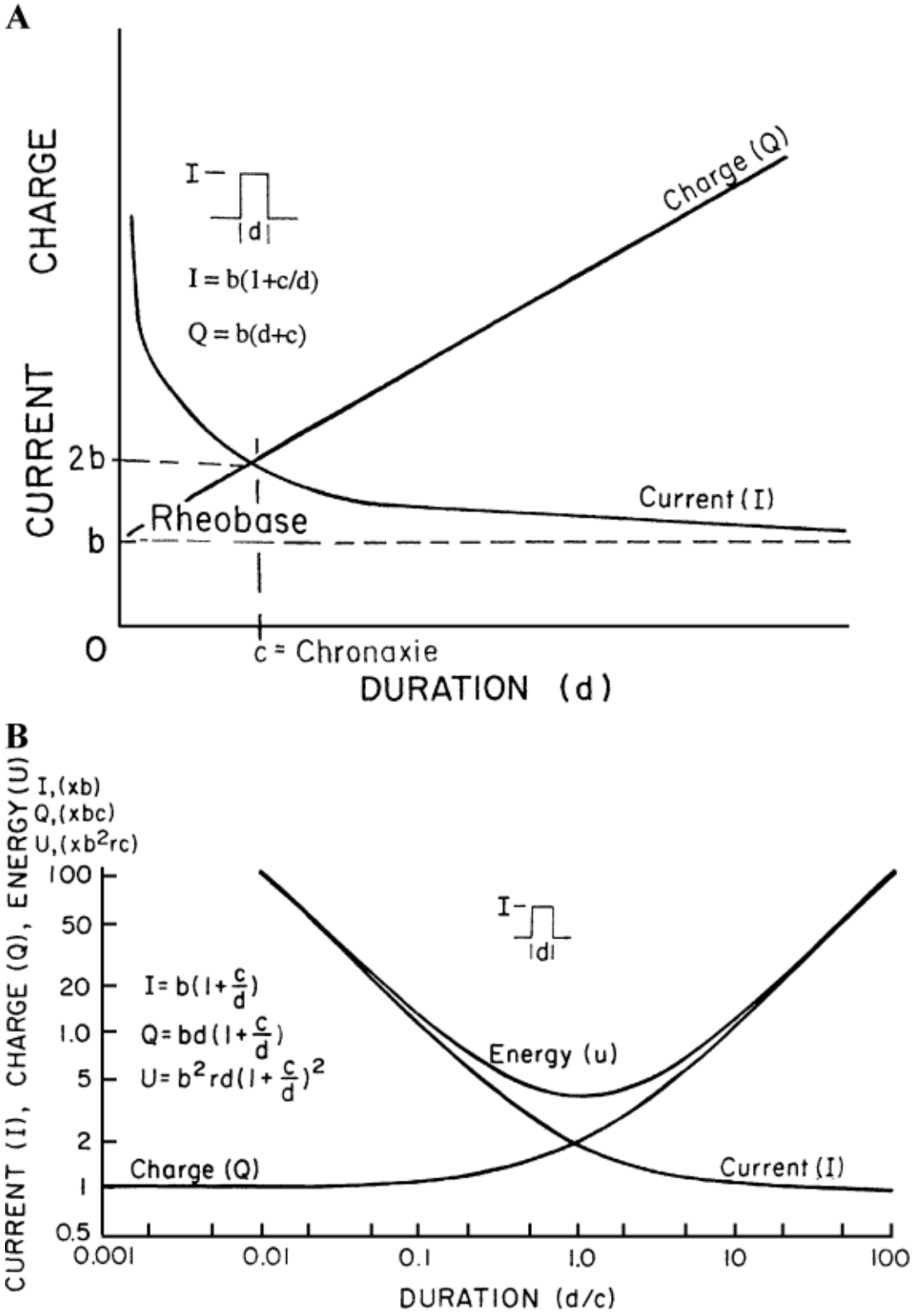

Figure 3.2 Example strength-duration curve
Figure obtained from Geddes et al[102]. A) Lapicque hyperbolic strength-duration (d) curve for current (I) and the Weiss linear strength-duration relationship for charge Q=Id. B) universal strength-duration curves, plotted logarithmically, for current energy and charge, with the duration axis divided by c, the chronaxie.

3.2 Methods

3.2.1 Optical power calibration

A Thorlabs s120vc power meter was used to determine the optical power produced by different voltages on the external Digitimer stimulator. Voltage was then plotted against power and the equation of the best fitting line was used to allow conversion of stimulation voltage into optical power. The area of the field of view of the 40x objective was ascertained using a stage micrometer allowing optical power to be converted into optical power per unit area, the standard unit for use in optogenetics[116,123,139,140]

3.2.2 Cell Plating

Stem cell derived cardiomyocytes (Axiogenesis) were seeded onto fibronectin (1:100 PBS) coated, Mattek 96 well glass bottomed plates at a density of 25,000 cells per well.

3.2.3 Viral Transfection

After 1 day in vitro (DIV) cells were incubated overnight with an adeno-associated virus containing ChR2 (Addgene# 20938M obtained from Vector Biolabs, Pennsylvania) at a multiplicity of infection (MOI) of 1250, 2500, 5000, 10,000, and 20,000

3.2.4 Time course for responsiveness

Each day post transfection, 3 randomly selected regions within each well were excited with 2 Hz 2 ms 470 nm light at an optical power of 1.6 mW/mm^2. The number of responsive regions was recorded until day 5 post-transfection.

3.2.5 Threshold Recordings

Cells were stimulated at 2 Hz with a pulse width of 2 ms using opto-led light at 470 nm the power of which was reduced using a 10% neutral density filter. Cell contractions were recorded using a Hamamatsu orca flash 4.0 camera attached to an Olympus IX71 Microscope at 40x magnification. The minimum optical power required to achieve 1:1 coupling was recorded for each MOI (Figure 3.3).

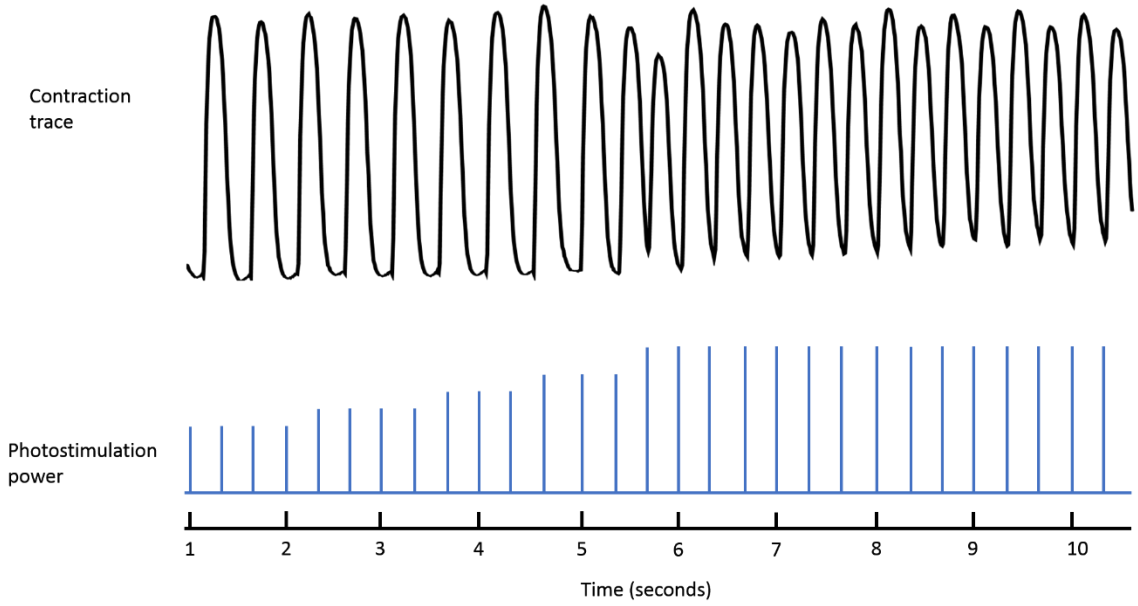

Figure 3.3 Optical thresholding
Demonstration of optical thresholding technique. Contractility (black trace) is monitored while optical power (represented by blue spikes) is gradually increased until 1:1 photostimulation:contraction coupling is achieved.

3.2.6 Chronaxie determination

Responsive cells were excited at 2 Hz with a 480 nm opto-led and the threshold for response measured at 0.2, 0.3, 0.5, 0.7, 1, 2, 3, 5, 7 and 10 ms pulse widths. Control cells were stimulated with solid state electrodes at the same frequency and pulse widths. Strength duration curves were best fitted (R^2 > 99%) with a second order exponential decay function (Figure 3.4). y_0 was used as the rheobasic current and the pulse width corresponding to a threshold current of twice the rheobase was taken as the chronaxie.

Optical chronaxie and rheobase were determined automatically in later chapters using a Python program developed in house to first convert Digitimer stimulator voltage into optical power, and then plot and fit the strength duration curve (see appendix).

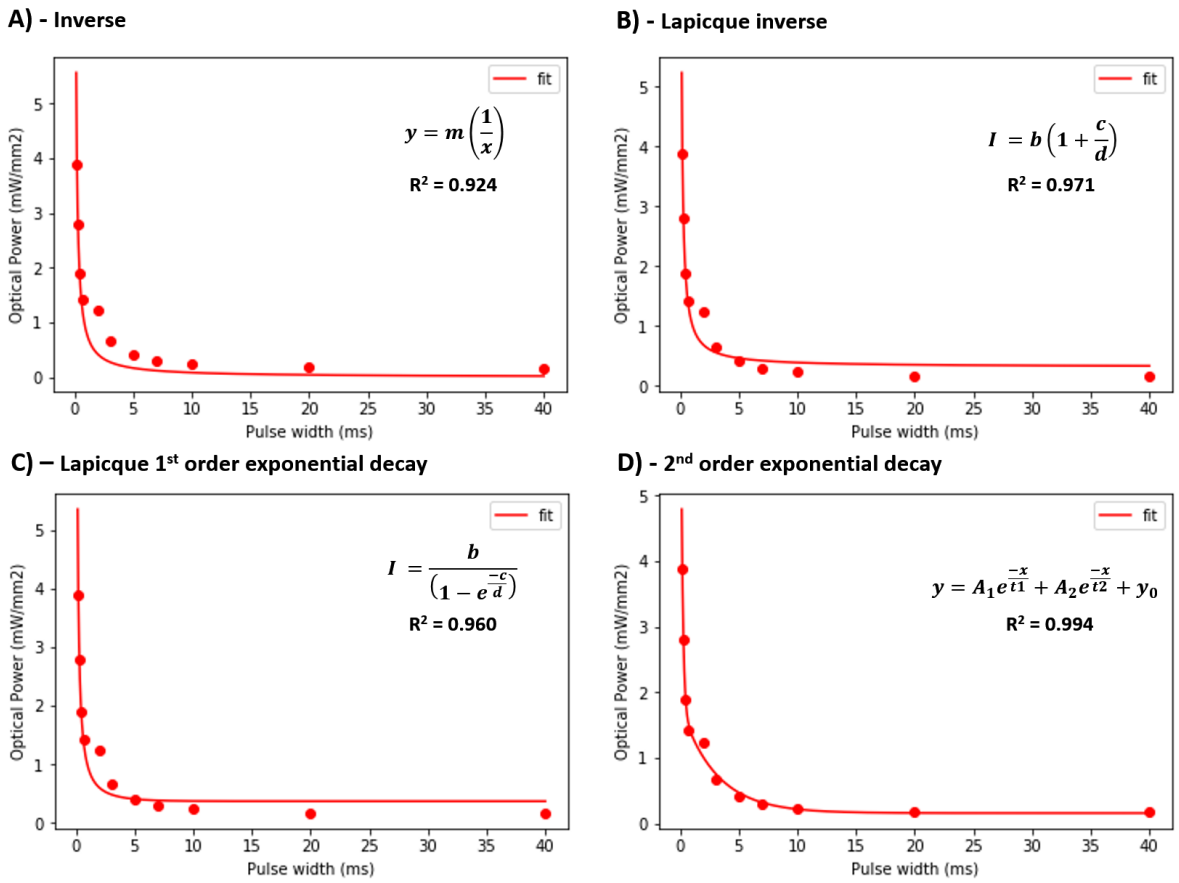

Figure 3.4 Strength duration curve fitting
Optical strength duration curves fit with A) simple inverse function ($I_t = {}^{1}/_{t}$), B) Lapicque hyperbolic function[102] $\left(I = b\left(1 + \frac{c}{d}\right)\right)$ C) Lapicque 1st order exponential decay[141] $\left(I = \frac{b}{\left(1 - e^{\frac{-c}{d}}\right)}\right)$ and D) 2nd order exponential decay $\left(y = A_1 e^{\frac{-x}{t1}} + A_2 e^{\frac{-x}{t2}} + y_0\right)$.

3.2.7 Determining viability of optical dyes

Cell contractility of transfected cells was recorded whilst illuminating constantly with 470 nm (2.11 mW/mm^2), 380 nm (0.45 mW/mm^2), or 340 nm (0.33 mW/mm^2) light at levels used for imaging with optical dyes. Similar recordings were performed every ten minutes over a 30-minute period to determine baseline variations in contractility values under only brightfield illumination.

3.2.8 Statistics

One-way ANOVA or two sample t-tests were used where appropriate. Data are displayed as the mean plus standard error of the mean. $P<0.05$ was taken as significant.

3.3 Results

3.3.1 Voltage and optical power are linearly related

Optical power was linearly related to stimulator voltage with the equation Y= 201.6X – 7.293(Figure 3.5). With a minimum optical power of 1.5μW and a field of view of 0.246 mm^2 the minimum optical power available was 0.006 mW/mm^2

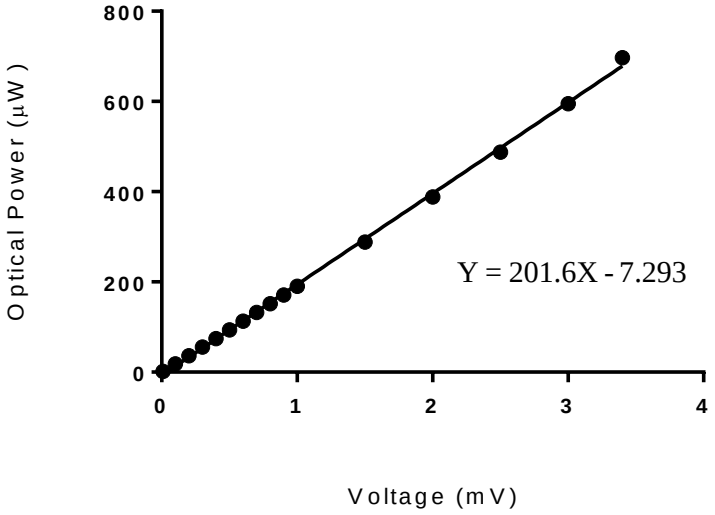

Figure 3.5 Optical power calibration
Optical power through the 40x objective lens is linearly corelated with the voltage supplied through the stimulator box with the equation Y = 201.6X – 7.293.

3.3.2 At 5 days post-transfection cells were fully responsive

Immediately after removal of adeno-associated virus, until 2 days post-transfection, cells showed no response to optical stimulation regardless of the MOI used. At 2 days post-transfection several areas within wells transfected at an MOI of 2500 and above responded to stimulation, however there were still unresponsive areas within these wells. By day 3 all conditions had responsive areas with cells transfected at MOI's of 10000 and 20000 showing 100% responsiveness to stimulation. The percentage of areas responding to stimulation continued to increase with cells transfected at an MOI of 5000 reaching 100% responsiveness at 3 days post-transfection and those transfected at an MOI of 2500 reaching 100% responsiveness at 4 days post-transfection. Cells transfected at an MOI of 1250 did not reach 100% responsiveness by the time the experiment was concluded (Figure 3.6A). The threshold value of the responsive areas at day 5 did not differ significantly between the transfection groups (Figure 3.6B, unpaired 1-way anova).

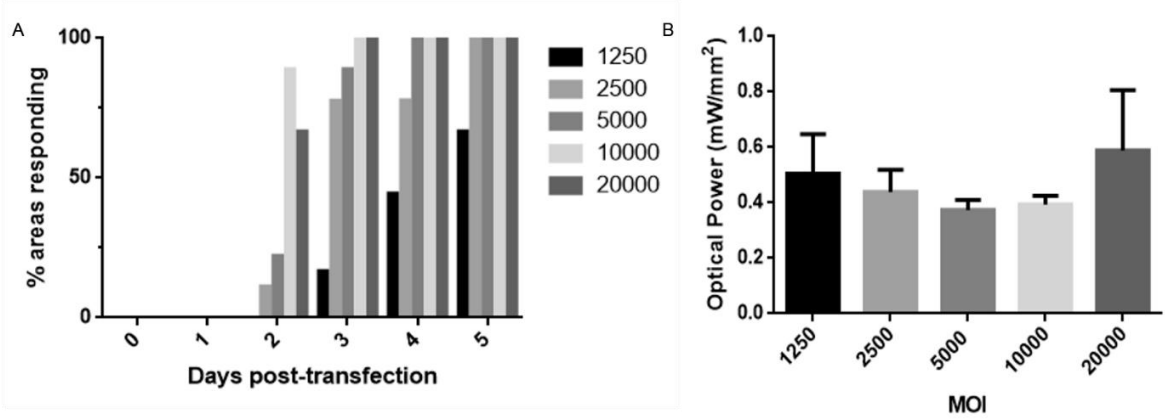

Figure 3.6 Cell responsiveness over time
A) cells began responding to stimulus at 2 days post-transfection and the percentage of areas responding increased to 100% at, 3 days post transfection in cells transfected at MOI's of 10000 and 20000, 4 days post-transfection for cells transfected at MOI 5000 and 5 days post-transfection at 2500 MOI. B) At 5 days post-transfection there was no significant differences in threshold within responsive areas between transfection groups.

3.3.3 Optical and electrical excitability is comparable.

The chronaxie for optical stimulation (1.53 ± 0.32 ms N=9) was not significantly different from the chronaxie of traditional electrical stimulation (2.17 ± 0.44 ms N=9, P=0.2434 unpaired t-test) (Figure 3.7D).

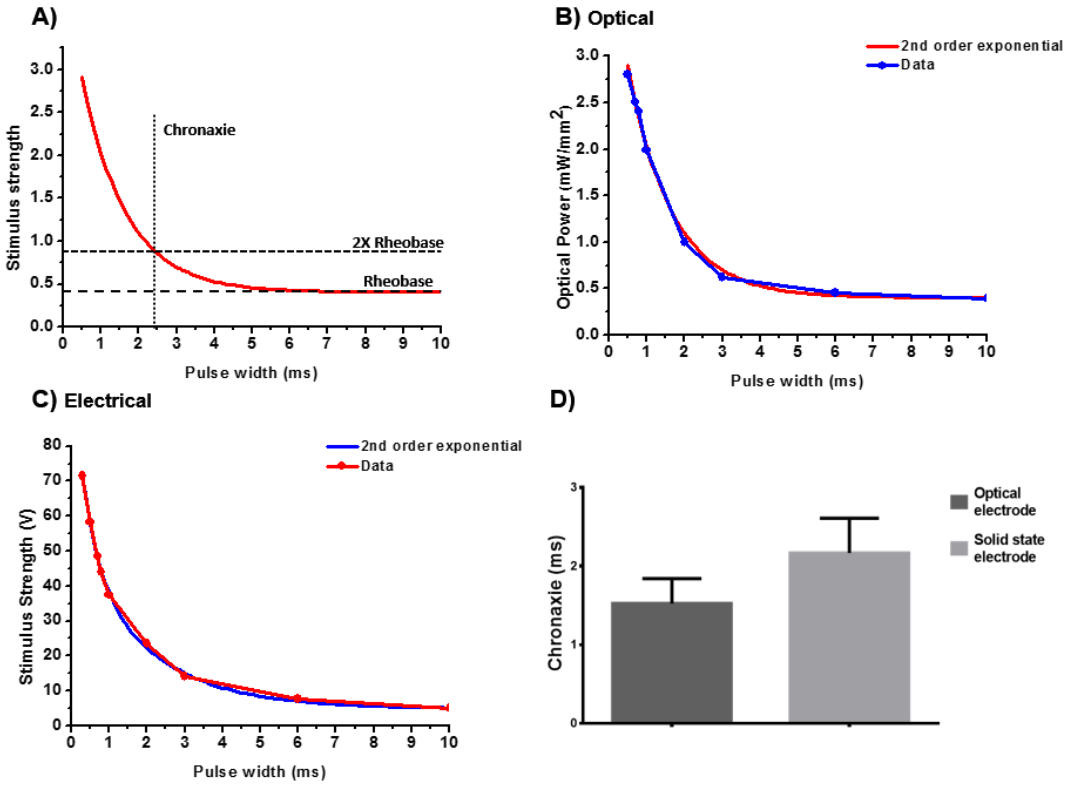

Figure 3.7 Photostimulation validation
A) Example of strength-duration curve showing rheobase, 2x rheobase and chronaxie time. B) Example of strength-duration curve obtained using optical stimulation at 2 Hz with an MOI of 2500. C) Example of strength-duration curve obtained using electric field stimulation. D) No significant difference in chronaxie between optical and field stimulation (N = 9 wells).

3.3.4 Continuous illumination with 470 nm light drastically alters cell contractility

Continuous 470 nm illumination caused a significant decrease in contraction amplitude (Table 3.1, Figure 3.8). Cycle length, Up90, and Dn90 were not significantly changed by 470, 380, and 340 illumination. The spread (max value-min value) of data was much larger upon 470 illumination compared to the spread caused by time (Table 3.1, Figure 3.10). The spread of data under 380 and 340 nm illumination was less than the spread under 470 nm illumination, however it was still larger than the spread of data after 30 minutes (Table 3.1,Figure 3.10).

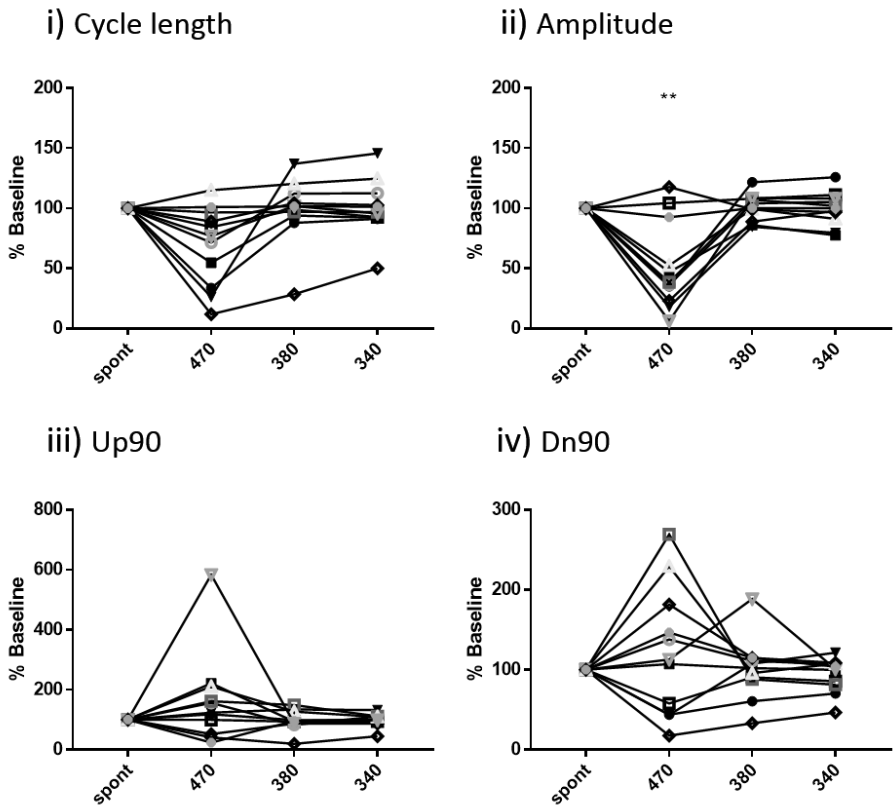

Figure 3.8 Change in cell function during continuous illumination
Demonstration of the spread of values recorded in i) spontaneous cycle length, ii) contraction amplitude, iii) Up90 and iv) Dn90 that occurred upon illumination with 470, 380, and 340 nm light. 470 nm light caused a significant decrease in contraction amplitude (404.1 ± 40.1 vs 195.0 ± 37.5, P = 0.0076) and increased the spread of data in all parameters recorded N = 11 cell areas.

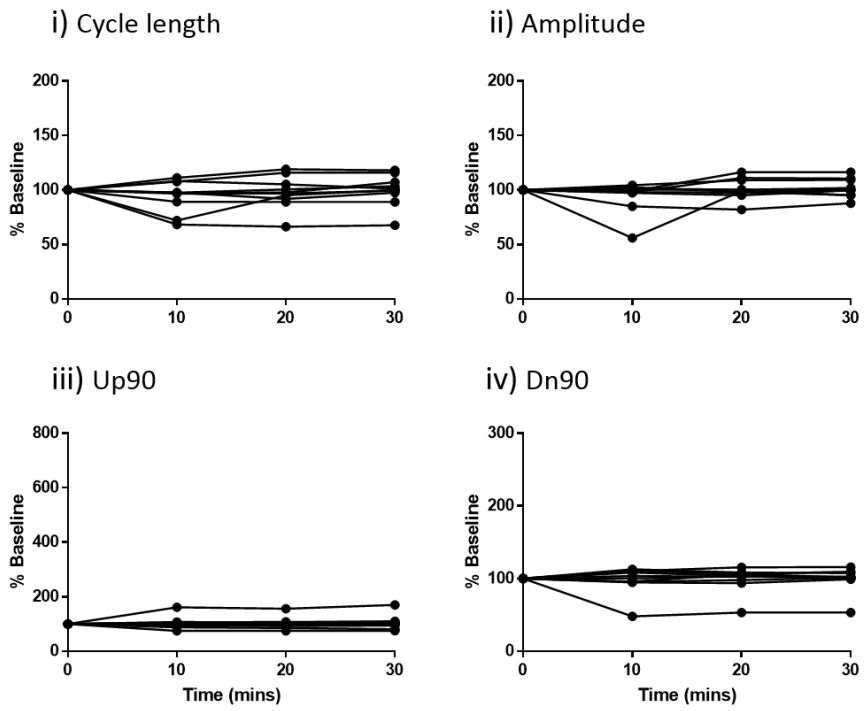

Figure 3.9 Change in cell function over 30 minutes
Demonstration of the spread of values recorded in i) spontaneous cycle length, ii) contraction amplitude, iii) Up90 and iv) Dn90 that occurred over 30 minutes. N = 10 cell areas

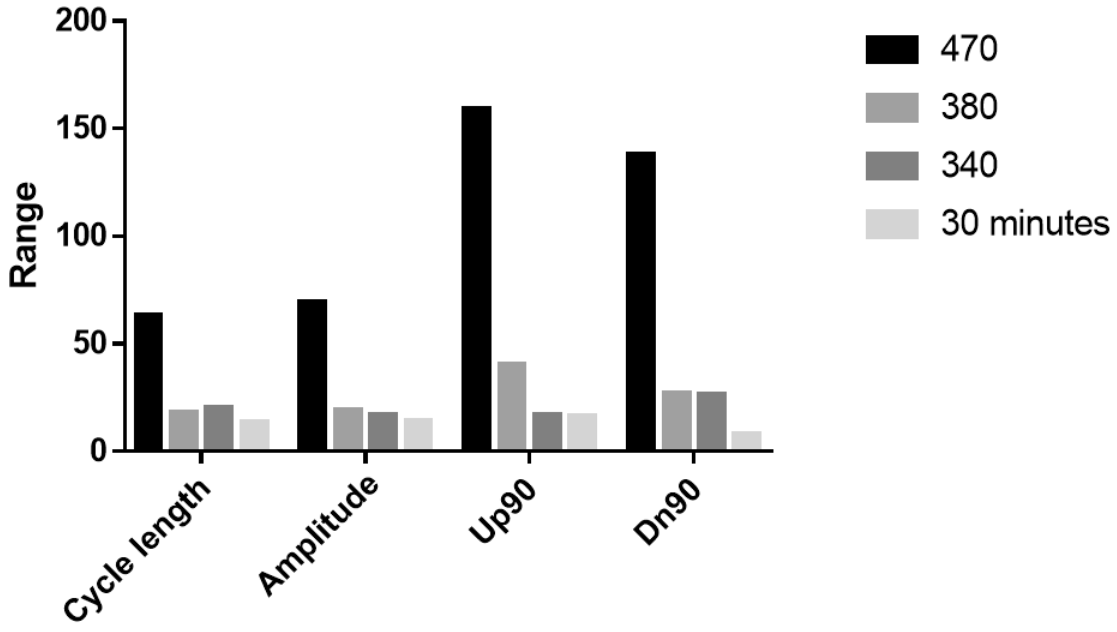

Figure 3.10 Change in cell function during continuous illumination
Demonstration of the spread of values recorded in i) spontaneous cycle length, ii) contraction amplitude, iii) Up90 and iv) Dn90 that occurred upon illumination with 470, 380, and 340 nm light (Figure 1.8) compared to the variation over time (Figure 1.9). 470 nm light had a significant effect on average contraction amplitude but increased the spread of data in all parameters recorded. The range of values observed is displayed in section C).

Table 3.1 Change in cell function during continuous illumination
Spread of contractility parameters represented by the range of values shown in Figure 3.10

	470 nm	380 nm	340 nm	30 minutes
Cycle length	62.97	18.14	20.36	13.47
Amplitude	69.48	19.14	17.07	14.24
Up90	158.72	40.02	17.02	16.35
Dn90	137.70	26.69	26.17	8.00

3.4 Discussion

3.4.1 At 5 days post-transfection cells were fully responsive

Time course and threshold results reveal that, as MOI does not affect stimulation threshold, the optimal transfection protocol was an MOI of 2,500 allowing photostimulation at 5 days post-transfection. Although a higher MOI would allow 100% responsiveness to be reached sooner, a lower MOI was chosen to prevent waste. This protocol was used for all following photostimulation experiments.

3.4.2 Optical and electrical excitability is comparable.

The chronaxie for ChR-2 stimulation has previously been shown to be approximately 4 ms in isolated rat cardiomyocytes[142], and 5-7 ms for intact mouse hearts[140]. The chronaxie for cathodal stimulation of intact rat hearts has been shown to be 0.8-0.9 ms[143], 0.2-0.5 ms for field stimulation in neonatal rat heart constructs[144], and 1.8 ms for field stimulation in isolated adult rat cardiomyocytes[145]. Modelling of optogenetic and electrical stimulation in human cardiomyocytes shows a preservation of action potential morphology between ChR-2 stimulation and direct electrical current injection, although differences in current waveform meant that the corrected chronaxie for optical stimulation was 18 ms compared to 8 ms for electrical stimulation[146].

Taken together these results indicate that muscular systems are less sensitive to optogenetic stimulation than they are to electrical stimulation. However, to the authors knowledge, no other study has performed a direct comparison between field stimulation and ChR-2 stimulation within the same cells. Within this chapter, chronaxie values did not differ significantly between electrical and

optogenetic stimulation, indicating that iPSC-CMs are equally excitable by ChR-2 and field stimulation.

3.4.3 Continuous illumination with 470 nm light drastically alters cell contractility

For an optimal signal-to-noise ratio, voltage measurements using di-4-anneps or fluovolt use 470 nm illumination at an intensity of 2.11 mW/mm^2, far above the threshold intensity for optical pacing (Figure 3.6b). As 470 nm illumination is close to the peak excitation of ChR-2[127], continuous supra-threshold illumination led to a significantly reduced contraction amplitude and disrupted other contraction parameters (Figure 3.8) above the normal variation in these cells (Figure 3.9). A consequence of this is that the optical voltage sensors used in house are incompatible with ChR-2 based optogenetic pacing. Recent work has shown that the red shifted voltage sensor di-4- ANBDQPQ allows voltage measurements alongside optical pacing with ChR-2 in mouse hearts[147]. Unfortunately, adapting the optical platform used in this project to allow use of red shifted dyes was out with the scope of this project due to time and cost restraints.

Although there were no significant changes in cell contractility, there was also minor disruption of contraction upon 380 nm illumination. As shown previously (Figure 2.6), the action spectra for ChR-2 shows current injection at wavelengths as low as 390 nm. It is therefore likely that illumination with 380 nm causes a current injection that is below the threshold for action potential generation, but large enough to disrupt action potential, and subsequently contraction morphology. In future studies the use of red shifted voltage sensitive dyes could be used to test this hypothesis.

3.4.4 Conclusions

Photostimulation is a valid alternative to solid state electrical stimulation however it is incompatible with standard fluorescent voltage or Ca^{2+} indicators.

Chapter 4: Initial trial of chronic pacing

4.1 Introduction

Chapter 3 demonstrated that the introduction of channelrhodopsin-2 into Axiogenesis iPSC-CMs allows the endogenous rate of the cells to be overridden by photostimulation. This chapter shall attempt to determine whether this alteration of contraction frequency can be used to induce a phenotypic change.

Controlling the beating rate of iPSC-CMs via electrical stimulation has been shown to induce phenotypic changes associated with an increase in maturity[48-50]. Continuously overriding the endogenous rhythm of iPSC-CMs for a period of several days has also been shown to have lasting effects on iPSC-CM electrophysiology[51,148]. An interesting aspect of electrical stimulation is the electrolysis of extracellular solutions leading to generation of reactive oxygen species (ROS)[149,150]. Given that it has been shown that application of ROS can itself induce phenotypic changes in embryoid bodies[47], it is possible that the phenotypic changes observed following electrical stimulation could be due to ROS. There is little evidence suggesting that optogenetic stimulation via channelrhodopsin-2 results in the generation of ROS.

The long-term goal of this project was to replicate the electrical conditions found in the early stages of cardiac development. This entails replicating a directional action potential spread for a period of several days. Before the directionality can be replicated it must be demonstrated that photostimulation can be maintained for the appropriate length of time.

4.1.1 Aims

This chapter aimed to:

1) Determine whether photostimulation can be maintained for an extended period.

2) Identify phenotypic changes occurring as a result of extended photostimulation.

3) Identify any issues that may hinder application of the photostimulation protocol.

4.2 Methods

4.2.1 Cell plating

Cells were plated in Mattek, glass bottomed 35 mm petri dishes at a density of 25,000 per well as described previously.

4.2.2 Viral transfection

Cells were transfected at an MOI of 2,500 and were ready for use 1 week after plating as described in chapter 3.

4.2.3 48-hour pacing

Petri dishes containing transfected cells were moved to an Okolab stage incubator mounted upon an Olympus IX71 microscope. A central location of beating cells was located using 40x magnification. This central area was then stimulated at 2 Hz with a pulse width of 2 ms for a period of 48 hours using a 470 nm led at 10% above pacing threshold power. Contractility recordings and strength-duration curves were taken at the beginning and end of the 48-hour period.

4.2.4 48-hour multi-site pacing

To reduce the total amount of photostimulation delivered to a single site, In-house software was used to move photostimulation between 6 peripheral sites per well by moving the stage to predetermined sites. Sites were photostimulated at 2-3 Hz with a 2 ms pulse width for 100 seconds. Photostimulation was alternated between 2 adjacent inserts to allow concomitant photostimulation with a duty cycle of 50% (Figure 4.1). Contractility recordings and strength duration curves were taken before and after pacing. Cells were then fixed using 2% paraformaldehyde (PFA).

4.2.5 96-hour multi-site pacing

Using the same protocol as before, cells were paced for 96 hours and cell media was replaced every 48 hours. At the end of the 96 hours, photostimulation was stopped and the cells were rested for 24 hours. Contractility recordings and

strength duration curves were taken at 0,48 and 96 hours of pacing. To identify any lasting effect of photostimulation, recordings were also taken after the 24-hour rest period. The cells were once again fixed at the end of the experiment.

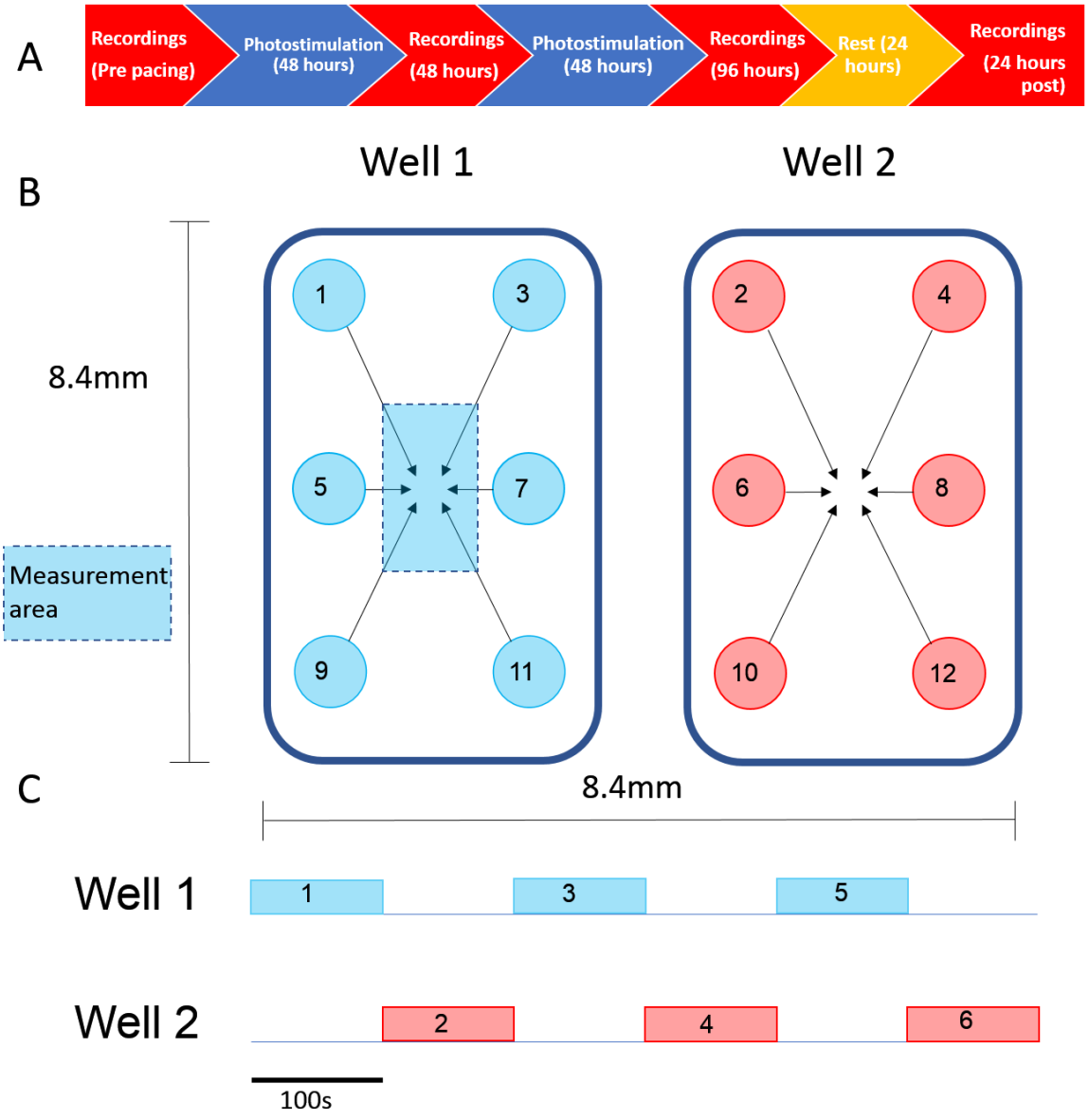

D

	Stimulation cycles per site	Stimulation time per site per cycle (seconds)	Total stimulation time per site (hours)	Rest time per site per cycle (seconds)	Total rest time per site (hours)
48 hours	144	100	4	1100	44
96 hours	288	100	8	1100	88

Figure 4.1 Multi-site pacing protocol
A) Timeline for 96-hour pacing. B) Figure representing order and position of photostimulation sites across 2 wells within a 35 mm glass bottomed petri dish. C) Mock timeline demonstrating the 50% duty cycle with each block representing 100 seconds of photostimulation. D) Total pacing and rest times for each stimulation site over 48 and 96 hours.

4.2.6 Study endpoints

To identify any issues with the chronic pacing protocol, several parameters were studied before and after pacing. The spontaneous cycle length and contraction kinetics such as the Up90, Dn90, CD10, 50 and 90 served as markers of cell function and were obtained within 30 seconds of the cessation of photostimulation. Details of contractility parameters can be found in chapter 2. Sarcomere length, inhomogeneity and alignment served as markers of cell structure, details of their acquisition can be found in chapter 2.

4.3 Results

4.3.1 Chronic pacing at a single site causes cell death

Chronic pacing at an individual sight caused cell damage within 24 hours and loss of coupling and cell death within the photostimulation area within 48 hours. Further pacing experiments utilised a patterned photostimulation protocol. Initial experiments demonstrated that a 100% duty cycle still proved toxic, however a 50% duty cycle was well tolerated over 96 hours by trial cells. The toxic effect of photostimulation is studied in detail in chapter 5.

4.3.2 48 hours of patterned photostimulation caused changes in spontaneous rate

There were no changes in the chronaxie times or rheobasic currents obtained from the strength duration curves (Figure 4.2) taken before and after 48 hours of 2 Hz pacing, indicating that cell excitability was not altered significantly. 2 Hz pacing also had no effect on the contraction upstroke or downstroke (Figure 4.2). The spontaneous cycle length (Figure 4.4) and sarcomere length, inhomogeneity and dispersion (Figure 4.3) were also unchanged by chronic pacing at 2 Hz.

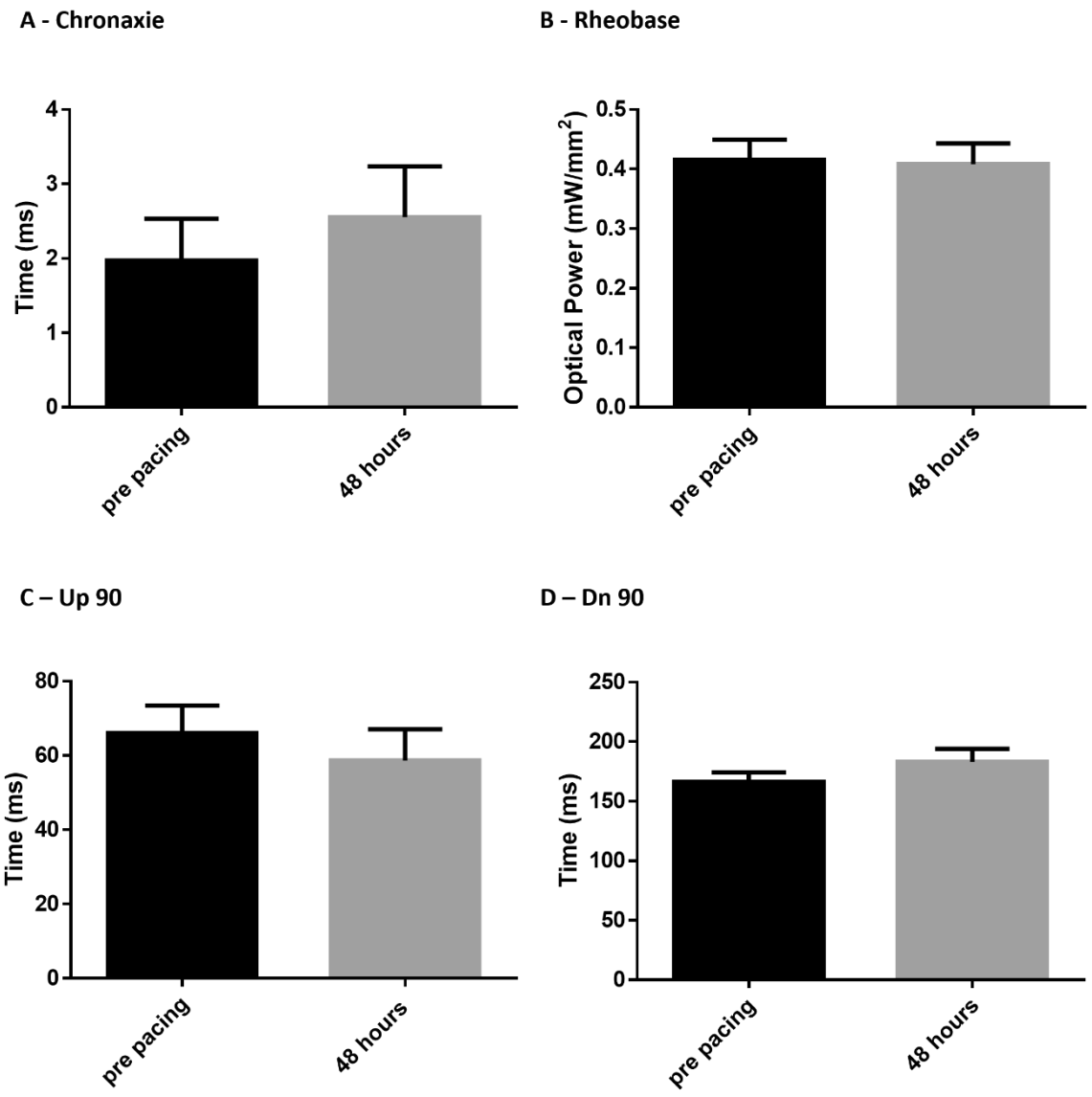

Figure 4.2 Cell functionality after photostimulation period (48 hours)
Functional measurements acquired before and after 48 hours of 2 Hz photostimulation. There was no change in the chronaxie after 48 hours of photostimulation, the rheobasic optical power remained unchanged by pacing. Up90 and the dn90 were not influenced by the photostimulation protocol (N = 6 wells).

Initial experiments increasing the photostimulation frequency to 3 Hz had no effect on contraction kinetics, but significantly increased the spontaneous cycle length (Figure 4.4). 3 Hz photostimulation for 48 hours caused the spontaneous cycle length to increase from 576 ± 79 ms to 2258 ± 608 ms (P= 0.021 unpaired t-test).

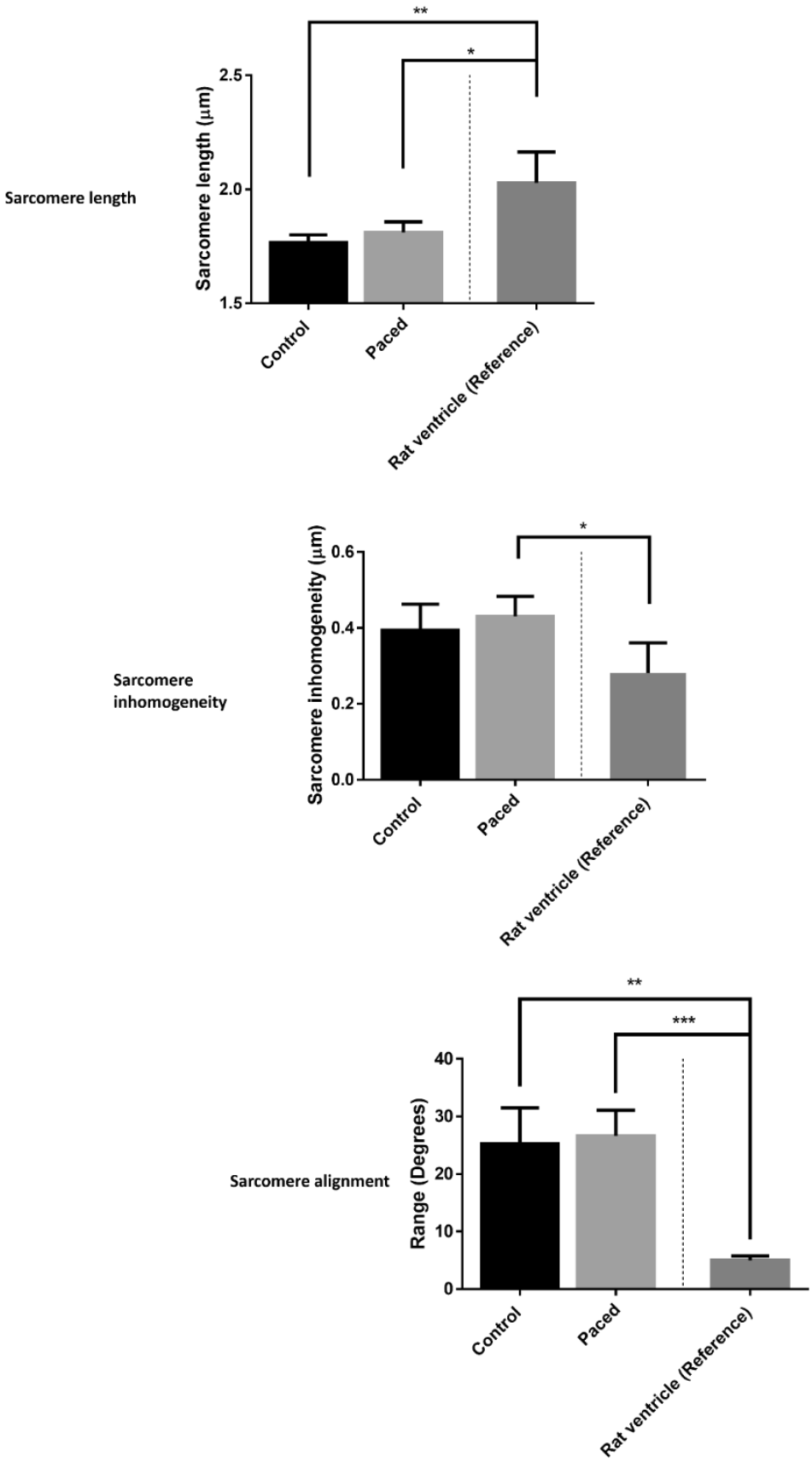

Figure 4.3 Cell structure after photostimulation period (48 hours)
Sarcomeric measurements comparing control, paced (N = 4 wells, 10 cells/well) and adult (rat ventricle, N= 3 animals, 10 cells/animal) cells. There were no changes associated with pacing in sarcomere length, sarcomere inhomogeneity or sarcomere alignment. The iPSC-CM's remained significantly different to adult myocytes in all 3 metrics. * P≤0.05, ** P≤0.01, *** P≤0.001 (1-way ANOVA)

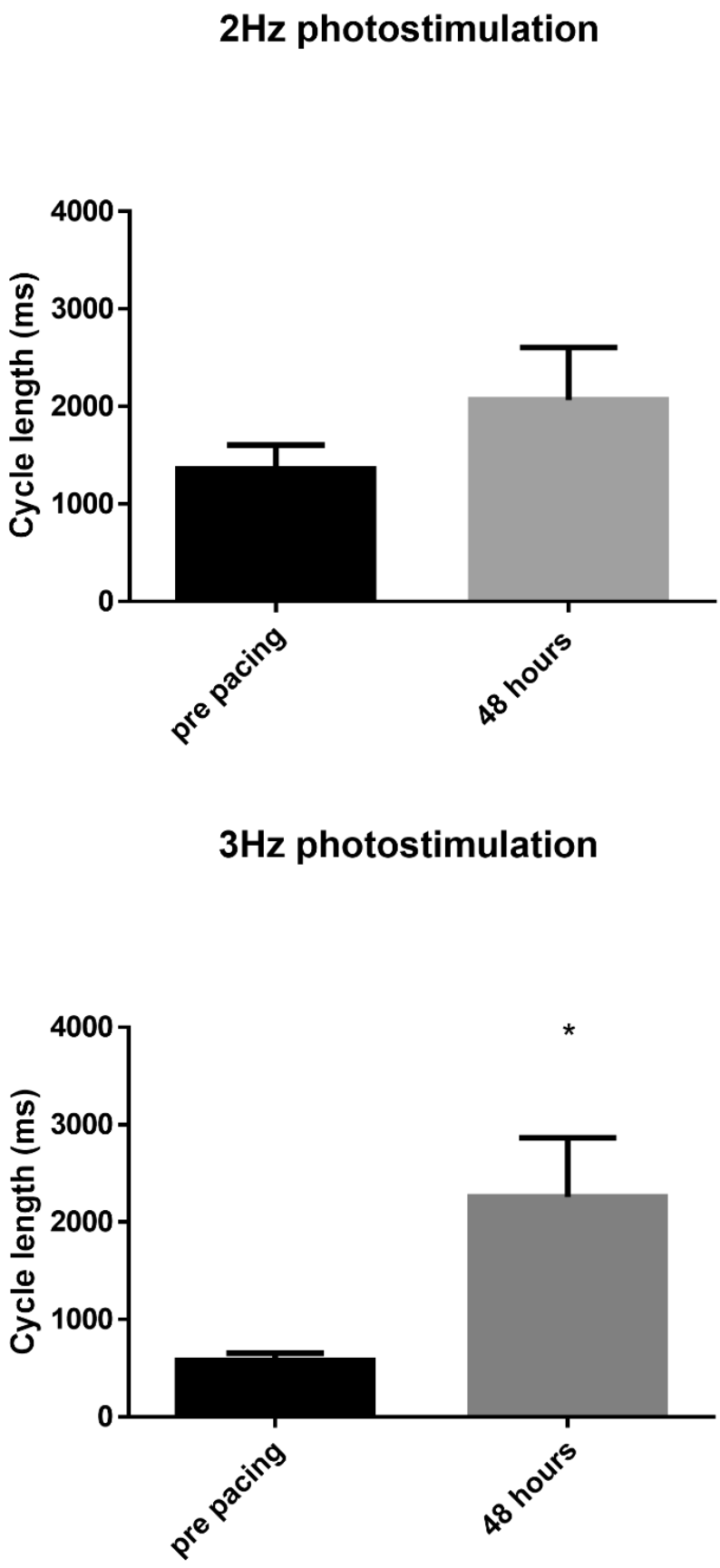

Figure 4.4 Spontaneous cycle length after photostimulation period (48 hours)
Measurements of spontaneous activity of iPSC-CM's. The cycle length of spontaneous contractions remains unchanged following 48 hours of 2 Hz photostimulation, however 48 hours of 3 Hz photostimulation caused a significant increase in the spontaneous cycle length (N = 6 wells).
* P≤0.05 (paired t-test)

4.3.3 96 Hours of patterned photostimulation at 3 Hz caused changes in cell function and structure.

There were no changes in markers of cell excitability both during and following the photostimulation protocol (Figure 4.5). The spontaneous cycle length was significantly increased after 48 (868.8 ± 143.2 ms to 5709 ± 1293 ms P=0.0245 repeated measures one-way ANOVA) and 96 hours of pacing (1931 ± 190.8 ms P=0.0062 repeated measures one-way ANOVA) but returned to prepacing values after the 24-hour rest period (Figure 4.6).

Measurements of contraction kinetics were complicated by an artefact generated by the stimulus light masking the contractility trace making analysis of paced traces impossible. Therefore, the recordings of spontaneous activity in the paced areas were analysed. There were no significant changes in the Up90 over the course of the experiment however Dn90 varied over the course of the experiment and was significantly increased at 24 hours post pacing (167.9± 16.5 ms vs 424.7± 60.1 ms P = 0.0162 repeated measures ANOVA). CD90, CD50 and CD10 were unchanged throughout the pacing protocol (Figure 4.7). Unpaced, stage incubator cells showed no change in Up90 or CD50 (Figure 4.8 A and D). Dn90 was significantly increased at 96 hours (462.3 ± 35.1 ms, P=0.0199) and 24 hours post pacing (330.6 ± 36.9 ms P=0.0168) compared to prepacing values (215 ± 45.73 ms) (Figure 4.8 B). Similar increases were seen in CD90 (0 hours, 99.4 ± 11.0 ms. 96 hours, 153.9 ± 6.6 ms P=0.008. 24 hours post, 142.7 ± 12.3 ms P=0.0235 repeated measures ANOVA) (Figure 4.8 C) and CD10 (0 hours, 378.3 ± 45.3 ms. 96 hours, 669.3 ± 37.92 ms P=0.0087. 24 hours post, 532.2 ± 46.31 ms P=0.002 repeated measures ANOVA) (Figure 4.8 E). Unpaced, full incubator cells showed no significant changes in Up90, CD90, CD50 or CD10 over the protocol period (Figure 4.9 A, C, D, and E respectively). These cells did however display a significant increase in Dn90 at 24 hours post pacing compared to prepacing values (333.9 ± 26.8 ms vs 165.1 ± 19.9 ms, P=0.0424 repeated measures ANOVA) (Figure 4.9 B).

Chronic photostimulation caused significant shortening of the sarcomeres when compared to unstimulated controls (1.71 ± 0.009m to 1.67 ± 0.012 μm P=0.0193 unpaired t-test) but had no effect on the sarcomere inhomogeneity or alignment (Figure 4.11).

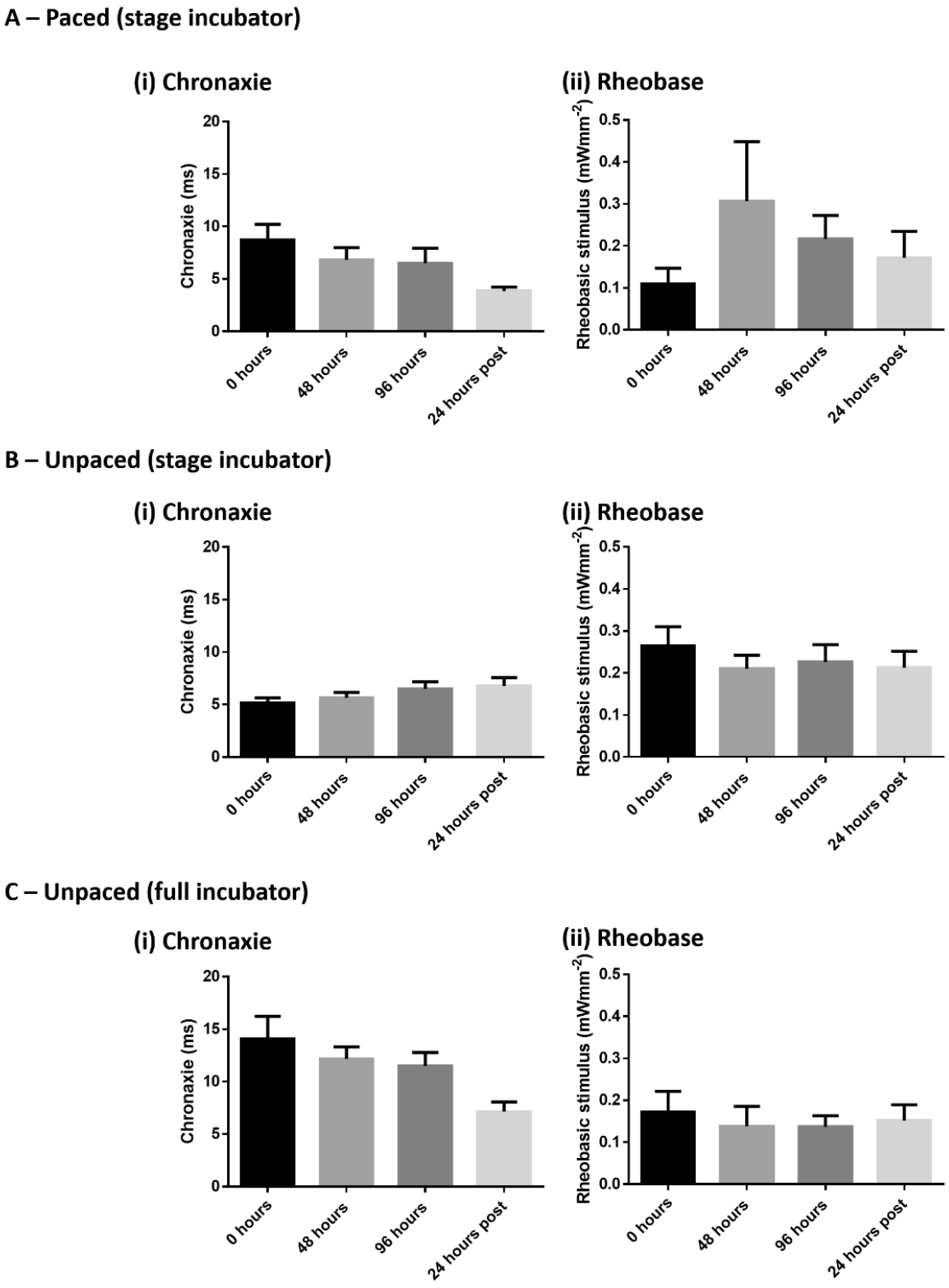

Figure 4.5 Cell excitability throughout photostimulation period (96 hours)
Chronaxie times (i) remained unchanged in paced cells (A) unpaced cells stage incubator cells (B) and unpaced full incubator cells (C). Rheobasic power (ii) also remained unchanged in paced cells(A) unpaced cells stage incubator cells (B) and unpaced full incubator cells (C) (N = 6 wells).

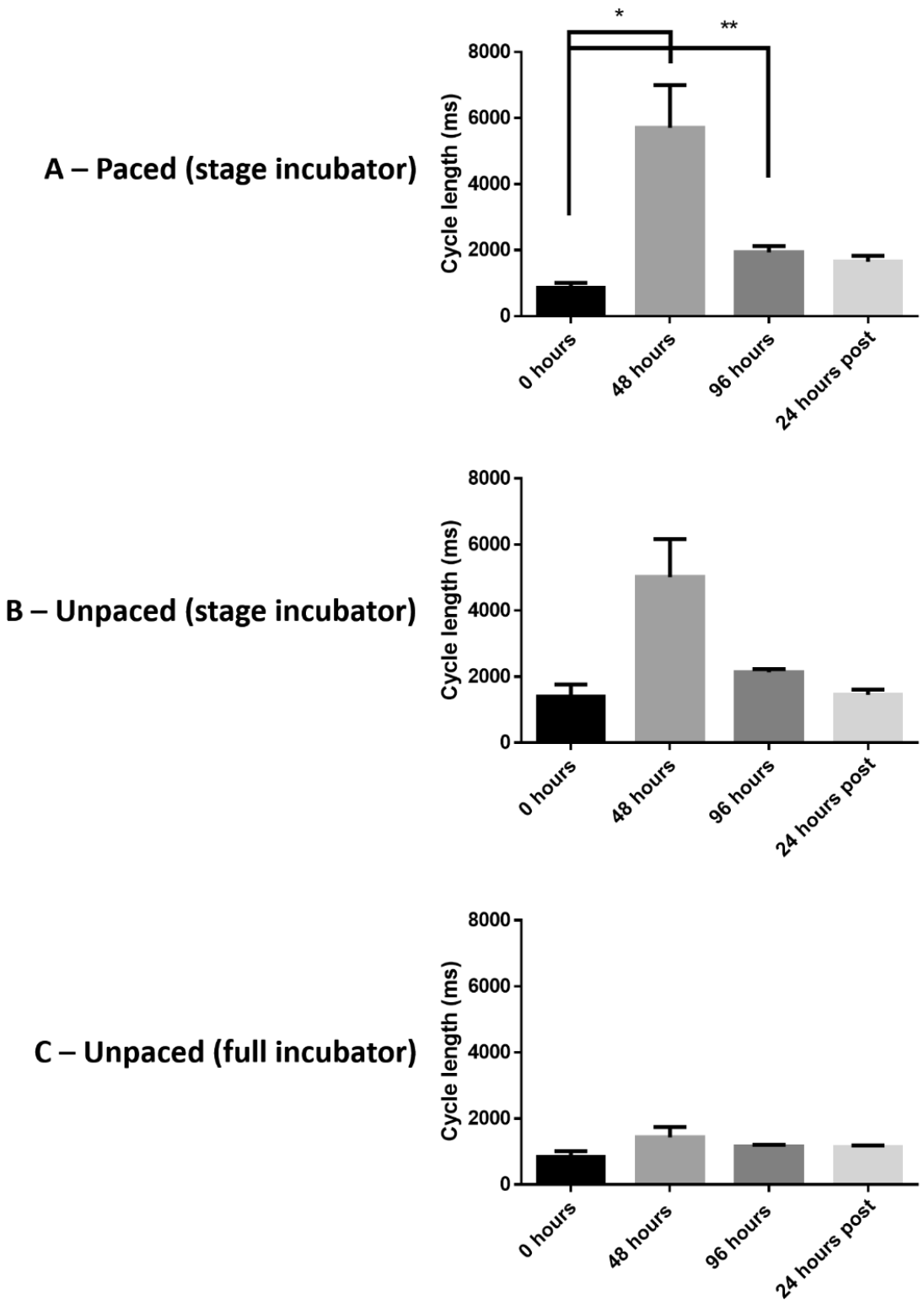

Figure 4.6 Spontaneous cycle length over 96 hours
Spontaneous cycle length of paced cells was increased at 48 and 96 hours before returning to prepaced values after 24 hours of rest. Unpaced cells in both stage and full incubators remained unchanged throughout the photostimulation period and following 24 hours of rest (N = 6 wells). * P≤0.05, ** P≤0.01 (repeated measures ANOVA)

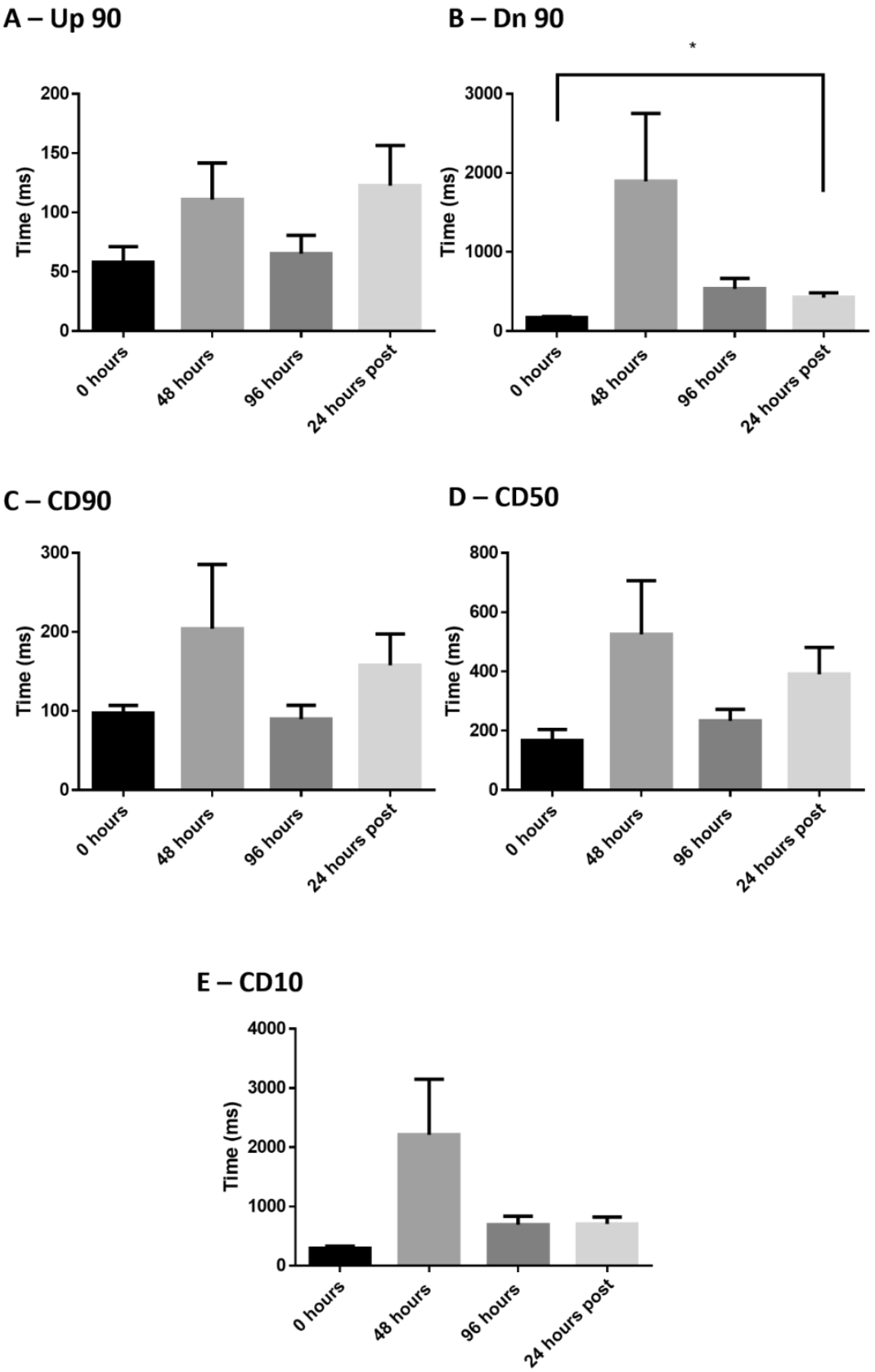

Figure 4.7 Contraction kinetics of paced cells (96 hours)
Contractility measurements from spontaneous cells. Up90 (A), CD90 (C), CD50 (D) and CD10 (E) remained unchanged throughout the photostimulation protocol. Dn90 (B) was significantly increased at 24 hours post stimulation (N = 6 wells). * P≤0.05 (repeated measures ANOVA).

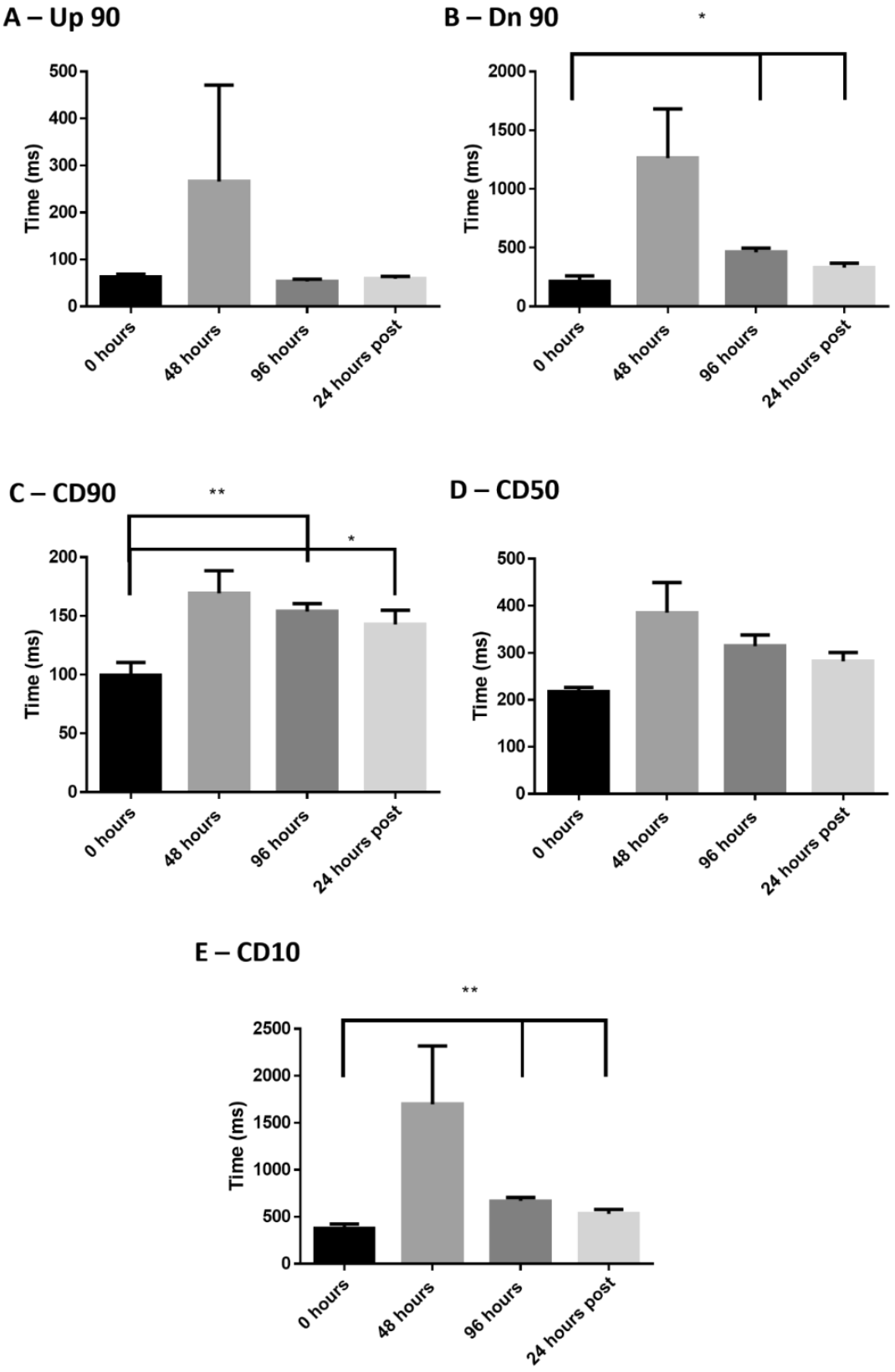

Figure 4.8 Contraction kinetics of unpaced cells (stage incubator)
Contractility measurements from spontaneous cells. Up90 (A) and CD50 (D) showed no significant changes. Dn90 (B), CD90 (C) and CD10 (E) showed significant increases at after 96 hours of pacing, and after 24 hours of rest (N = 6 wells). * P≤0.05, ** P≤0.01 (repeated measures ANOVA).

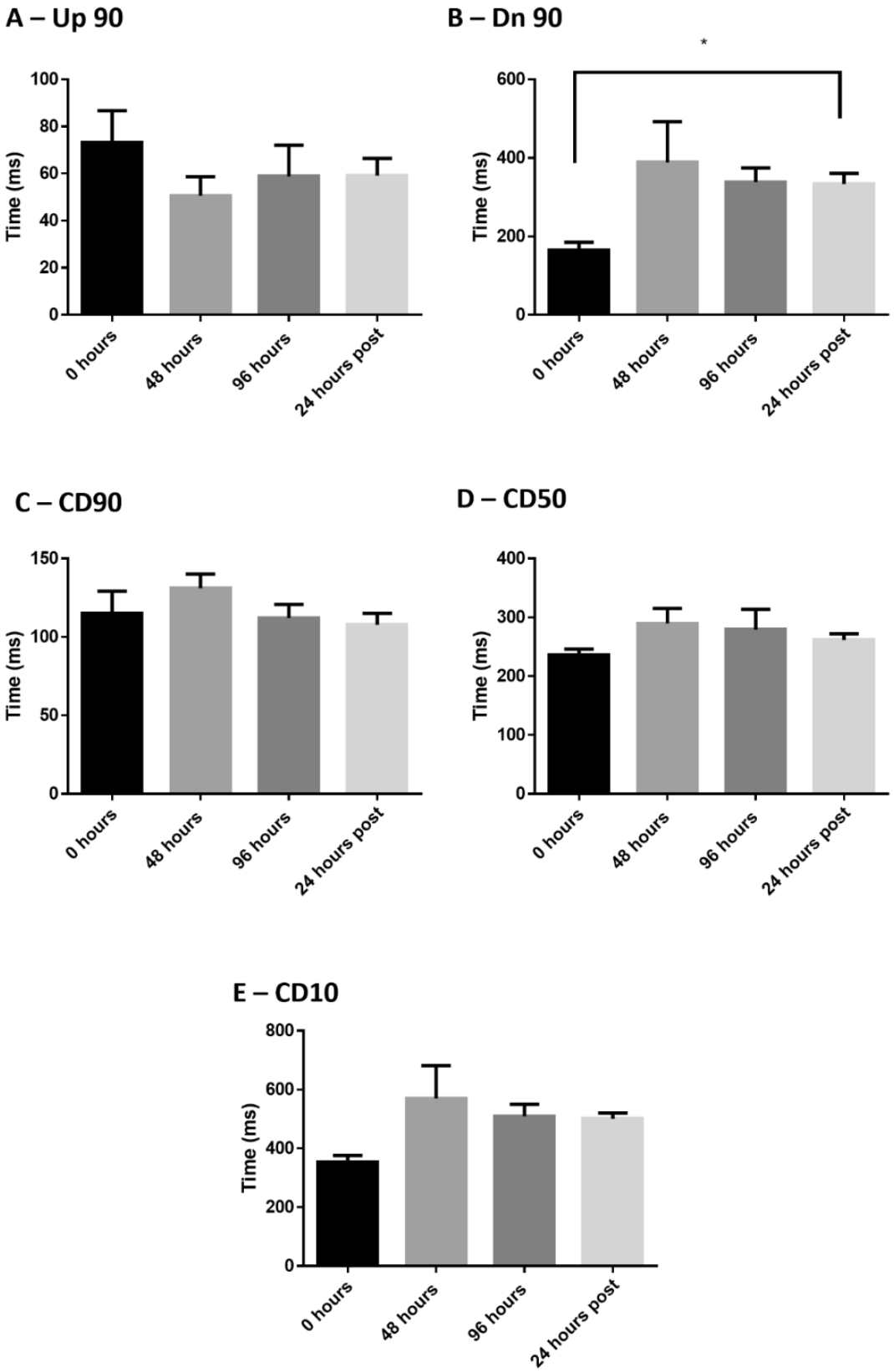

Figure 4.9 Contraction kinetics of unpaced cells (full incubator)
Contractility measurements from spontaneous cells. Up90 (A), CD90 (C), CD50 (D) and CD10 (E) remained were not significantly different at the protocol endpoint. Dn90 (B) was significantly increased after the 24-hour rest period (N = 6 wells). * P≤0.05 (repeated measures ANOVA)

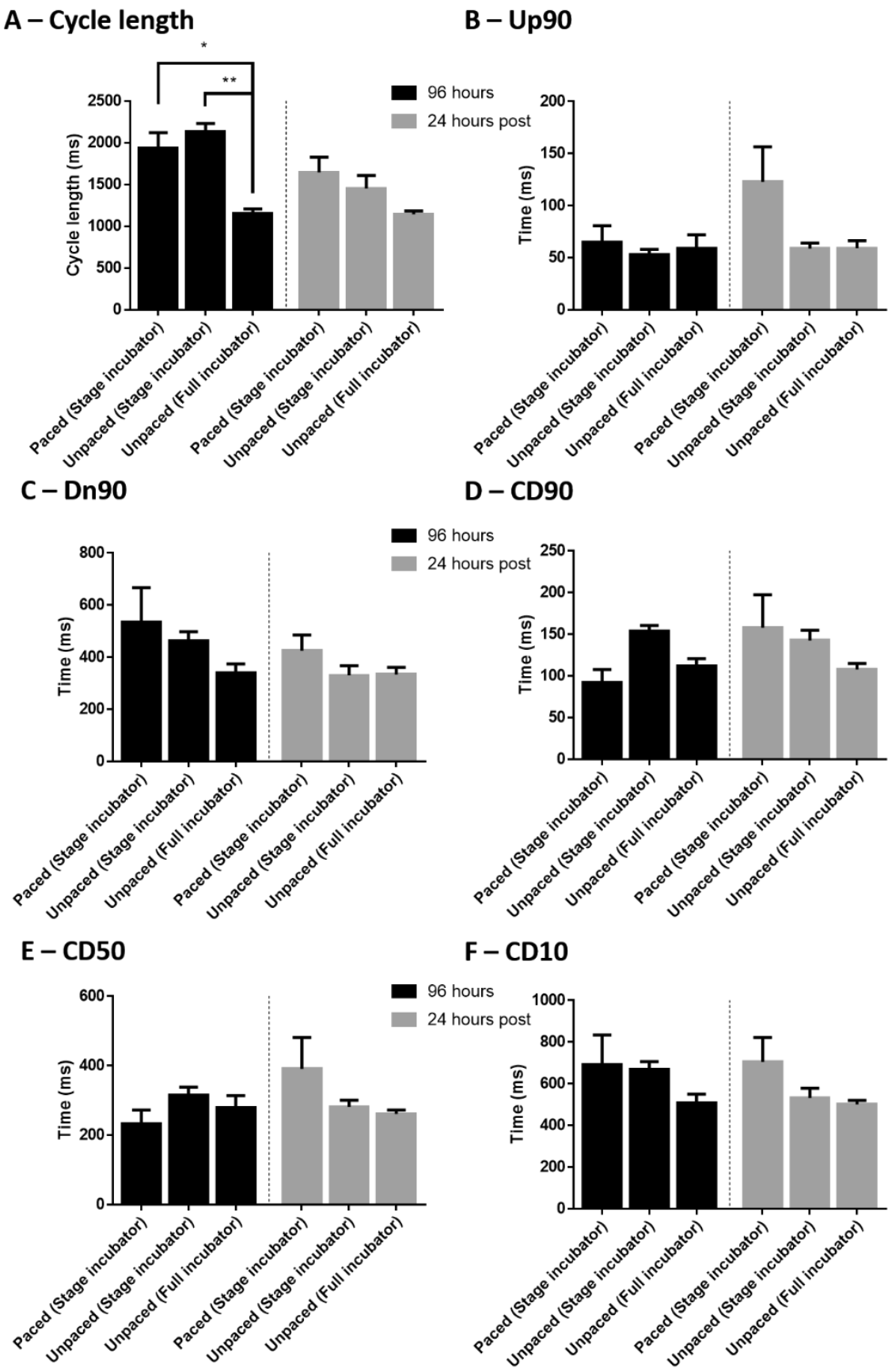

Figure 4.10 End point contraction kinetics across all conditions
Contraction kinetics at 96 hours (black) and 24 hours post pacing (grey) were compared across the 3 experimental conditions, Paced and unpaced stage incubator cells showed a significantly different spontaneous cycle length from unpaced, full incubator cells at 96 hours (A). Up90 (B), Dn90 (C), CD90 (D), CD50 (E) and CD10 (F) were not significantly different (N= 6 wells). * P≤0.05, ** P≤0.01, (1-way ANOVA)

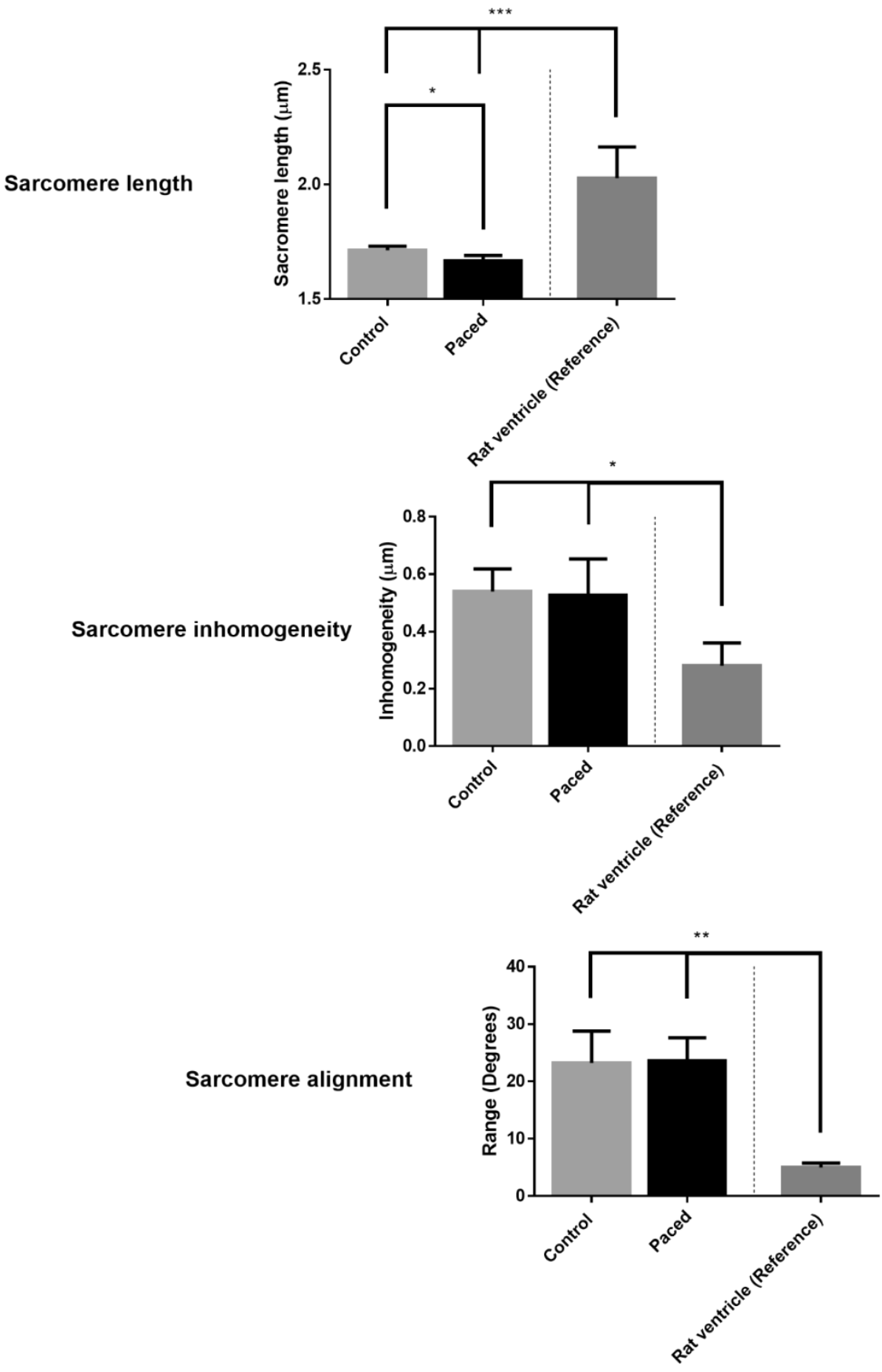

Figure 4.11 Cell structure after photostimulation period (96 hours)
96 hours of photostimulation caused a significant shortening of sarcomere length but caused no changes in sarcomere inhomogeneity or alignment (iPSC-CM N = 4 wells, 10 cells/well. Rat ventricle N = 3 animals, 10 cells/animal). * P≤0.05, ** P≤0.01, *** P≤0.001 (1-way ANOVA)

4.4 Discussion

4.4.1 Chronic pacing at a single site causes cell death

Prolonged photostimulation of a single site caused significant damage to the cells being stimulated. This indicated a potential toxic effect of the photostimulation protocol. This effect was studied in detail in chapter 5.

4.4.2 48 hours of patterned photostimulation caused changes in spontaneous rate

Changing the photostimulation protocol to include multiple stimulation sites within a single well did not prevent cell death after 48 hours. As a result, the protocol was further altered to reduce the duty cycle of each well of cells to 50% by alternating stimulation between 2 adjacent wells. This adaptation allowed cells to be paced for 48 hours with no apparent signs of damage.

Cells paced at 2 Hz for 48 hours showed no changes in structural or functional phenotype. Before extending the protocol duration, the work rate of the cells was increased by increasing photostimulation frequency to 3 Hz. The increased pacing frequency led to an increased spontaneous cycle length after 48 hours (Figure 4.4), contrary to previous work showing an adaptation of spontaneous frequency to pacing frequency[148]. Spontaneous activity is one of the major markers of immaturity in iPSC-CMs[45,50,64] which is likely caused by a lack of I_{k1}[151] and increased I_f expression[152]. The decreased spontaneous rate observed in cells paced at 3 Hz could arise from several changes including an increase in I_{k1} or decrease in I_f. This could be verified by western blotting, or by examining the stability of the resting membrane potential using patch clamping or red-shifted voltage sensitive dyes. As the spontaneous rate of iPSC-CMs is so variable (Figure 2.5), 3 Hz stimulation was used for all subsequent experiments to ensure the endogenous rate of the cells was consistently overridden.

4.4.3 Commercially available iPSC-CMs have a markedly different sarcomeric structure from isolated adult cardiomyocytes

The resting sarcomere length of adult rat ventricular cardiomyocytes is around 2 μm (Figure 4.11) and around 2.2 μm in human cells[153]. When kept in culture,

Isolated cardiomyocytes undergo dedifferentiation characterised by loss of rod-like morphology[153], decreased sarcomere alignment, and spontaneous electrical activity[154]. The foetal nature of these dedifferentiated cells is remarkably similar to that of iPSC-CMs and indicates the structural and electrical environment of the heart plays a significant role in increasing and maintaining cardiomyocyte maturity. This is consistent with studies attempting to replicate the physical environment of the adult heart in immature cell types

Simulating pressure load using cyclic stretching in engineered heart tissues produces cardiomyocytes with an increased sarcomere alignment and rod-like morphology[52,53]. The elastic modulus of the adult heart is approximately double that of the neonatal heart[155] which in turn is threefold greater than the embryonic heart[156]. Using microfabricated flexible posts to simulate the elastic modulus of the developing epicardium, sarcomere length and sarcomere alignment has been shown to increase with increasing elastic modulus[157].

Assays replicating the mechanical conditions of the mature heart are low throughput and as such commercial stem cell derived cardiomyocytes are differentiated in vitro using biochemical factors to increase product yield. As a result, commercial cells develop in a non-physiological structural environment resulting in a sarcomeric structure that is less organised than adult cells[64,153,158].

The decreased sarcomere length observed in these cells has a significant effect on contraction kinetics. At sarcomere lengths shorter than 1.9 μm, unloaded shortening velocity (V_o) is dependent on sarcomere length[159,160]. This dependency is due largely to the viscoelastic forces of sarcomeric proteins, namely titin[161], opposing shortening[162]. Given a resting length of 1.76 μm (Figure 2.9) and assuming a fractional shortening of 5%[51], sarcomere length would be reduced to 1.67 μm at peak contraction. This means that contraction velocity becomes progressively slower approaching peak contraction and may account for the domed peak seen in contraction traces (Figure 4.12). Of course, there is an assumption that the sarcomere length observed in iPSC-CMs is the resting length. Due to the spontaneous nature of these cells it is possible that some level of contraction occurred during fixation, skewing the results towards a shorter length. This could be tested by removing extracellular calcium or the addition of an excitation contraction uncoupler (such as blebbistatin) before fixation.

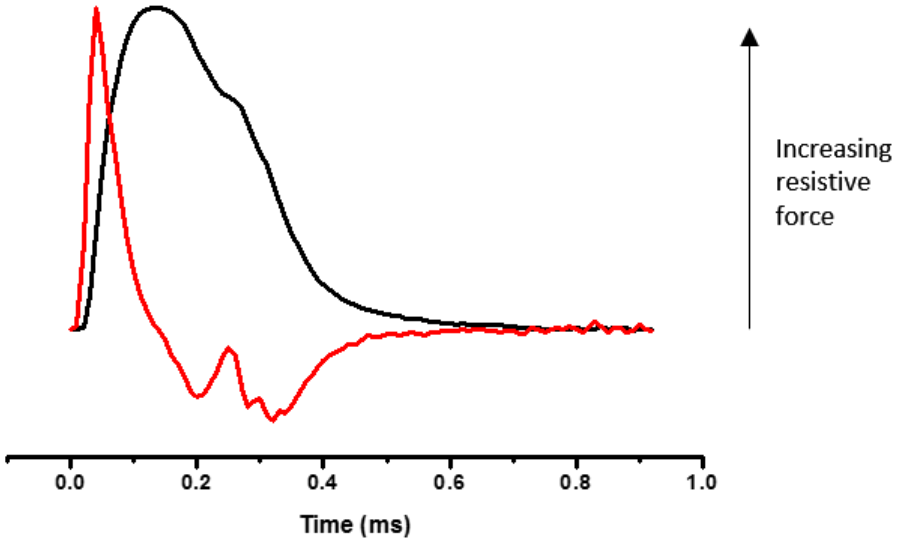

Figure 4.12 Contraction and contraction velocity
Contraction velocity (red line) was estimated by calculating the derivative of a spontaneous contraction trace (back line). Contraction velocity begins to decrease before peak contraction is reached due to increasing internal resistive forces caused by the reduction in sarcomere length.

4.4.4 96 Hours of patterned photostimulation at 3 Hz caused changes in cell function and structure.

During the extended pacing protocol there was again a significant increase in spontaneous cycle length after 48 hours of 3 Hz photostimulation, however this increase was lost after 24 hours of rest. Although not significant, a similar trend was present in stage incubator control cells. This trend was not present in cells kept in the full incubator. The cycle length of stage incubator cells was significantly greater than that of full incubator cells at 96 hours, but not at 24 hours post (Figure 4.10). This highlights the possibility that the phenotypic changes observed might be caused by improper function of the stage incubator. Incubator function was tested in chapter 5 where it was determined that humidity was being inadequately controlled.

Low incubator humidity would cause evaporation of cell media and result in an increased extracellular solute concentration. This increase would affect the cells in several ways. An increase in H^+ concentration would cause acidosis and adversely affect cell function, however the presence of HEPES buffer in cell media should prevent this from occurring.

Increased concentration of other solutes would result in hypertonicity of the cell media. Hypertonic solutions are often used to cause detubulation of muscle cells in order to study the effects of t-tubule dysfunction[163]. Treatment with a hypertonic glycerol solution causes an initial decrease in cell volume. Over time, cell volume is restored to pre-treatment levels as glycerol enters the cell accompanied by an osmotically equivalent volume of water[164]. Replacement of the hypertonic solution with normal solution results in a rapid increase in relative cell volume causing osmotic shock and detubulation. Glycerol was absent from the cell media used in this project however recovery of cell volume could still occur through the movement of other cell permeant solutes. Increased extracellular ion concentrations would lead to an increased influx of Na^+ and Ca^{2+} during an action potential. Overtime this could increase the osmolarity of the cell and cause recovery of cell volume. However, ion flux is very slight, and any change of internal concentration and cell volume would be minimal. The altered ion distributions would however have significant effects on cell electrophysiology.

The resting membrane potential, as described by the Goldman-Hodgkin-Katz equation (Equation 3.1), is determined by the distribution of ions, and the permeability of the membrane to said ions.

Equation 4.1 Goldman-Hodgkin-Katz equation
Where E_M is the resting membrane potential, R is the universal gas constant, T is the absolute temperature in kelvin, F is the Faraday constant, P is the relative membrane permeability to ion x $[x]_o$ is the extracellular concentration of ion x and $[x]_i$ is the intracellular concentration of ion x.

$$E_M = \frac{RT}{F} \ln \left(\frac{P_{Na^+}[Na^+]_o + P_{K^+}[K^+]_o + P_{Cl^-}[Cl^-]_i}{P_{Na^+}[Na^+]_i + P_{K^+}[K^+]_i + P_{Cl^-}[Cl^-]_o} \right)$$

An increase in extracellular ion concentrations would lead to a more positive resting membrane potential. The increased membrane potential could cause slow inactivation of voltage gated sodium channels leading to the increased cycle lengths observed after 48 and 96 hours of pacing (Figure 4.6). However, a reduction in cell volume due to the hypertonicity of the extracellular solution would cause the intercellular concentrations to rise accordingly meaning that the resting potential would be minimally affected. Increased $[K^+]_i$ could lead to

increased inward rectifying current, causing stabilisation of the resting membrane potential and prolonging the cycle length.

The transient nature of this change likely due to osmotic shock caused by the rapid replacement of cell media. Damage to the cell monolayer would result in reduced current sinking, and reduced membrane capacitance decreasing the time taken for spontaneous action potential generation, consistent with the reduced cycle length observed in these cells (Figure 4.6). This is speculation however and the precise cause of the change in cycle length remains unclear.

Hypertonicity of the extracellular solution might also explain the reduction in sarcomere length in paced cells. Reduced cell volume due to hypertonicity has been shown to increase Ca^{2+} content of the sarcoplasmic reticulum (SR) by way of an increase in resting $[Ca^{2+}]_i$ associated with the decreased cell volume[165]. The immature SR of iPSC-CMs[72,166,167] would not remove Ca^{2+} from the cytosol as effectively meaning the resting $[Ca^{2+}]_i$ level would remain elevated. Over time, the Na^+/Ca^{2+} exchanger would work to oppose this increase, however the increased entry of Ca^{2+} into paced cells via both L-type Ca^{2+} channels and ChR-2 could prevent any significant reduction in diastolic $[Ca^{2+}]_i$ in these cells. Elevated diastolic $[Ca^{2+}]_i$ in paced cells would reduce dissociation of Ca^{2+} from contractile myofilaments, resulting in the significantly shorter sarcomeres seen in paced cells (Figure 4.11).

The increase in Dn90 observed after the 24-hour rest period in photostimulated cells was mirrored in unpaced, full incubator cells indicating that the increase may be a result of the age of the cells rather than a consequence of the pacing protocol.

The significant changes in contraction kinetics observed in control cells kept in the stage incubator are likely due to the changes in spontaneous cycle length. Due to a stimulation artefact, only recordings from spontaneously active cells could be used. As the beating rate was not controlled during contractility recordings these results are heavily influenced by the changes in spontaneous cycle length. Later experiments utilised a longpass filter to allow simultaneous photostimulation and contractility recording.

4.4.5 Conclusions

This chapter has demonstrated that, with some adaptations, photostimulation can be used to pace cells for 96 hours. It has however highlighted an inadequacy in the stage top incubator as well as a toxic effect of photostimulation. These issues must be addressed before directionality can be introduced to the pacing protocol and are investigated in detail in chapter 5.

Chapter 5: Investigation and resolution of issues arising from chronic pacing trial

5.1 Introduction

Chapter 4 identified 2 factors affecting chronic pacing. 1) single site photostimulation resulted in severe cell damage and loss of stimulation-contraction coupling at the end of the 48-hour pacing period. 2) Multi-site photostimulation experiments demonstrated a potential failure of the stage-top incubator. Changes in spontaneous cycle length of stage control cells were absent in control cells kept in the full-size incubator. Before directionality can be introduced to the chronic pacing protocol, the toxic effect of photostimulation and the stability of the stage incubator in terms of moisture and CO_2/pH must first be investigated.

5.1.1 Incubator function

Bicarbonate buffer is included in cell media to maintain the pH of the solution at physiological levels. Hydrogen concentration is maintained through the following reaction:

Equation 5.1 Bicarbonate equilibrium
Bicarbonate equilibrium reaction by which pH can be maintained with constant perfusion of CO_2

$$CO_2 + H_2O \rightleftharpoons H_2CO_3 \rightleftharpoons HCO_3^- + H^+$$

For pH maintenance to work effectively using a bicarbonate buffer, adequate CO_2 partial pressure must be maintained or the solution will become basic. As seen in control cells in the previous chapter, there was a tendency for the spontaneous cycle length to vary over time. Although not significant this trend could indicate possible cellular damage in un-photostimulated cells, which could be due to improper incubator function. The most likely parameters that could result in cellular damage is inadequate CO_2 levels leading to an increase in pH, or inadequate humidification leading to evaporation and a subsequent increase in extracellular ionic concentrations.

To test incubator function, two fluorescent indicators were employed, 2',7'-bis-(2-carboxyethyl)-5-(and-6)-carboxyfluorescein (BCECF), and calcein. BCECF is a fluorescent pH indicator sensitive to pH changes around cytoplasmic norms[168](Figure 5.1). Calcein in its membrane permeable AM form is often used as a marker of cell viability. In its free acid form, calcein is useful as a marker of

fluid volume, as any change in volume will alter the concentration, and therefore, the level of fluorescence.

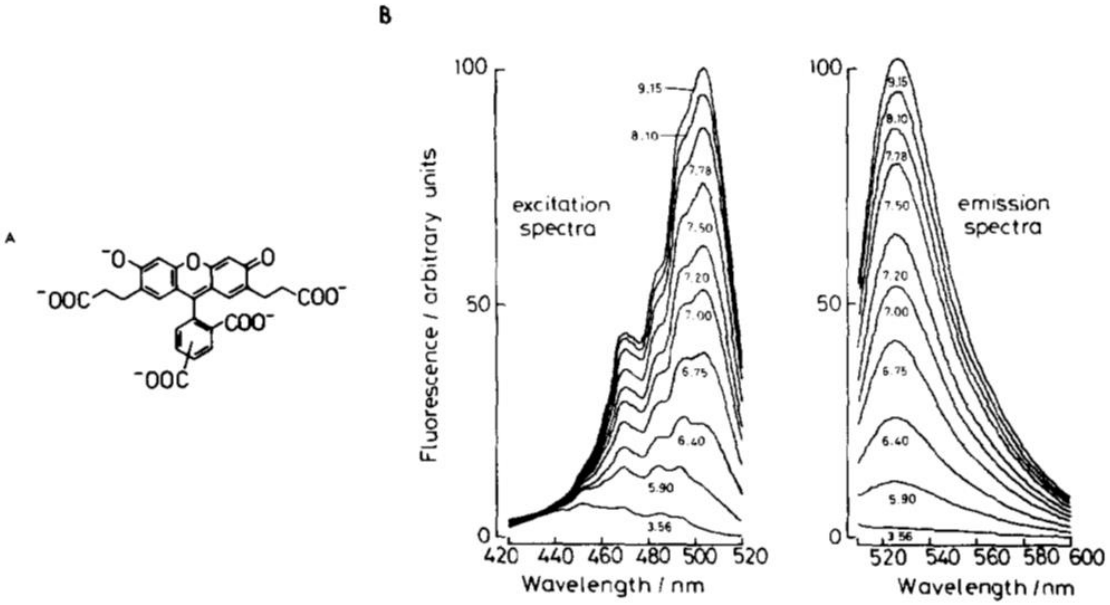

Figure 5.1 Structure and spectra of BCECF
(A) Structure of bis(carboxyethyl)carboxyfluorescein (BCECF). (B) Excitation and emission spectra of 70 nM BCECF at the indicated pHs. The calibration solution contained 130 mM KCI, 10 mM NaCI, I mM $MgSO^{+}$, and 10 mM Na MOPS. pH was altered by addition of IM HCI. Excitation spectra recorded at 530 nM in "energy" mode. Emission spectra recorded with excitation at 500 nm, in "ratio" mode. Hill plots of excitation and emission signal at 500 and 530 nm, respectively, give apparent pK~s of 6.96 and 6.98. Figure obtained from Rink et al 1982[168]

5.1.2 Electrical stimulation causes tissue damage.

There is extensive evidence that implanted pacing electrodes cause damage and fibrosis to the surrounding myocardium[169-172].There are 2 main theories as to the underlying cause of stimulation induced tissue damage. The first of these proposed mechanisms is the mass action theory, where hyperactivity of the stimulated tissue causes changes in the local electrophysiological environment[173]. The second proposed mechanism is the generation of toxic products at the surface of the electrode itself. Faradaic reactions in the presence of oxygen causes the production of reactive oxygen species(ROS)[149].These free radicals can cause protein oxidisation and alteration of amino acids[174,175], as well as oxidising DNA structures[176].

5.1.3 Phototoxicity

Phototoxicity describes the ability of a chemical substance to produce toxic effects upon exposure to light. This ability has been used previously in a

technique known as photochemotherapy. This involves the use of a chemical photosensitiser coupled with light therapy to target cancerous cells[177]. In a less clinical setting, phototoxicity occurs during imaging experiments with optical dyes, during which interaction between light and the fluorophore causes the generation of reactive oxygen species, resulting in loss of plasma membrane integrity[178]. In this case, the optical dye acts as the photosensitising agent.

There is evidence to suggest that phototoxicity can occur without the addition of a photosensitiser. Exposure to high intensity blue light (400-500 nm) has been shown to have an anti-microbial effect. It is likely that the toxic effect of illumination is photochemical in nature as illumination had negligible effects on temperature or composition of cell media[179]. It has been shown that in some bacterial species, phototoxicity is oxygen dependent[180], suggesting that the production of ROS may play a role. This is reinforced by work showing that presence of light sensitive proteins such as phycobiliproteins in certain microorganisms can result in the production of ROS when exposed to oxygen and light[181].

Of perhaps greater relevance to this project is work showing the phototoxic effect of a channelrhodopsin-2 variant (D156A) in human melanoma cells[182]. Three days of exposure to pulsed illumination (470 nm, 6.0 mW/mm^2, 1s on 10s off) significantly increased the percentage of apoptotic cells when compared to illuminated cells with negative expression and non-illuminated cells with positive expression. The increased levels of apoptosis in the experimental group were attributed to an increase in cytosolic Ca^{2+} levels, which was corroborated increased apoptotic levels in cells treated with calcium ionophore. Interestingly there was a small but significant increase in apoptosis in illuminated control cells compared to non-illuminated transfected cells. These results indicate that the illumination pattern, the light intensity and the Ca^{2+} entry via channelrhodopsin all contribute to the final cytotoxic effect.

5.1.4 Aims

The aims of this chapter were to:

1) Identify faults in incubator function and attempt to correct issues

2) Quantify cellular damage caused by chronic optogenetic stimulation of a single site.

3) Determine if damage arose due to photocurrent injection or as a direct result of prolonged exposure to 470 nm illumination.

5.2 Methods

5.2.1 pH measurements

To ensure pH changes could be detected, BCECF fluorescence was recorded at pHs of 6.9, 7.2, 7.4, 7.6 and 7.9. 0.5 μM BCECF was added to cell media in a glass bottomed 96 well plate and fluorescence was recorded (Excitation: 470 nm. Emission: 535-585 nm) periodically over 48 hours.

5.2.2 Evaporation measurements

A 96 well plate was filled with water and weighed before placing in the stage incubator for 48 hours. The plate was reweighed every 24 hours.

2 μM Calcein was used as a marker of relative fluid volume. Fluorescence was measured (Excitation: 470 nm. Emission: 535-585 nm) periodically over 48 hours. Calcein fluorescence was calibrated by measuring fluorescence at concentrations of 0.1, 0.2, 0.5, 1, 2 and 5 μM.

5.2.3 Cell Plating and viral transfection

Cells were plated under standard plating conditions. 12 wells were transfected at an MOI of 2500 and 6 wells received no virus.

5.2.4 Photostimulation

6 wells of transfected cells and 6 wells of untransfected cells underwent extended stimulation. 6 wells of transfected cells were left unstimulated as controls (Figure 5.2). A single cell area per well was exposed to 3 Hz 5 ms pulses of 470 nm light with an intensity of 1.36 mW/mm^2 for 48 hours. Cell contraction

was recorded every 10 minutes using open source automation software (Perfect Automation) in conjunction with standard contraction protocols.

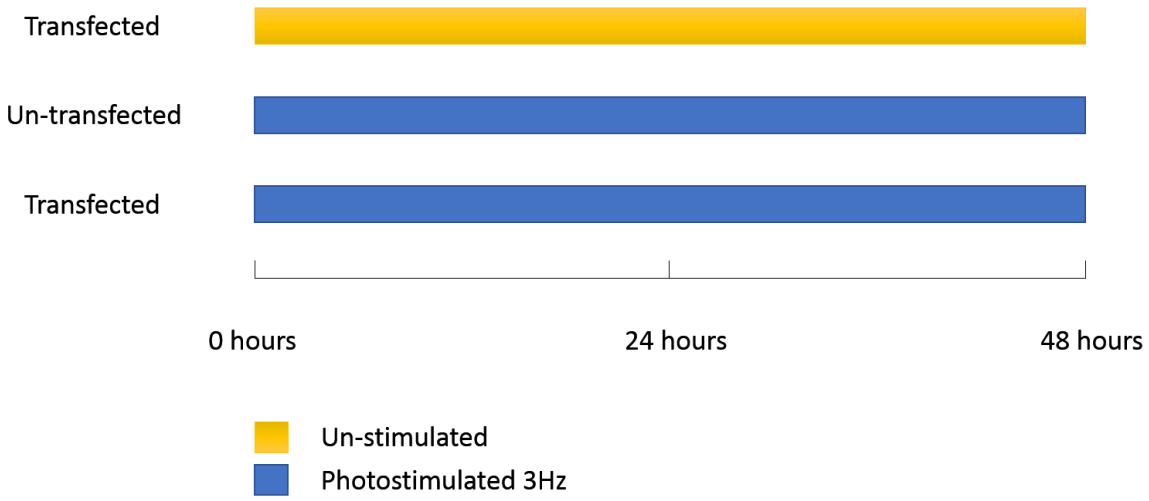

Figure 5.2 Mortality protocol timeline
Transfected cells were either photostimulated at 3 Hz (Blue) or left un-stimulated (Yellow). Untransfected cells were also photostimulated at 3 Hz (Blue). Cells were recorded every ten minutes for up to 48 hours.

5.2.5 Image analysis

5.2.5.1 Functional parameters

Contraction amplitude, cycle length, and duration at 50% contraction was acquired using the ImageJ macro previously described. The average percentage change per hour was plotted up to 24 hours (Figure 5.8)

5.2.5.2 Cell area

In ImageJ a single image from hourly recordings was used to determine the total area occupied by cells. The background was subtracted from each image using a rolling ball radius of 2.0. The image was then thresholded and converted to a binary image. The total area of the particles within the binary image was used as a measure of the total cell area. The cell area over 48 hours was plotted and the gradient used to compare change in cell area between conditions (Figure 5.8).

5.2.6 Statistics

Conditions were compared using a one-way ANOVA or 2-way ANOVA where appropriate. All data are displayed as mean ± SEM. A p value of 0.05 or less was considered significant.

5.3 Results

5.3.1 BCECF fluorescence increased despite the presence of 20 mM HEPES

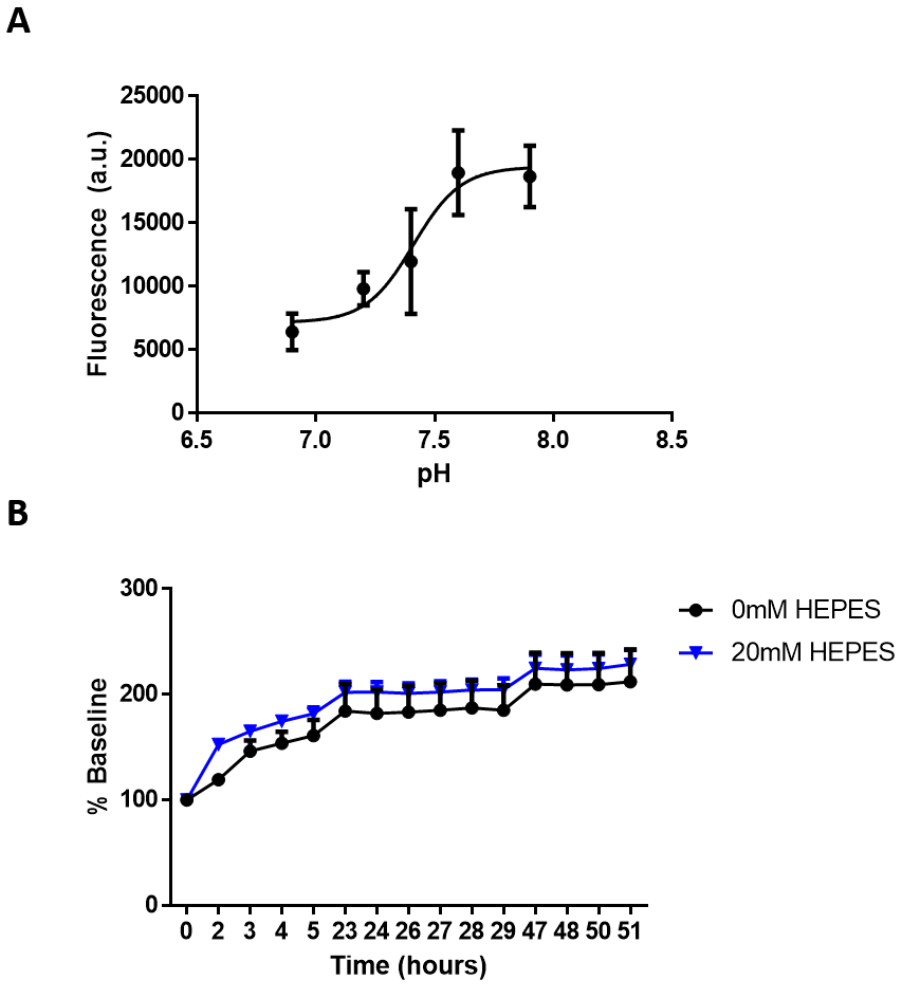

Figure 5.3 BCECF fluorescence over 48 hours
A) BCECF fluorescence response to altered pH. B) BCECF fluorescence increased with time. This increase was unaffected by the presence of 20 mM HEPES buffer (N = 3 wells).

Over the course of 48 hours there was a steady increase in BCECF fluorescence to 112% above baseline levels, and 128% in the presence of 20 mM HEPES (Figure 1.3).

5.3.2 Increase in BCECF fluorescence likely caused by volume loss

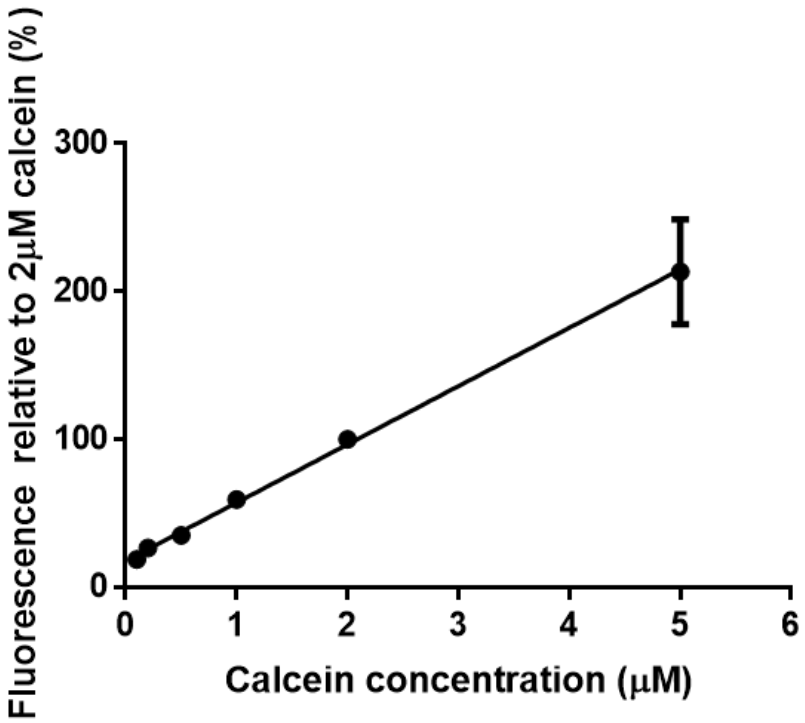

Figure 5.4 Calibration of calcein fluorescence
Calcein fluorescence relative to working concentration of 2 μM. Fluorescence increased linearly with increasing calcein concentration. Y = 39.43X + 17.77 (N = 3 wells).

After 48 hours in the stage incubator there was a 13.6% loss of volume by weight. This was accompanied by a 55% increase in BCECF fluorescence and a 160% increase in calcein fluorescence (Figure 5.5 A). Using the calcein calibration (Figure 5.4) calcein concentration was estimated to rise from 2 μM to 6.14 μM, meaning the volume in the well had decreased from 200 μl to 65 μl. This would result in BCECF concentration being increased to 1.53 μM.

Subsequently, the humidity of the stage incubator was increased from ~70% to ~90-95% by increasing the temperature of the bubble humidifier. 48 hours at this higher humidity level resulted on only a 5.5% loss of volume by weight which was accompanied by an increase in BCECF fluorescence of 10% and calcein fluorescence of 5% (Figure 5.5 B), indicating an increase in calcein concentration to 2.21 μM and a reduction in volume to 180 μl.

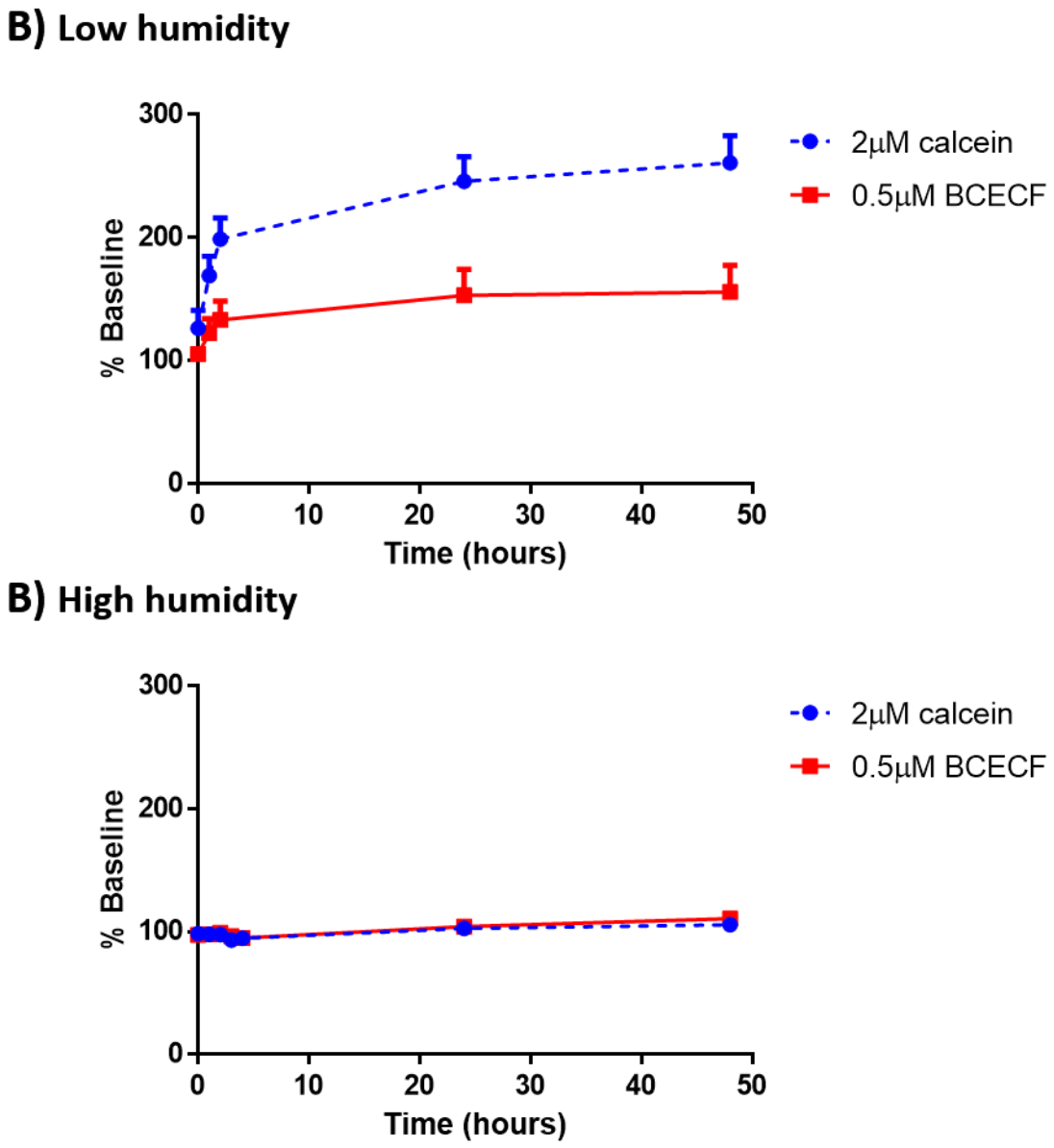

Figure 5.5 Fluorescence at high and low humidity
Fluorescence of both pH sensitive(BCECF) and insensitive(Calcein) markers was increased after 48 hours at original humidity setting (A). With the incubator humidity increased there was a negligible increase in fluorescence of both markers (B) (N = 6 wells).

5.3.3 The contraction profile of transfected, photostimulated cells alters drastically over 24 hours.

All cell areas that were both transfected and photostimulated lost 1:1 contraction coupling before 24 hours (average time for loss of coupling was 2.19 ± 1.26 hours) (Figure 5.6). Only 1 out of 6 of these areas showed any spontaneous activity at 24 hours (Figure 5.7).

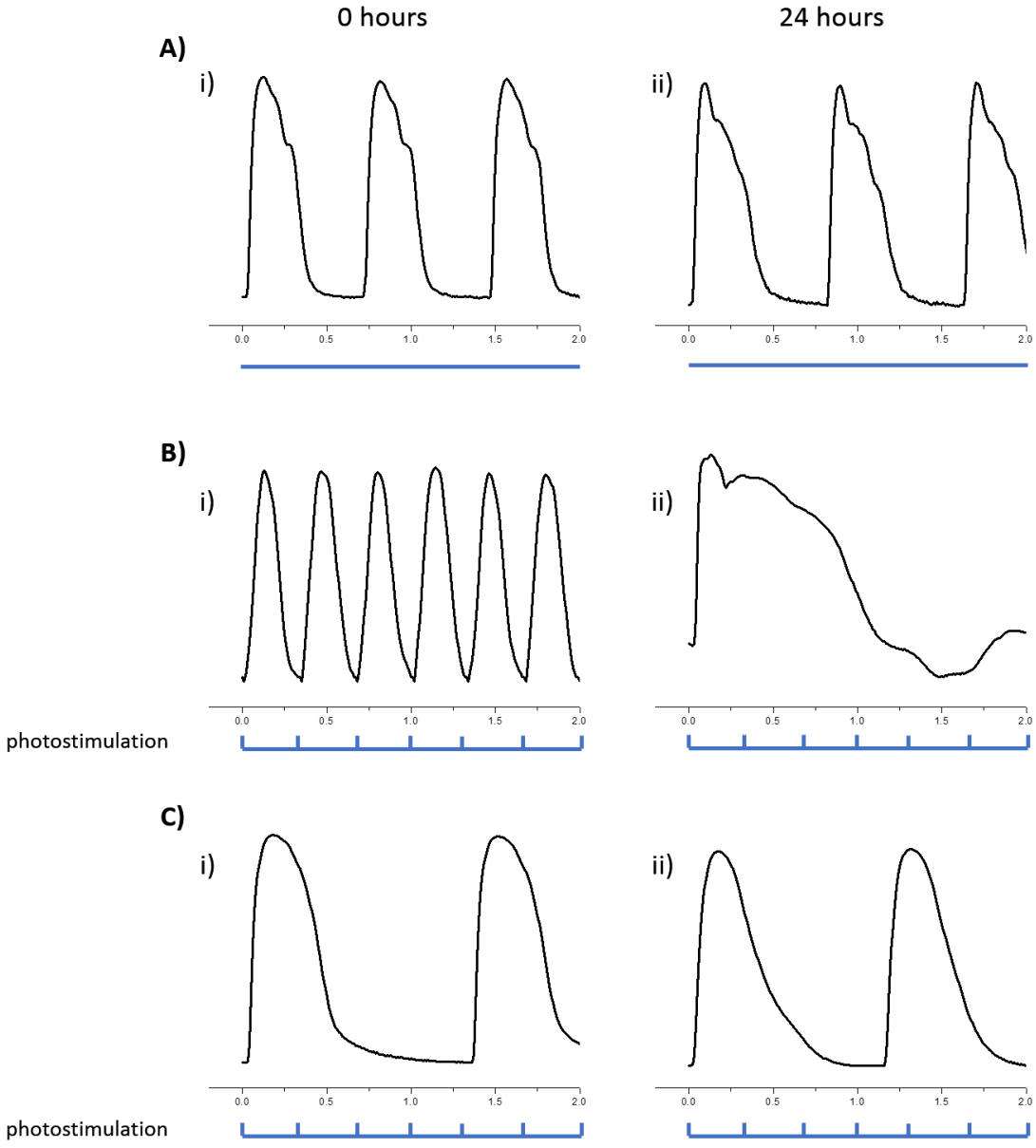

Figure 5.6 Contraction before and after
Example contraction traces for all three experimental conditions at 0 (i) and 24 hours (ii). The contraction profile remained largely unchanged in transfected unstimulated cells (A) and untransfected photostimulated cells (C). Transfected photostimulated cells (B) showed marked changes after 24 hours with total loss of stimulation-contraction coupling along with a significant increase in contraction duration.

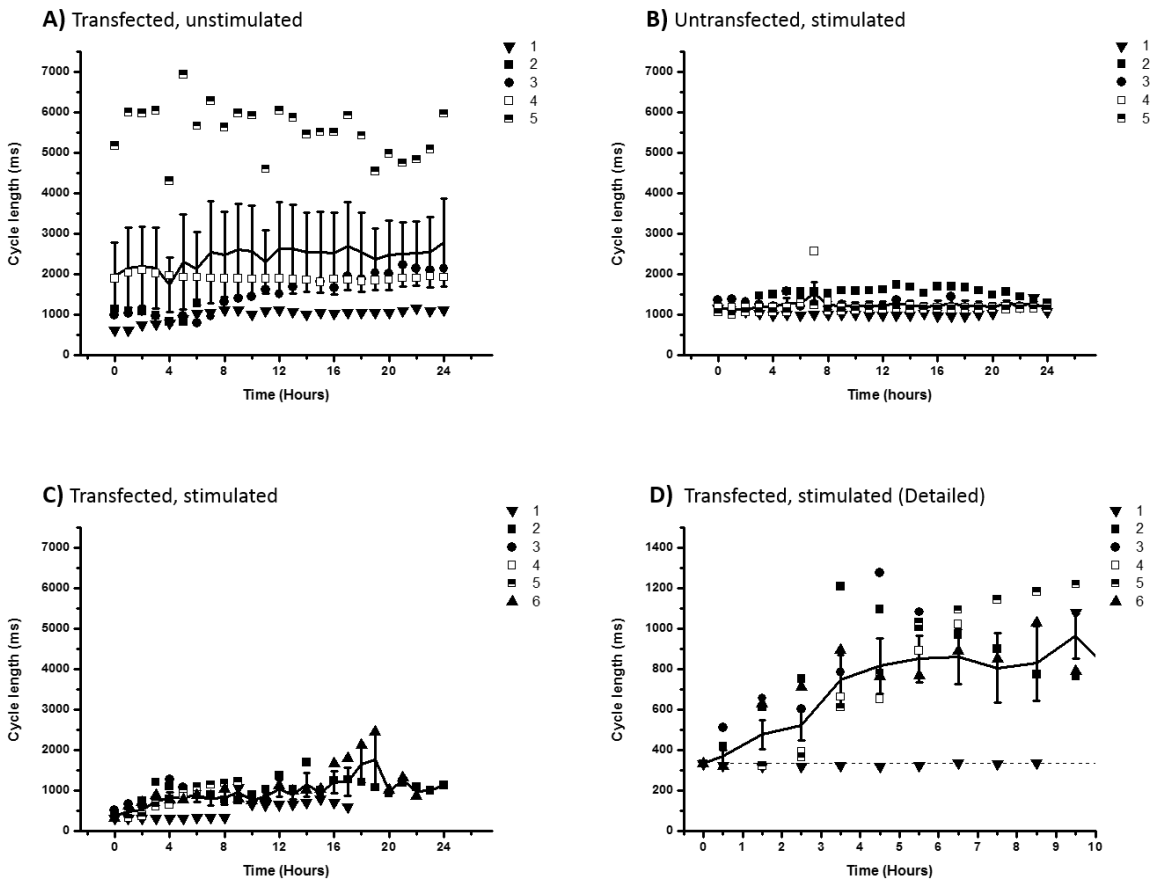

Figure 5.7 Contraction cycle length over 24 hours
Cycle lengths for the three experimental conditions over 24 hours. Cycle lengths for transfected, unstimulated cells (A, N = 5 areas), and untransfected, photostimulated (B, N = 5 areas) remained largely unchanged throughout the duration of the experiment. (Figure 5.9) Transfected, photostimulated cells (C, N = 6 areas) lost 1:1 coupling within 2.19 ± 1.26 hours (D) and only 1 of 6 cell areas still showed contraction at 24 hours.

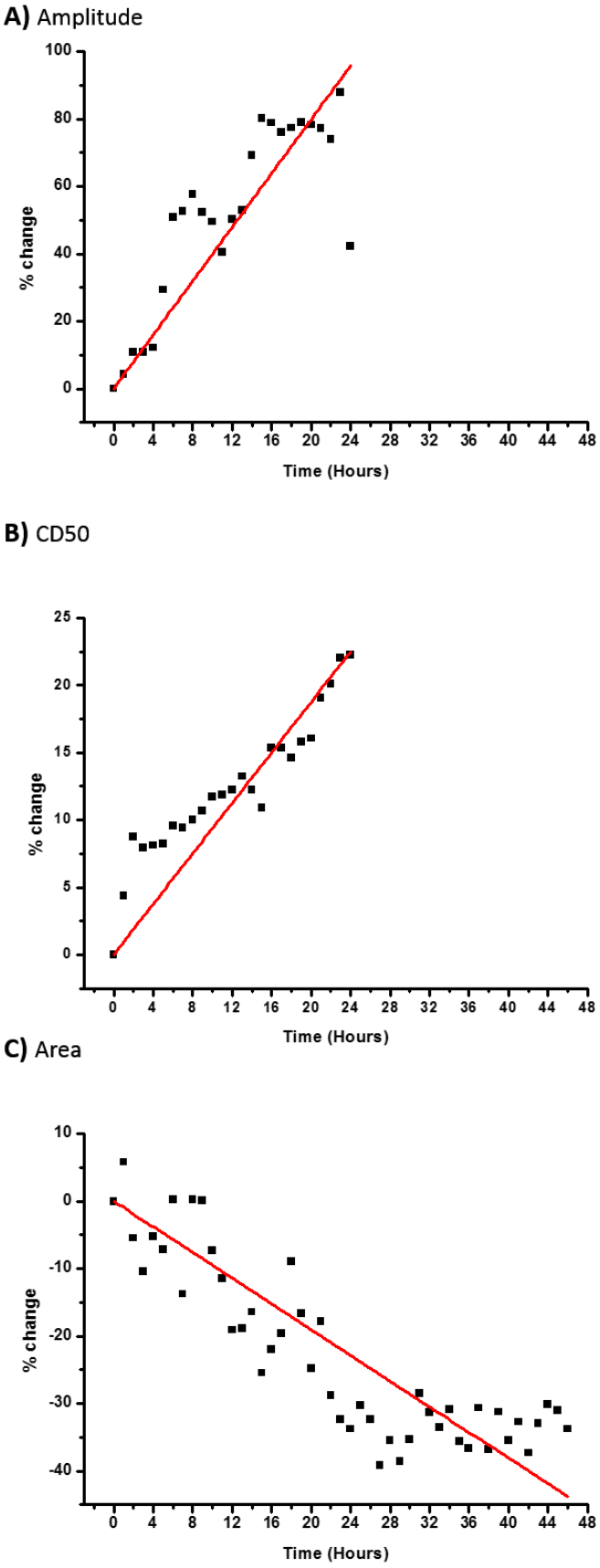

Figure 5.8 Example contraction changes over time
A) % Change in contraction amplitude, B) CD50 and C) cell area was plotted against time. As changes in amplitude and cell area are relative, the rate of change was used to identify significant differences between experimental conditions.

5.3.4 Rate of change was unaffected by transfection or photostimulation

There were no significant differences in rate of change of spontaneous amplitude, area, cycle length or CD50 between the 3 experimental groups. (Figure 5.9).

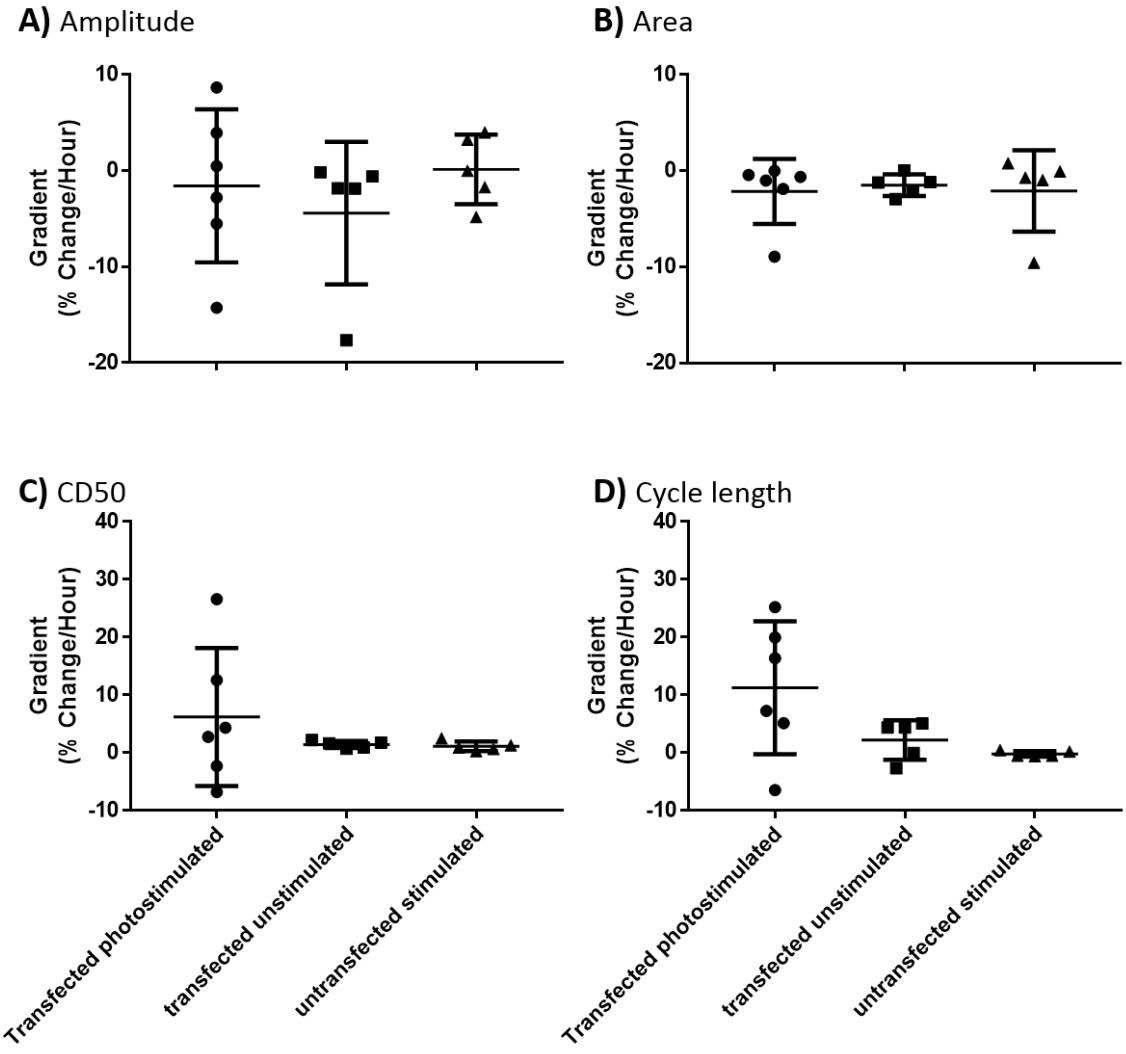

Figure 5.9 Contraction gradients post protocol
Average % change/hour in A) Amplitude, B) cell area, C) cycle duration at 50% contraction and D) cycle length. There were no significant changes in amplitude or area across all three conditions (Transfected, photostimulated N = 6 areas, transfected, unstimulated N = 5 areas, untransfected stimulated N = 5 areas) The gradient of CD50 and cycle length % change over time was significantly more positive in transfected photostimulated cells.

5.3.5 The presence of channelrhodopsin alters cell contractility

Untransfected cells showed no change in amplitude, cell area, CD50 or cycle length at the end of the experimental period (Figure 5.10). Transfected, photostimulated cells showed a significant decrease in cell area at the end of the 48-hour pacing period (100% vs 55.99 ± 13.45%, p = 0.0174 2-way anova) as well as a significant increase in CD50 (151.73 ± 10.17 ms vs 425.78 ± 62.11 ms, P = 0.0002 2-way anova) and cycle length (368.71 ± 32.54 ms vs 985.17 ± 92.33 ms, P = 0.0006). Transfected, unstimulated cells also showed small but significant increases in CD50 (382.81 ± 54.67 ms vs 538.67 ± 62.75 ms, p = 0.0331) and cycle length (1963.45 ± 828.29 ms vs 2487.80 ± 889.83 ms, p = 0.0051 2-way anova) (Figure 5.10).

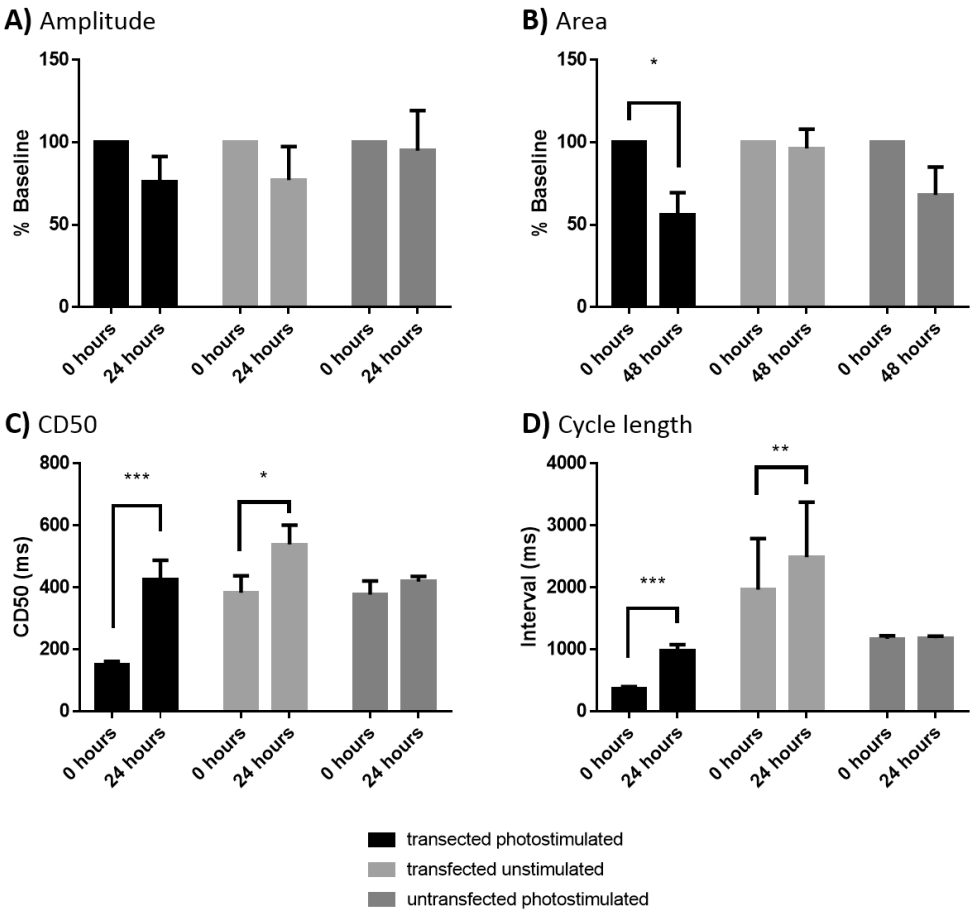

Figure 5.10 Cell function and coverage pre and post protocol
Initial values for A) amplitude, B) area, C) CD50 and D) cycle length compared to terminal values. There were no significant changes in contraction amplitude in any of the experimental groups. Cell area in the transfected, photostimulated group was significantly reduced after 48 hours of photostimulation. After 24 hours, CD50 was significantly increased in both the transfected, photostimulated group, and the transfected unstimulated group. Cycle length was also significantly altered in these groups (Transfected, photostimulated N = 6 areas, transfected, unstimulated N = 5 areas, untransfected stimulated N = 5 areas).

5.4 Discussion

5.4.1 BCECF fluorescence increased despite the presence of 20 mM HEPES

BCECF fluorescence increases with increasing pH (Figure 5.1, Figure 5.3A). Insufficient partial pressure of CO_2 would cause the bicarbonate equilibrium to shift towards the left (Equation 5.1), removing H^+ from solution and increasing the pH of the solution. The addition of 20 mM HEPES did not prevent affect the increase of BCECF fluorescence (Figure 5.3B). Given that the buffering power of HEPES is not dependent on CO_2 partial pressure, 20 mM should have been more than adequate to prevent a significant rise in pH, meaning the rise in fluorescence was not due to insufficient partial pressure of CO_2. The increased fluorescence was therefore most likely caused by an increase in concentration caused by evaporation of media due to inadequate humidity in the incubator chamber.

5.4.2 Increase in BCECF fluorescence likely caused by volume loss

The inadequate humidity of the incubator was confirmed by a significant loss of fluid from the test plate after 48 hours along with an increase in calcein fluorescence. The change in calcein fluorescence was drastically reduced upon increasing incubator humidity indicating reduced fluid loss. Improving incubator humidity also reduced the change in BCECF fluorescence, confirming that the increase observed previously was not due to improper CO_2 partial pressure.

The increased calcein fluorescence observed at low humidity was far greater than the increase in BCECF fluorescence. As BCECF is pH sensitive, it could be hypothesised that a reduction in pH led to reduced fluorescence, opposing the increase due to concentration. However, evaporation would cause an increased bicarbonate concentration causing pH to increase meaning this hypothesis was unlikely. As calcein is Ca^{2+} sensitive, it is more likely that increased Ca^{2+} concentration combined with the increase in indicator concentration led to disparity between calcein and BCECF fluorescence. Inconsistencies between weight measurements and volume calculations are likely due to evaporated solution condensing elsewhere in the plate, thus removing volume from the well

and influencing calcein fluorescence, but still contributing to the overall weight of the dish.

A reduction in extracellular volume would explain the changes in cycle length seen previously (Figure 4.6). Increased concentration of extracellular ions would cause an increase in resting membrane potential and a reduction in cell volume due to increased osmotic pressure (detailed interpretation in chapter 4). Restoring incubator humidity abolished the changes in spontaneous cycle-length in control cells in subsequent experiments (chapter 6).

5.4.3 The contraction profile of transfected, photostimulated cells alters drastically over 24 hours.

In adult cardiomyocytes, increased contraction frequency leads to increased force of contraction. This positive force-frequency relationship occurs as a result of increased Ca^{2+} influx via L-type calcium channels and a decreased diastolic period resulting in decreased Ca^{2+} efflux via the Na^{2+}/Ca^{2+} exchanger. In adult cells, the excess Ca^{2+} is removed to the sarcoplasmic reticulum (SR) by sarco/endoplasmic reticulum Ca^{2+}-ATPase (SERCA). This results in increased SR content, an increased intracellular Ca^{2+} transient, and an increase in contractile force.

Stem cell derived cardiomyocytes have been shown to have reduced SR capacity[72,166] where the removal of excess cytosolic Ca^{2+} to the SR is diminished, leading to a negative force-frequency relationship[72,74] similar to that seen in the failing human heart[183]. A negative force frequency relationship occurs when increased Ca^{2+} entry via the L-type Ca^{2+} channel cannot by removed by the impaired SR causing an increase in diastolic Ca^{2+}. This increase leads to reduced relaxation and therefore a reduction in contractile force. Insufficient Ca^{2+} removal during chronic pacing would cause an increased CD50 such as that observed in transfected, photostimulated cells (Figure 5.6 and Figure 5.10). This in turn would cause an increased refractory period and result in the loss of coupling observed in these cells (Figure 5.6 and Figure 5.7).

Loss of coupling may also have occurred due to a diminished photocurrent amplitude. As the ChR-2 current consists partly of Ca^{2+} flux, increased

intracellular Ca^{2+} levels would decrease the Ca^{2+} gradient resulting in a diminished inward current. This could lead to photostimulation being insufficient to depolarise the cell to the threshold required for action potential generation.

A prolonged increase in cytosolic calcium would also explain the cell death observed in transfected, photostimulated cells. Perny et al (2016) proposed an apoptotic pathway in which increased cytosolic calcium leads to release of cytochrome c from the mitochondria. This in turn leads to formation of the apoptosome leading to terminal DNA fragmentation and apoptosis[182].

In future studies this hypothesis should be tested using red-shifted Ca^{2+} and voltage sensors compatible with ChR-2 based optogenetics[184].

5.4.4 The presence of channelrhodopsin alters cell contractility

Channelrhodpsin-2 (H134R) has a constant steady state current in the presence of 470 nm light[109]. As shown previously (Figure 2.6) ChR-2 also has a broad action spectrum at the short end of the visible spectrum. As such, it is likely that brightfield illumination caused constant photocurrent injection at a level below the threshold for action potential generation. The presence of this continuous current likely causes prolongation of the plateau phase of the action potential. This prolongation would result in the prolonged contraction duration observed in transfected, unstimulated cells which in turn would result in the decreased contraction frequency also seen in these cells. As ChR-2 current is comprised of influx of several cations, prolonged channel opening is likely to prevent recovery of the resting membrane potential and cause slow inactivation of voltage gated sodium channels. This inactivation, coupled with the prolonged CD50, is likely the cause of the increased cycle length (Figure 5.10). Again, these hypotheses should be tested in future using appropriate voltage sensors.

As there were no significant changes in the untransfected, photostimulated cells, secondary effects such as increased temperature, and the generation of ROS by the stimulus light can be ruled out.

5.4.5 Conclusions

These results indicate that prolonged optogenetic stimulation of a single site of iPSC-CMs causes cell damage, future chronic pacing experiments should therefore utilise a multi-site protocol as shown in chapter 4. With incubator function restored, and a greater understanding of cell mortality, directionality was added to the chronic pacing protocol in chapter 6.

Chapter 6: Investigation into the effect of directional pacing on iPSC-CMs

6.1 Introduction

Chapter 5 investigated the issues plaguing chronic photostimulation. With these factors resolved, directionality could be introduced into the chronic pacing protocol.

6.1.1 Directional electrical activity

As mentioned in chapter 1, the very first heart beats during development arise from spontaneous activity within the immature cardiomyocytes before being overridden by the sino-atrial node. Directional activation is generated at the top (cranial) end of the heart tube, the wave of activation propagates to the dorsal end on each beat. This wave of electrical activity causes peristaltic motion with contraction direction being perpendicular to the direction of electrical activation. Previous studies attempting to increase the maturity of stem cell derived cardiomyocytes by replicating the physical environment of the developing or developed heart have been quite successful[52,53,157,185]. As such, it was hypothesised that altering the multi-site stimulation protocol to replicate the directional pattern of electrical activity seen during development could increase the maturity of iPSC-CMs.

6.1.2 Aims

This chapter aimed to determine:

1) If the improvements made to the stage incubator would prevent adverse changes to cell function.

2) If directional photostimulation could cause changes in iPSC-CM structure and function.

6.2 Methods

6.2.1 Cell Plating

Stem cell derived cardiomyocytes (Axiogenesis) were seeded onto fibronectin (1:100 PBS) coated inserts, within Mattek 35 mm glass bottomed petri dishes at a density of 25,000 cells per well.

6.2.2 Viral Transfection

Cells were incubated overnight with an adeno-associated virus containing ChR2 (Addgene# 20938M obtained from Vector Biolabs, Pennsylvania) at an MOI of 2500. Cells were then allowed to rest for 5 days to allow full expression of the ChR2 protein.

6.2.3 Contractility Recordings

Cell contractions were recorded using a Hamamatsu orca flash 4.0 camera attached to an Olympus IX71 Microscope at 40x magnification. Contractility recordings were analysed using in-house software developed by Dr Francis Burton.

6.2.4 Chronaxie determination

Responsive cells were excited at 3 Hz with a 470 nm opto-led and the threshold for response measured at 0.2, 0.3, 0.5, 0.7, 2,3,5,7,10,20,30 and 40 ms Pulse widths. These values were then fitted with an exponential and the chronaxie was taken as the pulse width for twice the rheobasic current.

6.2.5 Sarcomere analysis

6.2.5.1 Immunohistochemistry

Fixed cells were permeabilised using 0.2% triton in 1% bovine serum albumin (BSA) phosphate buffered saline (PBS) before being blocked with 10% goat serum (GS) 1%BSA PBS for 1 hour. The cells were then stained with mouse anti-α-actinin (1:500 3%GS 1%BSA PBS) overnight at 4˚C. Cells were then washed and stained with goat anti-mouse IgG alexafluor 647 antibodies (1:200 1% BSA PBS) for 1.5 hours at room temperature.

6.2.5.2 Sarcomere Imaging.

Z-stacks of cells with well-defined sarcomeres were obtained using an Olympus IX83 confocal microscope at 40x or 60x magnification.

6.2.5.3 Image analysis

Maximum intensity projections were obtained in open-source image analysis software FIJI. These images were then analysed as described in chapter 2.

6.2.6 96-hour directional pacing

In-house software was used to move the area of stimulation between 6 central sites per well. These sites were positioned in such a way that, although they would arise from either side of the measurement area, action potentials propagating from each site would share a similar directional axis (Figure 6.1). Sites were stimulated at 3 Hz with a 2 ms pulse width for 100 seconds. Stimulation was alternated between 2 adjacent inserts to allow concurrent stimulation with a duty cycle of 50%. Contractility recordings and strength duration curves were taken from central sites that did not undergo direct photostimulation. Measurements were made before pacing, after 48 and 96 hours of pacing, as well as after a 24-hour post-pacing rest period (Figure 6.1). Cell media was replaced every 48 hours and cells were fixed post-experiment using 2% paraformaldehyde (PFA).

6.3 Results

6.3.1 96 hours of directional stimulation caused minor changes to cell contractility

Patterned stimulation caused no changes to the spontaneous cycle length of paced cells (Figure 6.2 A, Figure 6.4). Although there was no change during the stimulation protocol, there was a significant decrease in the contraction upstroke time of cells paced at 3 Hz after the 24-hour rest period (72.03 ms vs 48.85 ms P=0.023 one-way ANOVA) (Figure 6.2 B). There was however, no change in the contraction downstroke time (Figure 6.2 C).

There was a temporary decrease in spontaneous cycle length in control cells (1272 ± 230 ms vs 727 ± 99 ms, P = 0.0255) however there were no significant changes in other contractility parameters (Figure 6.3)

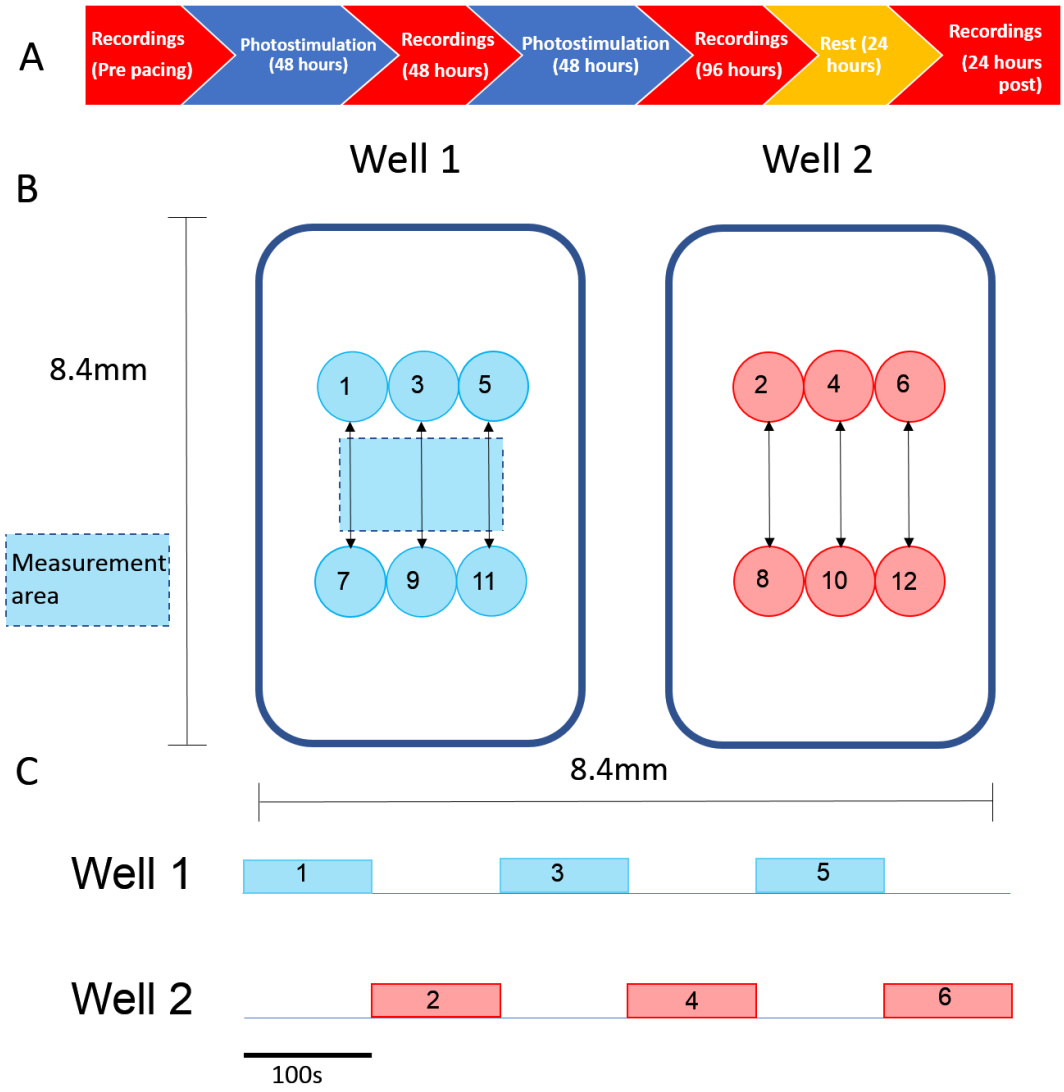

D

	Stimulation cycles per site	Stimulation time per site per cycle (seconds)	Total stimulation time per site (hours)	Rest time per site per cycle (seconds)	Total rest time per site (hours)
48 hours	144	100	4	1100	44
96 hours	288	100	8	1100	88

Figure 6.1 Directional pacing protocol
Visual representation of directional photostimulation pattern. Each site was photostimulated for 100 seconds before stimulation was moved to the corresponding site in the alternate well. This stimulation pattern was maintained for 96 hours.

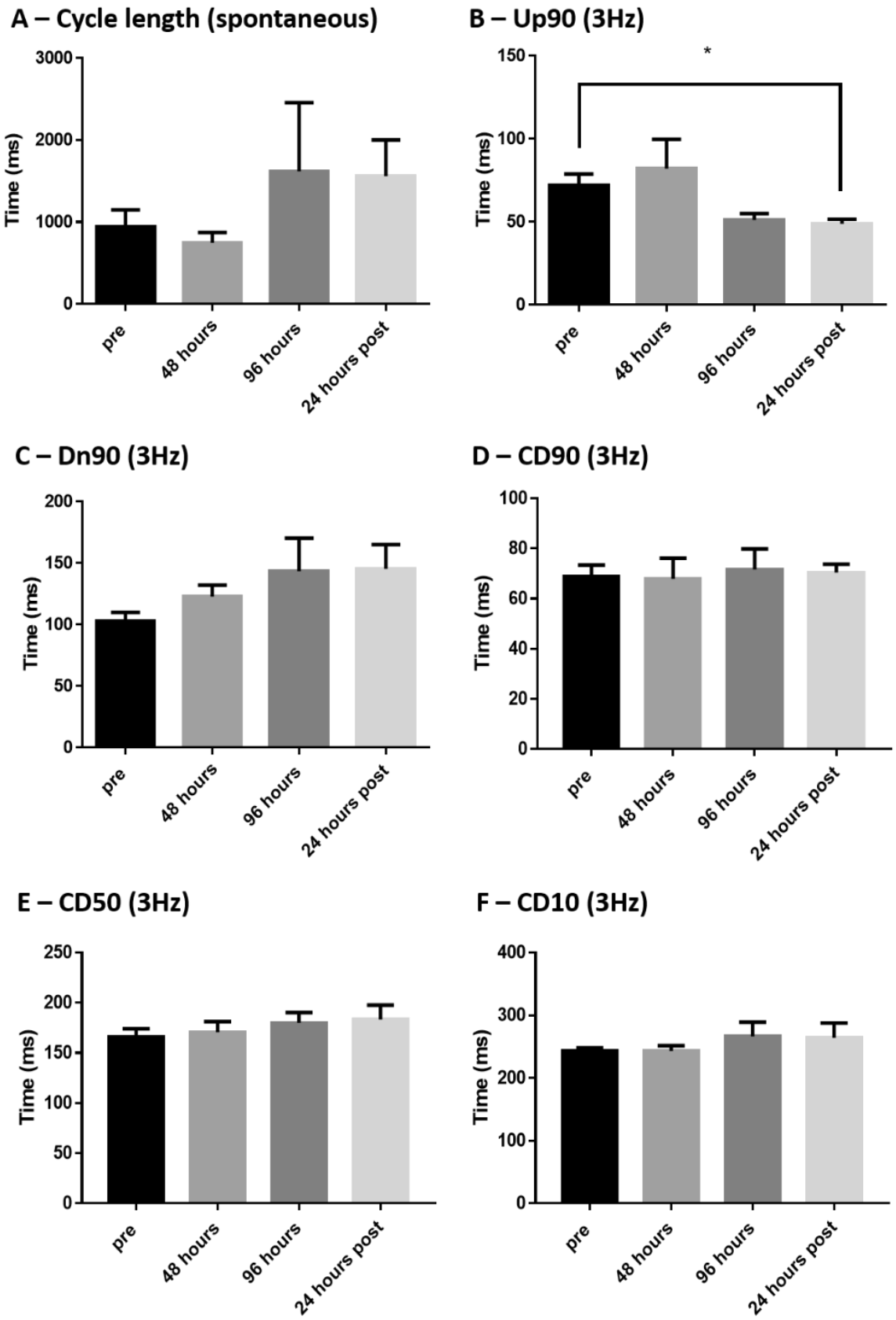

Figure 6.2 Contractility in paced cells during pacing protocol
96 hours of directional pacing caused no change in the spontaneous cycle length of the paced cells (A) or the relaxation phase of cells paced at 3 Hz (C). 24 hours after the pacing period however, there was a significant decrease in the upstroke time of the contraction phase of cells paced at 3 Hz (B) (72.03 ms decreased to 48.85 ms P=0.023 one-way ANOVA). There were no significant changes in (D) CD90, (E) CD50 or (F) CD10 (N = 6 wells).

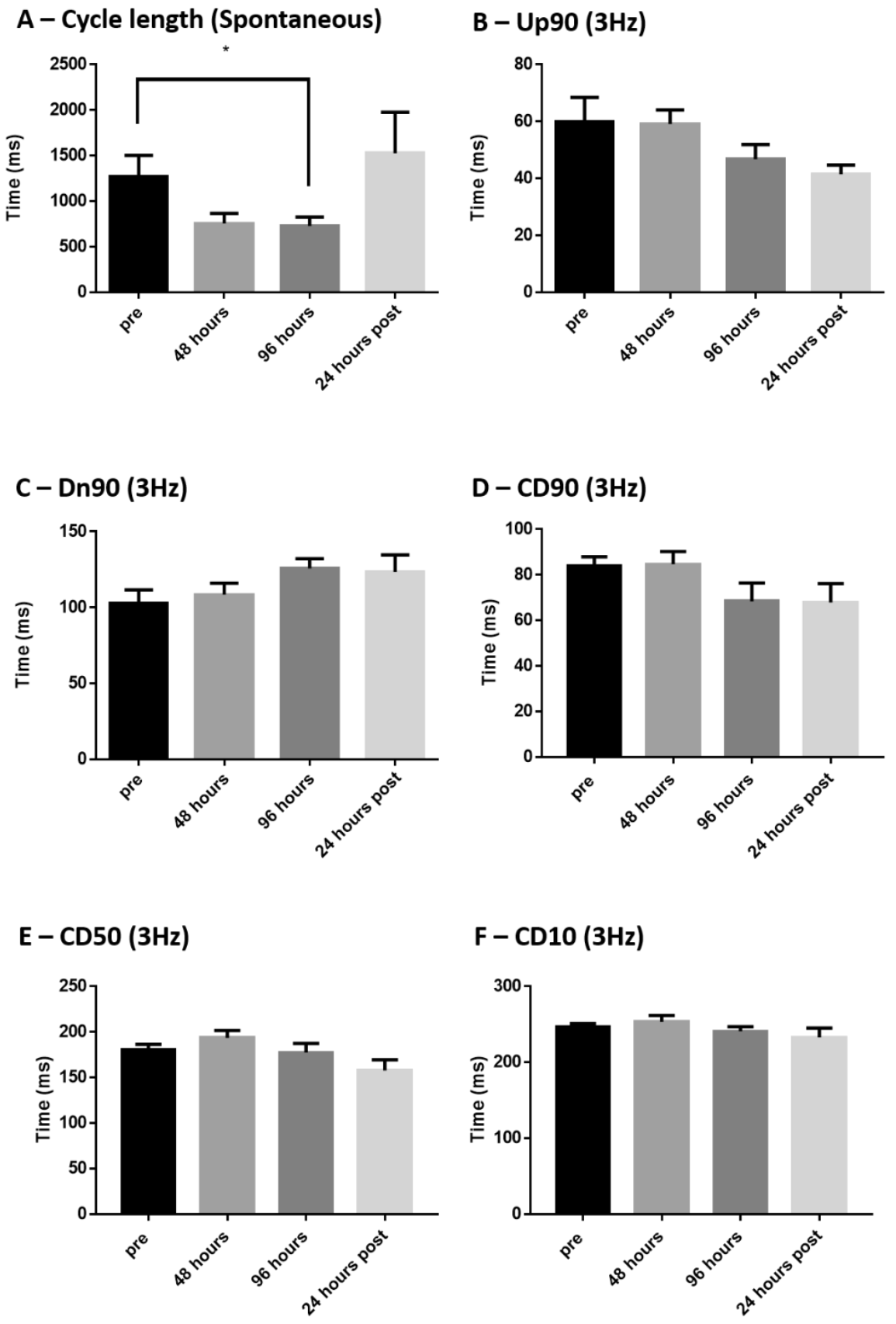

Figure 6.3 Contractility in control cells during pacing protocol
There was a significant decrease in spontaneous cycle length (A) at 96 hours which was lost at 24 hours post protocol. There were no significant changes in B) Up90, C) Dn90, D) CD90, E) CD50 or F) CD10 (N = 6 wells).

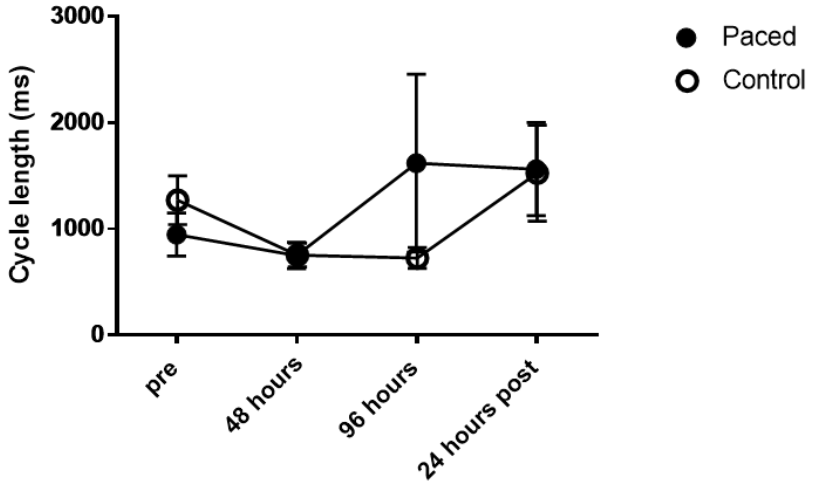

Figure 6.4 Spontaneous cycle length in control and paced cells
The spontaneous cycle length of paced cells did not differ significantly from that of control cells at any point during the photostimulation period (N = 6 wells).

6.3.2 96 hours of directional stimulation did not alter cell excitability

There were no significant changes in the chronaxie times or rheobasic stimuli of paced cells (Figure 6.5)

6.3.3 96 hours of directional stimulation did not alter cell structure

There were no significant changes in sarcomere length (Figure 6.6 A), inhomogeneity (Figure 6.6 B), or alignment (Figure 6.6 C) following 96 hours of patterned stimulation.

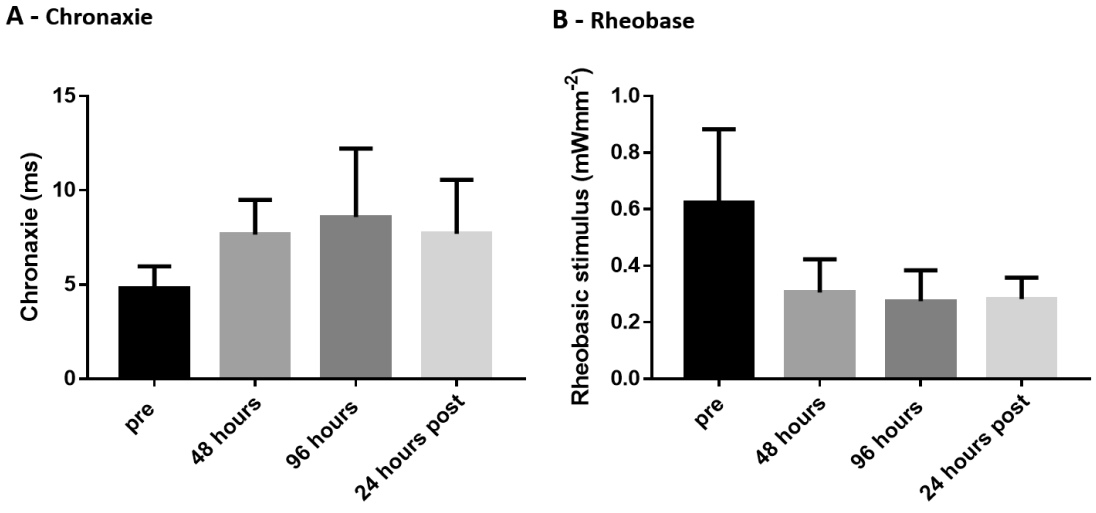

Figure 6.5 Cell excitability before and after protocol
There was no significant effect of patterned stimulation on markers of cell excitability Chronaxie (A) and Rheobasic stimulus (B) (N = 6 wells).

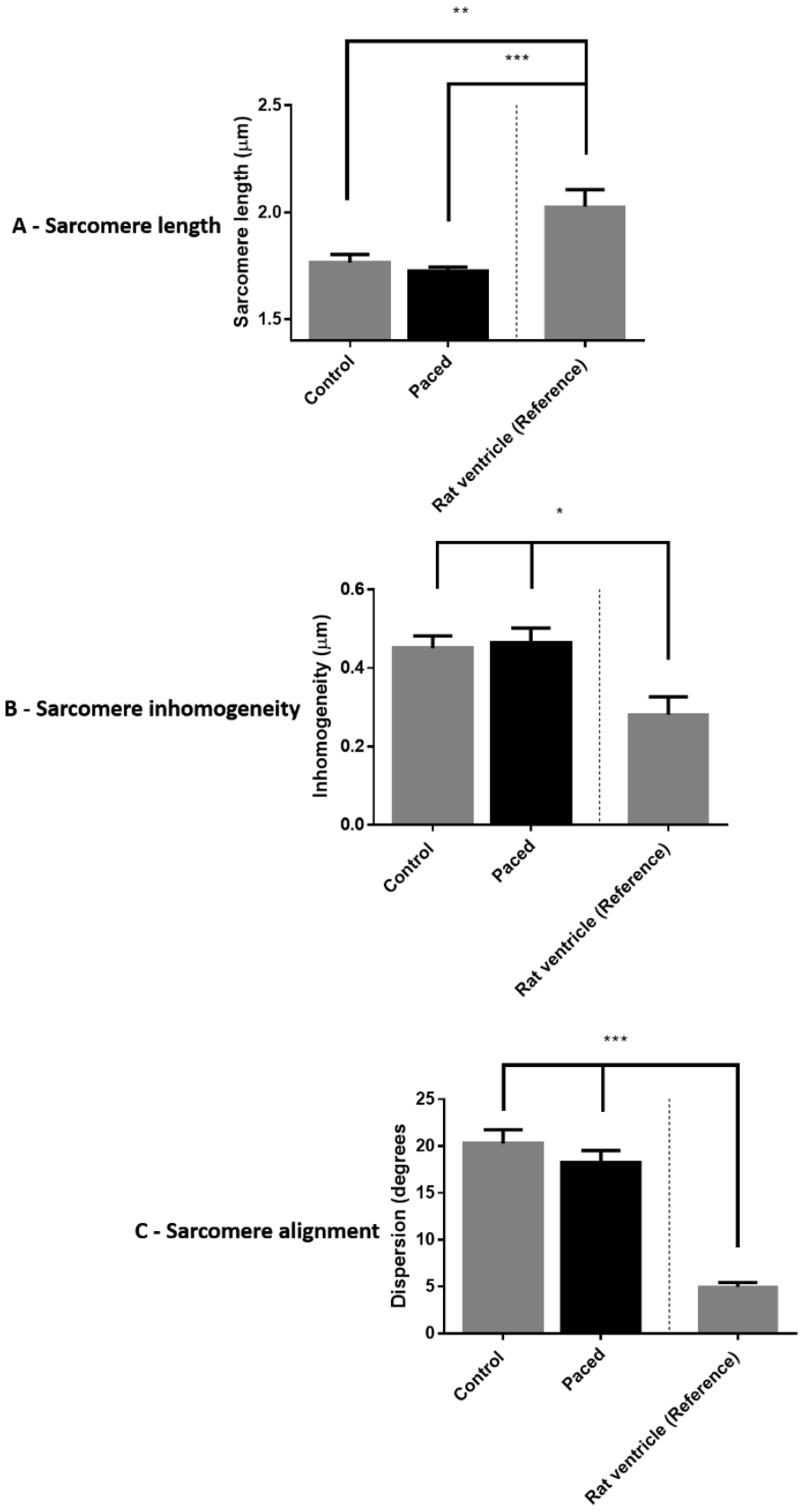

Figure 6.6 Cell structure post-protocol
Chronic directional stimulation caused no changes in sarcomere length, sarcomere inhomogeneity, or sarcomere alignment (iPSC-CM N= 6 wells, 10 cells/well. Rat ventricle N = 3 animals, 10 cells/ animal)

Table 6.1 Cell phenotype pre/post-protocol
Mean values for all directional pacing parameters in control/pre-treated cells and treated cells.

	Control	Treated
Spontaneous cycle length (ms)	946.00 ± 201.70	1562.00 ± 439.60
Up90 (ms)	72.03 ± 6.73	48.85 ± 2.78 *
Dn90 (ms)	102.80 ± 7.21	145.30 ± 19.78
CD90 (ms)	68.10 ± 4.78	70.49 ± 3.31
CD50 (ms)	165.90 ± 8.31	183.50 ± 14.4
CD10 (ms)	243.50 ± 4.56	264.60 ± 23.31
Chronaxie (ms)	4.79 ± 1.18	7.69 ± 2.87
Rheobase ($mWmm^{-2}$)	0.62 ± 0.26	0.28 ± 0.08
Sarcomere length (µm)	1.77 ± 0.04	1.72 ± 0.02
Sarcomere inhomogeneity (µm)	0.45 ± 0.03	0.46 ± 0.04
Sarcomere dispersion (°)	20.27 ± 1.47	18.21 ± 1.33
N	6 wells	6 wells

6.4 Discussion

6.4.1 96 hours of directional stimulation caused minor changes to cell contractility

The significant changes in spontaneous cycle length observed during previous, multi-site experiments were absent in the directionally paced cells. This is consistent with the hypothesis that the changes in spontaneous cycle length seen previously were due to improper incubator function. Restoring the humidity of

the stage incubator resulted in a vastly decreased fluid loss (chapter 5) meaning the cells were no longer subjected to altered ion concentrations, preventing the increase in spontaneous rate.

Previously, contraction recordings in control cells in showed significant changes in contraction kinetics throughout the multi-site pacing period (Figure 4.8). Due to an artefact caused by photostimulation, contraction kinetics were measured on spontaneously active cells. As a result, kinetics were greatly affected by changes in spontaneous cycle length. With the addition of a longpass emission filter between the camera and cells, contraction recording and photostimulation could be performed simultaneously. With a consistent beating rate, the contraction kinetics of control cells did not change significantly throughout the directional pacing period (Figure 6.3).

The significant decrease in Up90 observed in directionally paced cells can therefore be attributed to the pacing protocol rather than a secondary effect of fluid loss and spontaneous rate. The increased speed of contraction likely represents faster Ca^{2+} release from the sarcoplasmic reticulum, consistent with a more mature Ca^{2+} handling system[166,186,187]. Alternatively, this could represent changes in internal resistive forces due to altered expression of sarcomeric proteins.

These findings should be verified using appropriate optical sensors, however they indicate that directional electrical activity can increase the functional maturity of iPSC-CMs.

6.4.2 96 hours of directional stimulation did not alter cell excitability

The adult cardiomyocyte has a significantly larger cell capacitance, due to the presence of T-tubules, along with a more negative resting membrane potential, and a greater upstroke velocity than iPSC-CMs[64,82]. If directional pacing caused changes in these functional parameters, they would be reflected in the strength-duration curve.

The slower upstroke velocity observed in iPSC-CMs can be attributed to lower expression of voltage gated sodium channels. As blockade of voltage gated

sodium channels shifts the strength-duration curve up and to the right[134,135,137], an increase in sodium channel density associated with maturation would be expected to produce a strength duration curve with a reduced chronaxie and rheobase. A lack of change in the strength duration curve (Figure 6.5) indicates that directional pacing did not induce significant changes in expression or activation of voltage gated ion channels.

The more negative membrane potential associated with maturity would require a larger stimulus current in order to reach threshold and would be reflected by an increased rheobase[188,189]. However, as ChR-2 rheobase is determined by the intensity of illumination and ChR-2 current amplitude displays strong inward rectification[108,109], membrane hyperpolarisation would be accompanied by an increased photocurrent amplitude, preventing an increase in rheobase and obscuring the effect of membrane potential. An increase in rheobase due to increased cell capacitance would not be affected by the inward rectification of ChR-2.

Taken alongside the absence of significant changes to spontaneous cycle-length (Figure 6.2), the absence of any changes to rheobase (Figure 6.5) indicates that directional pacing has not significantly altered the excitability of iPSC-CMs

6.4.3 96 hours of directional stimulation did not alter cell structure

The lack of changes to sarcomeric structure indicates that directional electrical activity alone is insufficient to significantly alter iPSC-CM structure. This is at odds with several studies that have shown that electrical stimulation can influence sarcomeric structure[48,148]. The most likely explanation for this inconsistency the longer time courses used in these studies (5 days – 4 weeks). Given the 50% duty cycle used in this project, each well is stimulated for only 48 out of the 96-hour pacing protocol. Increasing the duration of the stimulation protocol may increase the effect of directional stimulation on cell structure. Additionally, replicating the directional contraction axis of the developing heart in addition to the directional electrical axis may promote structural changes in these cells.

6.4.4 Conclusions

Directional pacing can modestly improve contractile function in iPSC-CMs, but could be improved by prolonging the stimulation protocol and supplementing with additional structural factors

Chapter 7: General discussion

7.1 Background

The aim of this project was to determine if the structure and function of commercially available iPSC-CMs could be altered by replicating the electrical activity of the developing heart.

As stated in chapter 1, the developing heart consists of a muscularised tube with peristaltic contractions[9]. Because of their value as a diagnostic tool[92,97] this project aimed to improve the maturity of iPSC-CMs using optogenetic stimulation to mimic the directional electrical activity observed during development. Cell contractility, spontaneous activity and sarcomere structure were used as indicators of cell maturity as these parameters best represent the contrast between mature and immature cells[50,63,64].

7.2 Major findings

7.2.1 Distribution of contractility parameters

Using baseline spontaneous recordings gathered throughout the course of this project several histograms were generated showing the distribution of the contractility parameters (Figure 2.5). The spontaneous cycle length of cells did not conform to a gaussian distribution with the majority of cells having a beating rate between 0.5 and 3 Hz. As contraction kinetics are heavily influenced by contraction frequency, the kinetics of spontaneously beating cells were also non-normally distributed.

7.2.2 Success of viral transfer

Viral transfection (at MOIs of 2,500 and above) was successful and allowed for full control of cell beating rate at 5 days post-transfection. Although high, transfection with an MOI of 2,500 showed no negative effects such as loss of cell viability or death in the week following transfection.

7.2.3 Comparison of optogenetic and field stimulation

Published literature has shown the chronaxie of ChR-2 based optogenetic stimulation is greater than that of cathodal stimulation[140,142-146]. Chronaxie is a

useful metric for comparing the excitability of various tissues, however it can be heavily influenced by stimulus waveform amongst other factors. The inverse strength-duration relationship ($I_t = {}^{1}/_{t}$) assumes a constant current pulse. For non-constant current pulses (such as a capacitor discharge) chronaxie is significantly greater[190]. This is particularly relevant to optical chronaxie measurements as ChR-2 does not produce a constant photocurrent. An initial peak decays exponentially to a steady state with a decay constant of around 23 ms[191] or 7 ms for the gain of function mutant (H134R)[109], meaning current injection at shorter pulse-widths is similar to that of a capacitor discharge. Confounding this is the strong inward rectification of ChR-2[109,192] resulting in a reduced current amplitude as the membrane potential reaches positive values. These waveform differences are likely the cause of the significant differences between optogenetic and electrical stimulation reported in literature.

In this project, ChR-2 and electric field stimulation were not significantly different. This inconsistency with published literature could be a consequence of the spontaneous activity present in these cells. The threshold currents recorded were not the threshold for action potential generation, but the current required to completely override the spontaneous rate of the cells. It is likely that ChR-2 photocurrent works in concert with other depolarising currents, decreasing the photocurrent required to reach threshold and altering the position of the strength duration curve.

7.2.4 Issues with prolonged photostimulation dictated protocol for long term photostimulation experiments

Initial experiments suggested a significant toxic effect of prolonged photostimulation. Loss of photostimulation:contraction coupling was observed after only a few hours and cell death occurred within the photostimulation area after 24 hours. A thorough investigation revealed that toxicity was not caused by 470 nm illumination, but rather overactivity of paced cells. The proposed mechanism posits that increased Ca^{2+} entry via the L-type Ca^{2+} channel overwhelms the immature Ca^{2+} handling apparatus of the iPSC-CM leading to an increase in diastolic Ca^{2+} levels. This would cause an increased contraction duration and an increase in resting membrane potential resulting the observed loss of coupling via slow inactivation of voltage gated sodium channels. The

observed reduction in viable cell area can be attributed to the increased diastolic Ca^{2+} levels causing activation of apoptotic pathways[182].

Although not as large, transfected unstimulated cells showed changes in contractility similar to that seen in transfected, stimulated cells after 24 hours. ChR-2 is activated by light at the short end of the visible spectrum (Figure 2.6) meaning the brightfield illumination used to facilitate repeated recordings would cause channel opening. Although clearly below the threshold for action potential generation, continuous Ca^{2+} entry would result in an increased contraction duration and spontaneous cycle length.

The use of a multi-site pacing protocol limits the exposure of each photostimulation site. Using this method, cells were successfully paced at 3 Hz for 96 hours. This method does however have some limitations. Currently the protocol uses 6 sites in each well, alternating between wells, leading to a duty cycle of 50% i.e. each well is only being paced 50% of the time. Several attempts were made to increase the duty cycle to 100% by only moving the stimulation between 6 sites within the same well. This however also resulted in loss of coupling and cell death at the stimulation sites.

Initial pacing experiments also highlighted a malfunction within the stage-top incubator. Changes in spontaneous cycle length in multi-site stimulated cells were mimicked in control cells (Chapter 4). Further experiments revealed that the humidity was not being adequately controlled (Figure 5.5). Although this inadequacy was corrected, a significant but temporary change in spontaneous cycle length was detected in control cells within the directional pacing study (Figure 6.3). Given the transient nature of this change, it is unlikely to be a consequence of cell aging. As such, it is likely that even with the improvements made, the stage-top incubator (an open-ended system) may not be sufficient for extended duration experiments. Future experiments should be adapted to utilise a closed system.

7.2.5 Directional vs non-directional photostimulation.

Non-directional photostimulation caused significant sarcomeric shortening (Figure 4.11). alongside a temporary change in spontaneous cycle length (Figure

4.7). These changes were not observed in directionally paced cells indicating that the malfunctioning stage-top incubator may have been responsible for these changes.

Directionally paced cells did however show a significant decrease in Up90 (Figure 6.2). By removing compounding factors such as improper incubator function, and variable spontaneous activity it can be concluded that this effect was a direct result of the directional pacing protocol. A decreased upstroke time could indicate a faster release of calcium from the sarcoplasmic reticulum, a functional change that is associated with an increase in maturity[166,186,187].

7.3 Comparison of results with existing literature

A recent study reported great success in generating adult-like human myocardium from iPSC-CMs[185]. Using field stimulation and flexible pillars to induce auxotonic contraction, they were able to simulate intensity training in heart tissues engineered from three iPS cell lines. Intensity training (2 weeks at a frequency increasing from 2 Hz to 6 Hz by 0.33 Hz per day, followed by a week at 2 Hz) proved highly effective when applied to early stage cardiomyocytes (immediately following the onset of spontaneous activity). Intensity treated cells displayed a positive force frequency relationship similar to adult cardiomyocytes, along with a contractile force that was greater than the constant frequency (2 Hz for 3 weeks) and control groups but less than the adult myocardium. Concomitant with these changes in contraction was an increased expression of Ca^{2+} handling proteins, and an increased responsiveness to caffeine, isoproterenol and thapsigargin. Increased sarcomere alignment, a sarcomere length similar to adult myocardium, and the presence of t-tubules high colocalization of L-type Ca^{2+} channels to RyR2 were further evidence of the increased maturity of these cells. Whilst still below the levels found in adult cells, early stage intensity trained cells also displayed an increase in I_{k1}, lack of which is thought to contribute to the spontaneous activity of iPSC-CMs. Other maturation techniques are described in Table 7.1.

The improvement to cell contractility in this project seems modest by comparison, however it is likely that it could be enhanced by incorporating several elements of the intensity training regime. The cells used in this project

were commercially available iPSC-CMs that were pre-matured before shipment. As such the plasticity of these cells is likely to be reduced. If the directional pacing protocol were to be implemented in early-stage iPSC-CMs it is likely that the effectiveness could be increased. Additionally, replicating the mechanical environment of the developed heart, either through auxotonic contractions[185], cyclic stretching[52,193] or increased substrate stiffness, could enhance the effects of directional pacing.

The toxicity of prolonged ChR-2 stimulation shown in chapter 5 is consistent with recent studies[182]. Pulsed 473 nm illumination over 3 days produced a strong apoptotic effect in melanoma cells expressing the D156A ChR-2 variant but had no effect in non-expressing cells. ChR-2(D156A) produced a decrease in mitochondrial transmembrane potential and increased caspase-3 production consistent with mitochondrial Ca^{2+} overload induced by Ca^{2+} ionophore. Lack of any significant changes in illuminated, non-expressing cells agrees with the findings of this project.

Table 7.1 Maturation methods and effects

Intervention type	Intervention	Effect
Mechanical	*Increased substrate stiffness*	Increased sarcomere length, increased Ca^{2+} transient amplitude, increased contractile force (NRVM)[157,194].
	Cyclic stretching	Increased Cx43 expression (hESC-CM)[56] and localisation (NRVM)[53], increased sarcomeric organisation (hESC-CM)[55], increased expression of cardiac specific ion channels (hESC-CM)[56].
	Topographical cues	Reduced circularity, increased sarcomere alignment (NRVM)[195,196], movement of Cx43 to periphery(hESC-CM)[57] (NRVM)[197]

Table 7.2 Maturation methods and effects (continued)

Intervention type	Intervention	Effect
Mechanical	*Dynamic culture*	Increased expression of α-actinin and cardiac troponin, increased contractile force, increased Ca^{2+} transient amplitude, increased conduction velocity (NRVM/hiPSC)[198].
Electrical	*72 hrs 5 Hz field stimulation*	Increased mitochondrial activity (NRVM)[199].
	5 days 1 Hz field stimulation	Decreased excitation threshold, increased fractional shortening, increased sarcomeric organisation (NRVM)[48].
	7 days 0.5-2 Hz field stimulation	Increased sarcomeric organisation(2 Hz), adaptation of spontaneous rate to stimulation rate (0.5-2 Hz), increased expression of hERG(2 Hz) (hESC-CM)[148].
	4 weeks 0.5-2 Hz Field stimulation	Increased contractile force, increased sarcomere density (NRVM/hiPSC-CM)[51].
Combined	*Biowire*	Increased sarcomere organisation, reduced threshold potential, increased conduction velocity, improved Ca^{2+} handling, increased hERG and I_{K1} current density (hiPSC)[200].

Table 7.3 Maturation methods and effects (continued)

Intervention type	Intervention	Effect
Combined	*Intensity training*	Adult sarcomere length, positive force frequency relationship, increased Ca^{2+} transient amplitude, increased contractile force, increased t-tubule density, increased colocalization of Ca^{2+} handling proteins, increased SR capacity and responsiveness, increased I_{K1} current density (hiPSC-CM)[185].
	Cyclic stretch with β-adrenergic stimulation	Increased contractile force, increased expression of β-MHC (NRVM)[201].
	Cyclic stretch and electrical stimulation	Increased contractile force, increased contraction and relaxation speed, increased SERCA2a expression (NRVM)[61]
	Topographical and electrical	Cell elongation, movement of Cx43 to periphery (NRVM)[202].

7.4 Future studies

As shown in chapters 2 and 3, channelrhodopsin based photostimulation is incompatible with the optical sensors for voltage and calcium used in house (Di-4-anepps and Fura-2). Although unavailable for this project there are alternative, more compatible techniques, available to allow more detailed study of cellular electrophysiology in any future photostimulation studies. The red-shifted voltage sensitive dye di-4-ANBDQPQ has been shown to allow simultaneous photostimulation and voltage recordings[147]. Alongside this, red-shifted fluorescent probes(such as Cal-630) and genetically encoded calcium

indicators (GECI) have become available allowing for calcium measurements to be made alongside photostimulation[203]. This would allow several of the hypotheses proposed during this project to be tested.

Although MUSCLEMOTION gives many useful characteristics of cardiac contractility it does not give any indication of contractile force, a major difference between adult cardiomyocytes and iPSC-CMs[75,76]. Future experiments should attempt to determine if there is a corresponding increase in contractile force alongside the decreased contraction time.

In addition to a more detailed investigation of excitation contraction coupling, future experiments should look to determine the extent of action potential propagation during directional stimulation. This could be achieved with optical mapping using a macroscope coupled and an appropriate voltage sensitive dye[147]. Alternatively, microelectrode arrays (MEA) have been used successfully to map changes in field potential in a monolayer of iPSC-CMs in response to optogenetic stimulation[204].

Finally, the multisite pacing protocol could be altered to include additional sites in each well. This would limit the exposure of each site and may allow for a single iPSC-CM monolayer to be paced with a 100% duty cycle.

7.5 Final remarks

This project has demonstrated that replicating the directional electrical activity of the developing heart can induce a modest increase in the functional maturity of commercially available iPSC-CMs.

Appendix

Python code created to automatically calculate excitability markers from strength duration curves. Briefly: signal generator voltage is converted into optical power before being plotted against pulse width. A 2nd order best fitting exponential is then plotted and the rheobase taken as the minimum y value. The chronaxie is taken as the x value associated with a y value twice that of the rheobase value. If no exact chronaxie could be determined, the x value associated with the median of a list of y values between 1.9-2.1*rheobase was taken as chronaxie. Chronaxie and rheobase values can then be saved in a CSV file. (Python 2.7.13)

```
#import pandas as pd
import matplotlib.pyplot as plt
from scipy.optimize import curve_fit
import numpy as np
#import sys


pulse = []
Optical_power =[]


#returns median of a list of chronaxies
def median(lst):
    sortedLst = sorted(lst)
    lstLen = len(lst)
    index = (lstLen - 1) // 2

    if (lstLen % 2):
        return sortedLst[index]
    else:
        return (sortedLst[index] + sortedLst[index + 1])/2.0


#Convert amplifier voltage to optical power
def Convert(voltage):
    z = ((201.62389*float(voltage)-7.29275)/1000)/0.246
    return z


print "How many values?"
No_data = int(raw_input())

print "Enter pulse widths"
for i in range(0,No_data):
    x = float(raw_input())
    pulse.append(x)

print "Enter voltages"
for i in range(0,No_data):
    voltage = float(raw_input())
    y = Convert(float(voltage))
    Optical_power.append(y)

plt.plot (pulse, Optical_power, 'ro')

x=np.array(pulse)
```

```
y=np.array(Optical_power)

def func(x, a1, t1, a2, t2, c):
    #return c*(1/x) # simple inverse
    #return b*(1+c/x) #Lapiqcue inverse
    #return b/(1-np.exp(-x/t1)) # Lapiqcue exponential decay
    return a1 * np.exp(-x/t1) + a2*np.exp(-x/t2)+ c #second order exponential

#popt = an array of Optimal values for the parameters so that
#the sum of the squared residuals of func(x, *popt) - y is minimized

#pcov = The estimated covariance of popt.

popt, pcov = curve_fit(func, x, y,maxfev=100000)

#Generate x axis for line of best fit
xx = np.linspace((pulse[0]-0.05),pulse[-1],10000)

#generate y axis for line of best fit
yy = func(xx,*popt)

#plot line of best fit
lines = plt.plot(xx, yy, 'r-', label='fit')

#generate R2 value

residuals = y- func(x, *popt)
ss_res = np.sum(residuals**2) #residual sum of squares
ss_tot = np.sum((y-np.mean(y))**2) #total sum of squares
r_squared = 1 - (ss_res / ss_tot)

plt.xlabel('Pulse width (ms)')
plt.ylabel('Optical Power (mW/mm2)')
plt.legend()
plt.show()


rheobase = yy[-1:]
chronaxies = []

for x in xx:
    z = np.where(xx==x)
    if yy[z]==(rheobase*2):
        chronaxie =x
        break
    #if no exact match, make list of values around chronaxie
    elif yy[z]>=(rheobase*1.9) and yy[z]<=(rheobase*2.1):
        chronaxies.append(x)
       #print chronaxie
    else:
        chronaxie = 0

#identify chronaxie as the median value of the list of chronaxies
if chronaxie == 0:
    chronaxie = median(chronaxies)


rheobase = str(rheobase)[2:-1]

print "Rheobase: "+str(rheobase)[0:-4]+" mW/mm2"
print "Chronaxie: "+str(chronaxie)[0:-6]+"ms"
print "R_squared: "+str(r_squared)[0:5]

root='C:/Users/User/Documents/Thesis/Strength duration curves/'

print "Do you want to save these results?"
answer = raw_input()

if answer == "yes" or answer == "y":
    file = open(root+"electric 2nd order.csv",'a')
```

```
117.     file.write("Rheobase," + str(rheobase)[0:4] +
118.                ",Chronaxie," + str(chronaxie)[0:-6]+",\n")
119.     file.close()
120.
121. #store variables for next run to check for errors
122. mem_chronaxie=chronaxie
123. mem_rheobase=rheobase
124. mem_chronaxies = chronaxies
125. #reset variables
126. chronaxies = []
127. chronaxie = 0
128. rheobase = 0
```

List of references

1. Murry CE, Reinecke H, Pabon LM. Regeneration GapsObservations on Stem Cells and Cardiac Repair. *Journal of the American College of Cardiology* 2006; **47**(9): 1777-85.
2. Go AS, Mozaffarian D, Roger VL, et al. Heart disease and stroke statistics--2014 update: a report from the American Heart Association. *Circulation* 2014; **129**(3): e28.
3. Bahrami H, Kronmal R, Bluemke DA, et al. Differences in the Incidence of Congestive Heart Failure by Ethnicity: The Multi-Ethnic Study of Atherosclerosis. *Archives of internal medicine* 2008; **168**(19): 2138-45.
4. MacDonald JS, Robertson RT. Toxicity Testing in the 21st Century: A View from the Pharmaceutical Industry. *Toxicological Sciences* 2009; **110**(1): 40-6.
5. Furtado MB, Solloway MJ, Jones VJ, et al. BMP/SMAD1 signaling sets a threshold for the left/right pathway in lateral plate mesoderm and limits availability of SMAD4. *Genes & Development* 2008; **22**(21): 3037-49.
6. Tian Y, Yuan L, Goss AM, et al. Characterization and In Vivo Pharmacological Rescue of a Wnt2-Gata6 Pathway Required for Cardiac Inflow Tract Development. *Developmental Cell* 2010; **18**(2): 275-87.
7. Zhang H, Bradley A. Mice deficient for BMP2 are nonviable and have defects in amnion/chorion and cardiac development. *Development* 1996; **122**(10): 2977-86.
8. Mommersteeg MTM, Domínguez JN, Wiese C, et al. The sinus venosus progenitors separate and diversify from the first and second heart fields early in development. *Cardiovascular Research* 2010; **87**(1): 92-101.
9. de Jong F, Opthof T, Wilde AA, et al. Persisting zones of slow impulse conduction in developing chicken hearts. *Circulation Research* 1992; **71**(2): 240.
10. Eichna LW, Dehaan RL. Differentiation of the Atrioventricular Conducting System of the Heart. *Circulation* 1961; **24**(2): 458-70.
11. Mommersteeg MTM, Hoogaars WMH, Prall OWJ, et al. Molecular Pathway for the Localized Formation of the Sinoatrial Node. *Circulation Research* 2007; **100**(3): 354-62.
12. Paff GH, Boucek RJ, Harrell TC. Observations on the development of the electrocardiogram. *The Anatomical Record* 1968; **160**(3): 575-81.
13. Garg V, Kathiriya IS, Barnes R, et al. GATA4 mutations cause human congenital heart defects and reveal an interaction with TBX5. *Nature* 2003; **424**(6947): 443-7.
14. Schott J-J, Benson DW, Basson CT, et al. Congenital Heart Disease Caused by Mutations in the Transcription Factor NKX2-5. *Science* 1998; **281**(5373): 108-11.
15. Mori AD, Bruneau BG. TBX5 mutations and congenital heart disease: Holt-Oram syndrome revealed. *Current Opinion in Cardiology* 2004; **19**(3).
16. Harrelson Z, Kelly RG, Goldin SN, et al. Tbx2 is essential for patterning the atrioventricular canal and for morphogenesis of the outflow tract during heart development. *Development* 2004; **131**(20): 5041-52.
17. Ma L, Lu M-F, Schwartz RJ, Martin JF. Bmp2 is essential for cardiac cushion epithelial-mesenchymal transition and myocardial patterning. *Development* 2005; **132**(24): 5601-11.
18. Van Mierop LHS, Gessner IH. The morphologic development of the sinoatrial node in the mouse. *The American Journal of Cardiology* 1970; **25**(2): 204-12.
19. Davies MP, An RH, Doevendans P, Kubalak S, Chien KR, Kass RS. Developmental Changes in Ionic Channel Activity in the Embryonic Murine Heart. *Circulation Research* 1996; **78**(1): 15-25.
20. Zhao Y, Samal E, Srivastava D. Serum response factor regulates a muscle-specific microRNA that targets Hand2 during cardiogenesis. *Nature* 2005; **436**(7048): 214-20.
21. Bers DM. Cardiac excitation-contraction coupling. *Nature* 2002; **415**(6868): 198-205.
22. Seki S, Nagashima M, Yamada Y, et al. Fetal and postnatal development of Ca^{2+} transients and Ca^{2+} sparks in rat cardiomyocytes. *Cardiovascular Research* 2003; **58**(3): 535-48.
23. Nakanishi T, Seguchi M, Takao A. Development of the myocardial contractile system. *Experientia* 1988; **44**(11-12): 936-44.
24. Mahony L, Jones LR. Developmental changes in cardiac sarcoplasmic reticulum in sheep. *Journal of Biological Chemistry* 1986; **261**(32): 15257-65.

25. Pegg W, Michalak M. Differentiation of sarcoplasmic reticulum during cardiac myogenesis. *American Journal of Physiology - Heart and Circulatory Physiology* 1987; **252**(1): H22-H31.
26. Masuda H, Sumii K, Sperelakis N. Long openings of calcium channels in fetal rat ventricular cardiomyocytes. *Pflügers Archiv* 1995; **429**(4): 595-7.
27. Artman M, Ichikawa H, Avkiran M, Coetzee WA. Na+/Ca^{2+} exchange current density in cardiac myocytes from rabbits and guinea pigs during postnatal development. *American Journal of Physiology-Heart and Circulatory Physiology* 1995; **37**(4): H1714.
28. Qu Y, Ghatpande A, El-Sherif N, Boutjdir M. Gene expression of Na+/Ca^{2+} exchanger during development in human heart. *Cardiovascular Research* 2000; **45**(4): 866-73.
29. Wiegerinck RF, Cojoc A, Zeidenweber CM, et al. Force Frequency Relationship of the Human Ventricle Increases During Early Postnatal Development. *Pediatric Research* 2009; **65**: 414.
30. Cernohorský J, Kolář F, Pelouch V, Korecky B, Vetter R. Thyroid control of sarcolemmal Na+/Ca^{2+}exchanger and SR Ca^{2+}-ATPase in developing rat heart. *American Journal of Physiology - Heart and Circulatory Physiology* 1998; **275**(1): H264-H73.
31. Lopez L, Shacklock PS, Balke CW, Wier WG. Local calcium transients triggered by single L-type calcium channel currents in cardiac cells. *Science* 1995; **268**(5213): 1042-5.
32. Ziman AP, Gómez-Viquez NL, Bloch RJ, Lederer WJ. Excitation–contraction coupling changes during postnatal cardiac development. *Journal of Molecular and Cellular Cardiology* 2010; **48**(2): 379-86.
33. Gasser RF, Cork RJ, Stillwell BJ, McWilliams DT. Rebirth of Human Embryology. *Developmental dynamics : an official publication of the American Association of Anatomists* 2014; **243**(5): 621-8.
34. Li F, Wang X, Capasso JM, Gerdes AM. Rapid Transition of Cardiac Myocytes from Hyperplasia to Hypertrophy During Postnatal Development. *Journal of Molecular and Cellular Cardiology* 1996; **28**(8): 1737-46.
35. Hohendanner F, McCulloch AD, Blatter LA, Michailova AP. Calcium and IP3 dynamics in cardiac myocytes: experimental and computational perspectives and approaches. *Frontiers in Pharmacology* 2014; **5**: 35.
36. Contreras-Ferrat AE, Toro B, Bravo R, et al. An Inositol 1,4,5-Triphosphate (IP3)-IP3 Receptor Pathway Is Required for Insulin-Stimulated Glucose Transporter 4 Translocation and Glucose Uptake in Cardiomyocytes. *Endocrinology* 2010; **151**(10): 4665-77.
37. Yu J, Deliu E, Zhang X-Q, et al. Differential Activation of Cultured Neonatal Cardiomyocytes by Plasmalemmal Versus Intracellular G Protein-coupled Receptor 55. *The Journal of Biological Chemistry* 2013; **288**(31): 22481-92.
38. Richards MA, Clarke JD, Saravanan P, et al. Transverse tubules are a common feature in large mammalian atrial myocytes including human. *American Journal of Physiology - Heart and Circulatory Physiology* 2011; **301**(5): H1996-H2005.
39. Takahashi K, Yamanaka S. Induction of Pluripotent Stem Cells from Mouse Embryonic and Adult Fibroblast Cultures by Defined Factors. *Cell* 2006; **126**(4): 663-76.
40. Takahashi K, Tanabe K, Ohnuki M, et al. Induction of Pluripotent Stem Cells from Adult Human Fibroblasts by Defined Factors. *Cell* 2007; **131**(5): 861-72.
41. Kattman SJ, Witty AD, Gagliardi M, et al. Stage-Specific Optimization of Activin/Nodal and BMP Signaling Promotes Cardiac Differentiation of Mouse and Human Pluripotent Stem Cell Lines. *Cell stem cell* 2011; **8**(2): 228-40.
42. Willems E, Spiering S, Davidovics H, et al. Small-Molecule Inhibitors of the Wnt Pathway Potently Promote Cardiomyocytes From Human Embryonic Stem Cell–Derived Mesoderm. *Circulation Research* 2011; **109**(4): 360-4.
43. Chattergoon NN, Giraud GD, Louey S, Stork P, Fowden AL, Thornburg KL. Thyroid hormone drives fetal cardiomyocyte maturation. *The FASEB Journal* 2012; **26**(1): 397-408.
44. Lee Y-K, Ng K-M, Chan Y-C, et al. Triiodothyronine Promotes Cardiac Differentiation and Maturation of Embryonic Stem Cells via the Classical Genomic Pathway. *Molecular Endocrinology* 2010; **24**(9): 1728-36.

45. Yang X, Rodriguez M, Pabon L, et al. Tri-iodo-l-thyronine promotes the maturation of human cardiomyocytes-derived from induced pluripotent stem cells. *Journal of Molecular and Cellular Cardiology* 2014; **72**(0): 296-304.
46. Fu J-D, Rushing SN, Lieu DK, et al. Distinct Roles of MicroRNA-1 and -499 in Ventricular Specification and Functional Maturation of Human Embryonic Stem Cell-Derived Cardiomyocytes. *PLoS ONE* 2011; **6**(11): e27417.
47. Serena E, Figallo E, Tandon N, et al. Electrical stimulation of human embryonic stem cells: Cardiac differentiation and the generation of reactive oxygen species. *Experimental Cell Research* 2009; **315**(20): 3611-9.
48. Radisic M, Park H, Shing H, et al. Functional assembly of engineered myocardium by electrical stimulation of cardiac myocytes cultured on scaffolds. *Proceedings of the National Academy of Sciences* 2004; **101**(52): 18129-34.
49. Sathaye A, Bursac N, Sheehy S, Tung L. Electrical pacing counteracts intrinsic shortening of action potential duration of neonatal rat ventricular cells in culture. *Journal of Molecular and Cellular Cardiology* 2006; **41**(4): 633-41.
50. Chan Y-C, Ting S, Lee Y-K, et al. Electrical Stimulation Promotes Maturation of Cardiomyocytes Derived from Human Embryonic Stem Cells. *Journal of Cardiovascular Translational Research* 2013; **6**(6): 989-99.
51. Hirt MN, Boeddinghaus J, Mitchell A, et al. Functional improvement and maturation of rat and human engineered heart tissue by chronic electrical stimulation. *Journal of Molecular and Cellular Cardiology* 2014; **74**(0): 151-61.
52. Zimmermann WH, Schneiderbanger K, Schubert P, et al. Tissue Engineering of a Differentiated Cardiac Muscle Construct. *Circulation Research* 2002; **90**(2): 223-30.
53. Salameh A, Wustmann A, Karl S, et al. Cyclic Mechanical Stretch Induces Cardiomyocyte Orientation and Polarization of the Gap Junction Protein Connexin43. *Circulation Research* 2010; **106**(10): 1592-602.
54. Gwak S-J, Bhang SH, Kim I-K, et al. The effect of cyclic strain on embryonic stem cell-derived cardiomyocytes. *Biomaterials* 2008; **29**(7): 844-56.
55. Földes G, Mioulane M, Wright JS, et al. Modulation of human embryonic stem cell-derived cardiomyocyte growth: A testbed for studying human cardiac hypertrophy? *Journal of Molecular and Cellular Cardiology* 2011; **50**(2): 367-76.
56. Mihic A, Li J, Miyagi Y, et al. The effect of cyclic stretch on maturation and 3D tissue formation of human embryonic stem cell-derived cardiomyocytes. *Biomaterials* 2014; **35**(9): 2798-808.
57. Salick MR, Napiwocki BN, Sha J, et al. Micropattern width dependent sarcomere development in human ESC-derived cardiomyocytes. *Biomaterials* 2014; **35**(15): 4454-64.
58. Annabi N, Tsang K, Mithieux SM, et al. Highly Elastic Micropatterned Hydrogel for Engineering Functional Cardiac Tissue. *Advanced Functional Materials* 2013; **23**(39): 4950-9.
59. Liau B, Christoforou N, Leong KW, Bursac N. Pluripotent stem cell-derived cardiac tissue patch with advanced structure and function. *Biomaterials* 2011; **32**(35): 9180-7.
60. Christoforou N, Liau B, Chakraborty S, Chellapan M, Bursac N, Leong KW. Induced Pluripotent Stem Cell-Derived Cardiac Progenitors Differentiate to Cardiomyocytes and Form Biosynthetic Tissues. *PLoS ONE* 2013; **8**(6): e65963.
61. Morgan KY, Black LD. Mimicking Isovolumic Contraction with Combined Electromechanical Stimulation Improves the Development of Engineered Cardiac Constructs. *Tissue Engineering Part A* 2014; **20**(11-12): 1654-67.
62. Park H, Larson BL, Kolewe ME, Vunjak-Novakovic G, Freed LE. Biomimetic scaffold combined with electrical stimulation and growth factor promotes tissue engineered cardiac development. *Experimental Cell Research* 2014; **321**(2): 297-306.
63. Snir M, Kehat I, Gepstein A, et al. Assessment of the ultrastructural and proliferative properties of human embryonic stem cell-derived cardiomyocytes. *American Journal of Physiology - Heart and Circulatory Physiology* 2003; **285**(6): H2355-H63.
64. Lundy SD, Zhu W-Z, Regnier M, Laflamme MA. Structural and Functional Maturation of Cardiomyocytes Derived from Human Pluripotent Stem Cells. *Stem Cells and Development* 2013; **22**(14): 1991-2002.

65. Kuzmenkin A, Liang H, Xu G, et al. Functional characterization of cardiomyocytes derived from murine induced pluripotent stem cells in vitro. *The FASEB Journal* 2009; **23**(12): 4168-80.
66. Cerbai E, Sartiani L, DePaoli P, et al. The Properties of the Pacemaker Current IFin Human Ventricular Myocytes are Modulated by Cardiac Disease. *Journal of Molecular and Cellular Cardiology* 2001; **33**(3): 441-8.
67. Gherghiceanu M, Barad L, Novak A, et al. Cardiomyocytes derived from human embryonic and induced pluripotent stem cells: comparative ultrastructure. *Journal of Cellular and Molecular Medicine* 2011; **15**(11): 2539-51.
68. Lieu DK, Liu J, Siu C-W, et al. Absence of Transverse Tubules Contributes to Non-Uniform Ca^{2+} Wavefronts in Mouse and Human Embryonic Stem Cell–Derived Cardiomyocytes. *Stem Cells and Development* 2009; **18**(10): 1493-500.
69. Satin J, Itzhaki I, Rapoport S, et al. Calcium Handling in Human Embryonic Stem Cell-Derived Cardiomyocytes. *STEM CELLS* 2008; **26**(8): 1961-72.
70. Synnergren J, Améen C, Jansson A, Sartipy P. Global transcriptional profiling reveals similarities and differences between human stem cell-derived cardiomyocyte clusters and heart tissue. *Physiological Genomics* 2012; **44**(4): 245-58.
71. Liu J, Fu JD, Siu CW, Li RA. Functional Sarcoplasmic Reticulum for Calcium Handling of Human Embryonic Stem Cell-Derived Cardiomyocytes: Insights for Driven Maturation. *STEM CELLS* 2007; **25**(12): 3038-44.
72. Dolnikov K, Shilkrut M, Zeevi-Levin N, et al. Functional Properties of Human Embryonic Stem Cell–Derived Cardiomyocytes: Intracellular Ca^{2+} Handling and the Role of Sarcoplasmic Reticulum in the Contraction. *STEM CELLS* 2006; **24**(2): 236-45.
73. Itzhaki I, Rapoport S, Huber I, et al. Calcium Handling in Human Induced Pluripotent Stem Cell Derived Cardiomyocytes. *PLoS ONE* 2011; **6**(4): e18037.
74. Germanguz I, Sedan O, Zeevi-Levin N, et al. Molecular characterization and functional properties of cardiomyocytes derived from human inducible pluripotent stem cells. *Journal of Cellular and Molecular Medicine* 2011; **15**(1): 38-51.
75. Kita-Matsuo H, Barcova M, Prigozhina N, et al. Lentiviral Vectors and Protocols for Creation of Stable hESC Lines for Fluorescent Tracking and Drug Resistance Selection of Cardiomyocytes. *PLoS ONE* 2009; **4**(4): e5046.
76. Korte FS, Herron TJ, Rovetto MJ, McDonald KS. Power output is linearly related to MyHC content in rat skinned myocytes and isolated working hearts. *American Journal of Physiology - Heart and Circulatory Physiology* 2005; **289**(2): H801-H12.
77. Wang Y, Li ZC, Zhang P, et al. Nitric Oxide-cGMP-PKG Pathway Acts on Orai1 to Inhibit the Hypertrophy of Human Embryonic Stem Cell-Derived Cardiomyocytes. *STEM CELLS* 2015; **33**(10): 2973-84.
78. Huang B, Wang W, Bates M, Zhuang X. Three-Dimensional Super-Resolution Imaging by Stochastic Optical Reconstruction Microscopy. *Science* 2008; **319**(5864): 810-3.
79. Kapur N, Banach K. Inositol-1,4,5-trisphosphate-mediated spontaneous activity in mouse embryonic stem cell-derived cardiomyocytes. *The Journal of Physiology* 2007; **581**(3): 1113-27.
80. Kolossov E, Lu Z, Drobinskaya I, et al. Identification and characterization of embryonic stem cell-derived pacemaker and atrial cardiomyocytes. *The FASEB Journal* 2005; **19**(6): 577-9.
81. Ivashchenko CY, Pipes GC, Lozinskaya IM, et al. Human-induced pluripotent stem cell-derived cardiomyocytes exhibit temporal changes in phenotype. *American Journal of Physiology - Heart and Circulatory Physiology* 2013; **305**(6): H913-H22.
82. Drouin E, Charpentier F, Gauthier C, Laurent K, Le Marec H. Electrophysiologic characteristics of cells spanning the left ventricular wall of human heart: Evidence for presence of M cells. *Journal of the American College of Cardiology* 1995; **26**(1): 185-92.
83. Mummery C, Ward D, Van Den Brink CE, et al. Cardiomyocyte differentiation of mouse and human embryonic stem cells*. *Journal of Anatomy* 2002; **200**(3): 233-42.
84. Sartiani L, Bettiol E, Stillitano F, Mugelli A, Cerbai E, Jaconi ME. Developmental Changes in Cardiomyocytes Differentiated from Human Embryonic Stem Cells: A Molecular and Electrophysiological Approach. *STEM CELLS* 2007; **25**(5): 1136-44.

85. Kehat I, Gepstein A, Spira A, Itskovitz-Eldor J, Gepstein L. High-Resolution Electrophysiological Assessment of Human Embryonic Stem Cell-Derived Cardiomyocytes: A Novel In Vitro Model for the Study of Conduction. *Circulation Research* 2002; **91**(8): 659-61.
86. Spach MS, Heidlage JF, Barr RC, Dolber PC. Cell size and communication: Role in structural and electrical development and remodeling of the heart. *Heart Rhythm* 2004; **1**(4): 500-15.
87. Caspi O, Huber I, Kehat I, et al. Transplantation of Human Embryonic Stem Cell-Derived Cardiomyocytes Improves Myocardial Performance in Infarcted Rat Hearts. *Journal of the American College of Cardiology* 2007; **50**(19): 1884-93.
88. Laflamme MA, Chen KY, Naumova AV, et al. Cardiomyocytes derived from human embryonic stem cells in pro-survival factors enhance function of infarcted rat hearts. *Nat Biotech* 2007; **25**(9): 1015-24.
89. Liao S-Y, Liu Y, Siu C-W, et al. Proarrhythmic risk of embryonic stem cell–derived cardiomyocyte transplantation in infarcted myocardium. *Heart Rhythm* 2010; **7**(12): 1852-9.
90. Shiba Y, Fernandes S, Zhu W-Z, et al. Human ES-cell-derived cardiomyocytes electrically couple and suppress arrhythmias in injured hearts. *Nature* 2012; **489**(7415): 322-5.
91. Chong JJH, Yang X, Don CW, et al. Human embryonic-stem-cell-derived cardiomyocytes regenerate non-human primate hearts. *Nature* 2014; **510**(7504): 273-7.
92. Moretti A, Bellin M, Welling A, et al. Patient-Specific Induced Pluripotent Stem-Cell Models for Long-QT Syndrome. *New England Journal of Medicine* 2010; **363**(15): 1397-409.
93. Jost N, Acsai K, Horváth B, et al. Contribution of I Kr and I K1 to ventricular repolarization in canine and human myocytes: is there any influence of action potential duration? *Basic Research in Cardiology* 2009; **104**(1): 33-41.
94. Ma J, Guo L, Fiene SJ, et al. High purity human-induced pluripotent stem cell-derived cardiomyocytes: electrophysiological properties of action potentials and ionic currents. *American Journal of Physiology - Heart and Circulatory Physiology* 2011; **301**(5): H2006-H17.
95. Sakakibara Y, Furukawa T, Singer DH, et al. Sodium current in isolated human ventricular myocytes. *American Journal of Physiology* 1993; **265**: H1301-H.
96. Pelzmann B, Schaffer P, Bernhart E, et al. L-type calcium current in human ventricular myocytes at a physiological temperature from children with tetralogy of Fallot. *Cardiovascular Research* 1998; **38**(2): 424-32.
97. Guo L, Abrams R, Babiarz JE, et al. Estimating the Risk of Drug-induced Proarrhythmia using Human Induced Pluripotent Stem Cell Derived Cardiomyocytes. *Toxicological Sciences* 2011.
98. Huh D, Matthews BD, Mammoto A, Montoya-Zavala M, Hsin HY, Ingber DE. Reconstituting Organ-Level Lung Functions on a Chip. *Science* 2010; **328**(5986): 1662.
99. Nupura SBaVMaSMaATaMGaMMaQLaYSZaSRSaG. A liver-on-a-chip platform with bioprinted hepatic spheroids. *Biofabrication* 2016; **8**(1): 014101.
100. Jang K-J, Mehr AP, Hamilton GA, et al. Human kidney proximal tubule-on-a-chip for drug transport and nephrotoxicity assessment. *Integrative Biology* 2013; **5**(9): 1119-29.
101. Zhang YS, Arneri A, Bersini S, et al. Bioprinting 3D microfibrous scaffolds for engineering endothelialized myocardium and heart-on-a-chip. *Biomaterials* 2016; **110**: 45-59.
102. Geddes LA. Accuracy limitations of chronaxie values. *IEEE Transactions on Biomedical Engineering* 2004; **51**(1): 176-81.
103. Zemelman BV, Lee GA, Ng M, Miesenböck G. Selective Photostimulation of Genetically ChARGed Neurons. *Neuron* 2002; **33**(1): 15-22.
104. Mutoh H, Perron A, Akemann W, Iwamoto Y, Knöpfel T. Optogenetic monitoring of membrane potentials. *Experimental Physiology* 2011; **96**(1): 13-8.
105. Chang Liao M-L, de Boer TP, Mutoh H, et al. Sensing Cardiac Electrical Activity With a Cardiac Myocyte–Targeted Optogenetic Voltage Indicator. *Circulation Research* 2015; **117**(5): 401.
106. Akerboom J, Carreras Calderón N, Tian L, et al. Genetically encoded calcium indicators for multi-color neural activity imaging and combination with optogenetics. *Frontiers in Molecular Neuroscience* 2013; **6**: 2.
107. Zhao S, Cunha C, Zhang F, et al. Improved expression of halorhodopsin for light-induced silencing of neuronal activity. *Brain Cell Biology* 2008; **36**(1): 141-54.

108. Nagel G, Szellas T, Huhn W, et al. Channelrhodopsin-2, a directly light-gated cation-selective membrane channel. *Proceedings of the National Academy of Sciences* 2003; **100**(24): 13940-5.
109. Nagel G, Brauner M, Liewald JF, Adeishvili N, Bamberg E, Gottschalk A. Light Activation of Channelrhodopsin-2 in Excitable Cells of Caenorhabditis elegans Triggers Rapid Behavioral Responses. *Current Biology* 2005; **15**(24): 2279-84.
110. Boyden ES, Zhang F, Bamberg E, Nagel G, Deisseroth K. Millisecond-timescale, genetically targeted optical control of neural activity. *Nat Neurosci* 2005; **8**(9): 1263-8.
111. Bamann C, Kirsch T, Nagel G, Bamberg E. Spectral Characteristics of the Photocycle of Channelrhodopsin-2 and Its Implication for Channel Function. *Journal of Molecular Biology* 2008; **375**(3): 686-94.
112. Cardin JA, Carlen M, Meletis K, et al. Targeted optogenetic stimulation and recording of neurons in vivo using cell-type-specific expression of Channelrhodopsin-2. *Nat Protocols* 2010; **5**(2): 247-54.
113. Arrenberg AB, Del Bene F, Baier H. Optical control of zebrafish behavior with halorhodopsin. *Proceedings of the National Academy of Sciences* 2009; **106**(42): 17968-73.
114. Prakash R, Yizhar O, Grewe B, et al. Two-photon optogenetic toolbox for fast inhibition, excitation and bistable modulation. *Nat Meth* 2012; **9**(12): 1171-9.
115. Zhang F, Wang L-P, Brauner M, et al. Multimodal fast optical interrogation of neural circuitry. *Nature* 2007; **446**(7136): 633-9.
116. Bruegmann T, Boyle PM, Vogt CC, et al. Optogenetic defibrillation terminates ventricular arrhythmia in mouse hearts and human simulations. *The Journal of Clinical Investigation*; **126**(10): 3894-904.
117. Burton RAB, Klimas A, Ambrosi CM, et al. Optical control of excitation waves in cardiac tissue. *Nat Photon* 2015; **9**(12): 813-6.
118. Marcus GM, Chan DW, Redberg RF. Recollection of Pain Due to Inappropriate Versus Appropriate Implantable Cardioverter-Defibrillator Shocks. *Pacing and Clinical Electrophysiology* 2011; **34**(3): 348-53.
119. Larsen GK, Evans J, Lambert WE, Chen Y, Raitt MH. Shocks burden and increased mortality in implantable cardioverter-defibrillator patients. *Heart Rhythm* 2011; **8**(12): 1881-6.
120. Sohail MR, Henrikson CA, Braid-Forbes M, Forbes KF, Lerner DJ. Mortality and cost associated with cardiovascular implantable electronic device infections. *Archives of Internal Medicine* 2011; **171**(20): 1821-8.
121. Tung L, Borderies JR. Analysis of electric field stimulation of single cardiac muscle cells. *Biophysical Journal* 1992; **63**(2): 371-86.
122. Sharma V, Tung L. Spatial heterogeneity of transmembrane potential responses of single guinea-pig cardiac cells during electric field stimulation. *The Journal of Physiology* 2004; **542**(2): 477-92.
123. Bruegmann T, Malan D, Hesse M, et al. Optogenetic control of heart muscle in vitro and in vivo. *Nat Meth* 2010; **7**(11): 897-900.
124. Wang H, Peca J, Matsuzaki M, et al. High-speed mapping of synaptic connectivity using photostimulation in Channelrhodopsin-2 transgenic mice. *Proceedings of the National Academy of Sciences* 2007; **104**(19): 8143.
125. Sala L, van Meer BJ, Tertoolen LT, et al. MUSCLEMOTION: A Versatile Open Software Tool to Quantify Cardiomyocyte and Cardiac Muscle Contraction In Vitro and In Vivo. *Circulation Research* 2017.
126. Kong SK, Lee CY. The use of fura 2 for measurement of free calcium concentration. *Biochemical Education* 1995; **23**(2): 97-8.
127. Lin JY, Lin MZ, Steinbach P, Tsien RY. Characterization of Engineered Channelrhodopsin Variants with Improved Properties and Kinetics. *Biophysical Journal* 2009; **96**(5): 1803-14.
128. Schindelin J, Arganda-Carreras I, Frise E, et al. Fiji: an open-source platform for biological-image analysis. *Nat Meth* 2012; **9**(7): 676-82.
129. Wagner E, Brandenburg S, ren, Kohl T, Lehnart SE. Analysis of Tubular Membrane Networks in Cardiac Myocytes from Atria and Ventricles. 2014; (92): e51823.

130. Weiwad WKK, Linke WA, Wussling MHP. Sarcomere Length–tension Relationship of Rat Cardiac Myocytes at Lengths Greater than Optimum. *Journal of Molecular and Cellular Cardiology* 2000; **32**(2): 247-59.
131. Becker N, Stoelzle S, Göpel S, et al. Minimized cell usage for stem cell-derived and primary cells on an automated patch clamp system. *Journal of Pharmacological and Toxicological Methods* 2013; **68**(1): 82-7.
132. Denning C, Borgdorff V, Crutchley J, et al. Cardiomyocytes from human pluripotent stem cells: From laboratory curiosity to industrial biomedical platform. *Biochimica et Biophysica Acta (BBA) - Molecular Cell Research* 2016; **1863**(7, Part B): 1728-48.
133. Kovács L, Szűcs G. Effect of caffeine on intramembrane charge movement and calcium transients in cut skeletal muscle fibres of the frog. *The Journal of Physiology* 1983; **341**(1): 559-78.
134. DiPalma JR, Mascatello AV. ANALYSIS OF THE ACTIONS OF ACETYLCHOLINE, ATROPINE, EPINEPHRINE AND QUINIDINE ON HEART MUSCLE OF THE CAT. *Journal of Pharmacology and Experimental Therapeutics* 1951; **101**(3): 243.
135. Wallace AG, Cline RE, Sealy WC, Young WG, Troyer WG. Electrophysiologic Effects of Quinidine. *Circulation Research* 1966; **19**(5): 960.
136. Tamargo J. Electrophysiological effects of bunaphtine on isolated rat atria. *European Journal of Pharmacology* 1980; **62**(1): 81-8.
137. Delgado C, Tamargo J, Tejerina T. Electrophysiological effects of propafenone in untreated and propafenone-pretreated guinea-pig atrial and ventricular muscle fibres. *British Journal of Pharmacology* 1985; **86**(4): 765-75.
138. Ashley Z, Sutherland H, Lanmuller H, et al. Determination of the Chronaxie and Rheobase of Denervated Limb Muscles in Conscious Rabbits. *Artificial Organs* 2005; **29**(3): 212-5.
139. Bruegmann T, van Bremen T, Vogt CC, Send T, Fleischmann BK, Sasse P. Optogenetic control of contractile function in skeletal muscle. *Nat Commun* 2015; **6**.
140. Vogt CC, Bruegmann T, Malan D, et al. Systemic gene transfer enables optogenetic pacing of mouse hearts. *Cardiovascular Research* 2015.
141. Lapicque L. Recherches quantitatives sur l'excitation electrique des nerfs traitee comme une polarization. *Journal de physiologie et de pathologie générale* 1907; **9**: 620-35.
142. Yu J, Chen K, Lucero RV, Ambrosi CM, Entcheva E. Cardiac Optogenetics: Enhancement by All-trans-Retinal. *Scientific Reports* 2015; **5**: 16542.
143. Stilli D, Lagrasta C, Berni R, et al. Preservation of ventricular performance at early stages of diabetic cardiomyopathy involves changes in myocyte size, number and intercellular coupling. *Basic Research in Cardiology* 2007; **102**(6): 488.
144. Tandon N, Marsano A, Maidhof R, Wan L, Park H, Vunjak-Novakovic G. Optimization of electrical stimulation parameters for cardiac tissue engineering. *Journal of Tissue Engineering and Regenerative Medicine* 2011; **5**(6): e115-e25.
145. Bassani RA, Lima KA, Gomes PA, Oliveira PX, Bassani JW. Combining stimulus direction and waveform for optimization of threshold stimulation of isolated ventricular myocytes. *Physiol Meas* 2006; **27**(9): 851-63.
146. Williams John C, Entcheva E. Optogenetic versus Electrical Stimulation of Human Cardiomyocytes: Modeling Insights. *Biophysical Journal* 2015; **108**(8): 1934-45.
147. Crocini C, Ferrantini C, Coppini R, et al. Optogenetics design of mechanistically-based stimulation patterns for cardiac defibrillation. *Scientific Reports* 2016; **6**: 35628.
148. Eng G, Lee BW, Protas L, et al. Autonomous beating rate adaptation in human stem cell-derived cardiomyocytes. *Nature Communications* 2016; **7**: 10312.
149. Morton SL, Daroux ML, Mortimer JT. The Role of Oxygen Reduction in Electrical Stimulation of Neural Tissue. *Journal of The Electrochemical Society* 1994; **141**(1): 122-30.
150. Wu S-Y, Hou H-S, Sun Y-S, Cheng J-Y, Lo K-Y. Correlation between cell migration and reactive oxygen species under electric field stimulation. *Biomicrofluidics* 2015; **9**(5): 054120.
151. Bett GCL, Kaplan AD, Lis A, et al. Electronic “expression” of the inward rectifier in cardiocytes derived from human-induced pluripotent stem cells. *Heart Rhythm*; **10**(12): 1903-10.
152. Goversen B, van der Heyden MAG, van Veen TAB, de Boer TP. The immature electrophysiological phenotype of iPSC-CMs still hampers in vitro drug screening: Special focus on IK1. *Pharmacology & Therapeutics* 2018; **183**: 127-36.

153. Bird SD, Doevendans PA, van Rooijen MA, et al. The human adult cardiomyocyte phenotype. *Cardiovascular Research* 2003; **58**(2): 423-34.
154. Bénardeau A, Hatem SN, Rücker-Martin C, et al. Primary Culture of Human Atrial Myocytes is Associated with the Appearance of Structural and Functional Characteristics of Immature Myocardium. *Journal of Molecular and Cellular Cardiology* 1997; **29**(5): 1307-20.
155. Prakash YS, Cody MJ, Housmans PR, Hannon JD, Sieck GC. Comparison of cross-bridge cycling kinetics in neonatal vs. adult rat ventricular muscle. *Journal of Muscle Research & Cell Motility* 1999; **20**(7): 717-23.
156. Jacot JG, Martin JC, Hunt DL. Mechanobiology of cardiomyocyte development. *Journal of Biomechanics* 2010; **43**(1): 93-8.
157. Rodriguez Anthony G, Han Sangyoon J, Regnier M, Sniadecki Nathan J. Substrate Stiffness Increases Twitch Power of Neonatal Cardiomyocytes in Correlation with Changes in Myofibril Structure and Intracellular Calcium. *Biophysical Journal* 2011; **101**(10): 2455-64.
158. ter Keurs HE, Rijnsburger WH, van Heuningen R, Nagelsmit MJ. Tension development and sarcomere length in rat cardiac trabeculae. Evidence of length-dependent activation. *Circulation Research* 1980; **46**(5): 703.
159. Daniels M, Noble MI, ter Keurs HE, Wohlfart B. Velocity of sarcomere shortening in rat cardiac muscle: relationship to force, sarcomere length, calcium and time. *The Journal of Physiology* 1984; **355**(1): 367-81.
160. de Tombe PP, ter Keurs HE. Force and velocity of sarcomere shortening in trabeculae from rat heart. Effects of temperature. *Circulation Research* 1990; **66**(5): 1239.
161. ter Keurs HEDJ, de Tombe PP. Determinants of Velocity of Sarcomere Shortening in Mammalian Myocardium. In: Sugi H, Pollack GH, eds. Mechanism of Myofilament Sliding in Muscle Contraction. Boston, MA: Springer US; 1993: 649-65.
162. Granzier H, Helmes M, Trombitás K. Nonuniform elasticity of titin in cardiac myocytes: a study using immunoelectron microscopy and cellular mechanics. *Biophysical Journal* 1996; **70**(1): 430-42.
163. Gallagher FA, Huang CLH. Osmotic 'detubulation' in frog muscle arises from a reversible vacuolation process. *Journal of Muscle Research & Cell Motility* 1997; **18**(3): 305-21.
164. Nakajima S, Nakajima Y, Peachey LD. Speed of repolarization and morphology of glycerol-treated frog muscle fibre. *The Journal of Physiology* 1973; **234**(2): 465-80.
165. Allen DG, Smith GL. The effects of hypertonicity on tension and intracellular calcium concentration in ferret ventricular muscle. *The Journal of Physiology* 1987; **383**(1): 425-39.
166. Lee Y-K, Ng K-M, Lai W-H, et al. Calcium Homeostasis in Human Induced Pluripotent Stem Cell-Derived Cardiomyocytes. *Stem Cell Reviews and Reports* 2011; **7**(4): 976-86.
167. Germanguz I, Sedan O, Zeevi-Levin N, et al. Molecular characterization and functional properties of cardiomyocytes derived from human inducible pluripotent stem cells. *Journal of Cellular and Molecular Medicine* 2011; **15**(1): 38-51.
168. Rink TJ, Tsien RY, Pozzan T. Cytoplasmic pH and free Mg^{2+} in lymphocytes. *The Journal of Cell Biology* 1982; **95**(1): 189.
169. Li HG, Jones DL, Yee R, Klein GJ. Electrophysiologic substrate associated with pacing-induced heart failure in dogs: Potential value of programmed stimulation in predicting sudden death. *Journal of the American College of Cardiology* 1992; **19**(2): 444-9.
170. Robboy SJ, Harthorne JW, Leinbach RC, Sanders CA, Austen WG. Autopsy Findings with Permanent Pervenous Pacemakers. *Circulation* 1969; **39**(4): 495.
171. Esposito M, Kennergren C, Holmström N, Nilsson S, Eckerdal J, Thomsen P. Morphologic and immunohistochemical observations of tissues surrounding retrieved transvenous pacemaker leads. *Journal of Biomedical Materials Research* 2002; **63**(5): 548-58.
172. Radovsky AS, Van Vleet JF. Effects of dexamethasone elution on tissue reaction around stimulating electrodes of endocardial pacing leads in dogs. *American Heart Journal* 1989; **117**(6): 1288-98.
173. Merrill DR, Bikson M, Jefferys JGR. Electrical stimulation of excitable tissue: design of efficacious and safe protocols. *Journal of Neuroscience Methods* 2005; **141**(2): 171-98.
174. Hawkins CL, Davies MJ. Generation and propagation of radical reactions on proteins. *Biochimica et Biophysica Acta (BBA) - Bioenergetics* 2001; **1504**(2): 196-219.

175. Stadtman ER, Oliver CN. Metal-catalyzed oxidation of proteins. Physiological consequences. *Journal of Biological Chemistry* 1991; **266**(4): 2005-8.
176. Hemnani T, Parihar MS. Reactive oxygen species and oxidative DNA damage. *Indian journal of physiology and pharmacology* 1998; **42**(4): 440-52.
177. Moan J, Berg K. PHOTOCHEMOTHERAPY OF CANCER: EXPERIMENTAL RESEARCH. *Photochemistry and Photobiology* 1992; **55**(6): 931-48.
178. Dobrucki JW, Feret D, Noatynska A. Scattering of Exciting Light by Live Cells in Fluorescence Confocal Imaging: Phototoxic Effects and Relevance for FRAP Studies. *Biophysical Journal* 2007; **93**(5): 1778-86.
179. Feuerstein O, Persman N, Weiss EI. Phototoxic Effect of Visible Light on Porphyromonas gingivalis and Fusobacterium nucleatum: An In Vitro Study¶†. *Photochemistry and Photobiology* 2004; **80**(3): 412-5.
180. Henry CA, Dyer B, Wagner M, Judy M, Matthews JL. Phototoxicity of argon laser irradiation on biofilms of Porphyromonas and Prevotella species. *Journal of Photochemistry and Photobiology B: Biology* 1996; **34**(2): 123-8.
181. He J-A, Hu Y-Z, Jiang L-J. Photodynamic action of phycobiliproteins: in situ generation of reactive oxygen species. *Biochimica et Biophysica Acta (BBA) - Bioenergetics* 1997; **1320**(2): 165-74.
182. Perny M, Muri L, Dawson H, Kleinlogel S. Chronic activation of the D156A point mutant of Channelrhodopsin-2 signals apoptotic cell death: the good and the bad. *Cell Death & Disease* 2016; **7**(11): e2447.
183. Schwinger RH, Böhm M, Müller-Ehmsen J, et al. Effect of inotropic stimulation on the negative force-frequency relationship in the failing human heart. *Circulation* 1993; **88**(5): 2267.
184. Oheim M, van 't Hoff M, Feltz A, Zamaleeva A, Mallet J-M, Collot M. New red-fluorescent calcium indicators for optogenetics, photoactivation and multi-color imaging. *Biochimica et Biophysica Acta (BBA) - Molecular Cell Research* 2014; **1843**(10): 2284-306.
185. Ronaldson-Bouchard K, Ma SP, Yeager K, et al. Advanced maturation of human cardiac tissue grown from pluripotent stem cells. *Nature* 2018; **556**(7700): 239-43.
186. Hwang HS, Kryshtal DO, Feaster TK, et al. Comparable calcium handling of human iPSC-derived cardiomyocytes generated by multiple laboratories. *Journal of Molecular and Cellular Cardiology*; **85**: 79-88.
187. Keung W, Boheler KR, Li RA. Developmental cues for the maturation of metabolic, electrophysiological and calcium handling properties of human pluripotent stem cell-derived cardiomyocytes. *Stem Cell Research & Therapy* 2014; **5**(1): 17.
188. Lesperance LS, Lankarany M, Zhang TC, Esteller R, Ratté S, Prescott SA. Artifactual hyperpolarization during extracellular electrical stimulation: Proposed mechanism of high-rate neuromodulation disproved. *Brain Stimulation* 2018; **11**(3): 582-91.
189. Bostock H, Cikurel K, Burke D. Threshold tracking techniques in the study of human peripheral nerve. *Muscle & Nerve* 1998; **21**(2): 137-58.
190. Wessale JL, Geddes LA, Ayers GM, Foster KS. Comparison of rectangular and exponential current pulses for evoking sensation. *Annals of Biomedical Engineering* 1992; **20**(2): 237-44.
191. Ishizuka T, Kakuda M, Araki R, Yawo H. Kinetic evaluation of photosensitivity in genetically engineered neurons expressing green algae light-gated channels. *Neuroscience Research* 2006; **54**(2): 85-94.
192. Williams JC, Xu J, Lu Z, et al. Computational Optogenetics: Empirically-Derived Voltage- and Light-Sensitive Channelrhodopsin-2 Model. *PLoS Computational Biology* 2013; **9**(9): e1003220.
193. Tulloch NL, Muskheli V, Razumova MV, et al. Growth of Engineered Human Myocardium With Mechanical Loading and Vascular Coculture. *Circulation Research* 2011.
194. Jacot JG, McCulloch AD, Omens JH. Substrate Stiffness Affects the Functional Maturation of Neonatal Rat Ventricular Myocytes. *Biophysical Journal* 2008; **95**(7): 3479-87.
195. Bray M-A, Sheehy SP, Parker KK. Sarcomere Alignment is Regulated by Myocyte Shape. *Cell motility and the cytoskeleton* 2008; **65**(8): 641-51.

196. Wang P-Y, Yu J, Lin J-H, Tsai W-B. Modulation of alignment, elongation and contraction of cardiomyocytes through a combination of nanotopography and rigidity of substrates. *Acta Biomaterialia* 2011; **7**(9): 3285-93.
197. McDevitt TC, Angello JC, Whitney ML, et al. In vitro generation of differentiated cardiac myofibers on micropatterned laminin surfaces. *Journal of Biomedical Materials Research Part A* 2002; **60**(3): 472-9.
198. Jackman CP, Carlson AL, Bursac N. Dynamic culture yields engineered myocardium with near-adult functional output. *Biomaterials* 2016; **111**: 66-79.
199. Xia Y, Buja LM, Scarpulla RC, McMillin JB. Electrical stimulation of neonatal cardiomyocytes results in the sequential activation of nuclear genes governing mitochondrial proliferation and differentiation. *Proceedings of the National Academy of Sciences of the United States of America* 1997; **94**(21): 11399-404.
200. Nunes SS, Miklas JW, Liu J, et al. Biowire: a new platform for maturation of human pluripotent stem cell derived cardiomyocytes. *Nature methods* 2013; **10**(8): 781-7.
201. Kensah G, Gruh I, Viering J, et al. A Novel Miniaturized Multimodal Bioreactor for Continuous In Situ Assessment of Bioartificial Cardiac Tissue During Stimulation and Maturation. *Tissue Engineering Part C, Methods* 2011; **17**(4): 463-73.
202. Heidi Au HT, Cui B, Chu ZE, Veres T, Radisic M. Cell culture chips for simultaneous application of topographical and electrical cues enhance phenotype of cardiomyocytes. *Lab on a Chip* 2009; **9**(4): 564-75.
203. Dana H, Mohar B, Sun Y, et al. Sensitive red protein calcium indicators for imaging neural activity. *eLife* 2016; **5**: e12727.
204. Lapp H, Bruegmann T, Malan D, et al. Frequency-dependent drug screening using optogenetic stimulation of human iPSC-derived cardiomyocytes. *Scientific Reports* 2017; **7**(1): 9629.